Development of an L-Band Clear-Air Doppler Radar and Its Application to Planetary Boundary Layer Observations over Equatorial Indonesia

by

Hiroyuki Hashiguchi

January 1995

Development of an L-Band Clear-Air Doppler Radar and Its Application to Planetary Boundary Layer Observations over Equatorial Indonesia

by

Hiroyuki Hashiguchi

January 1995

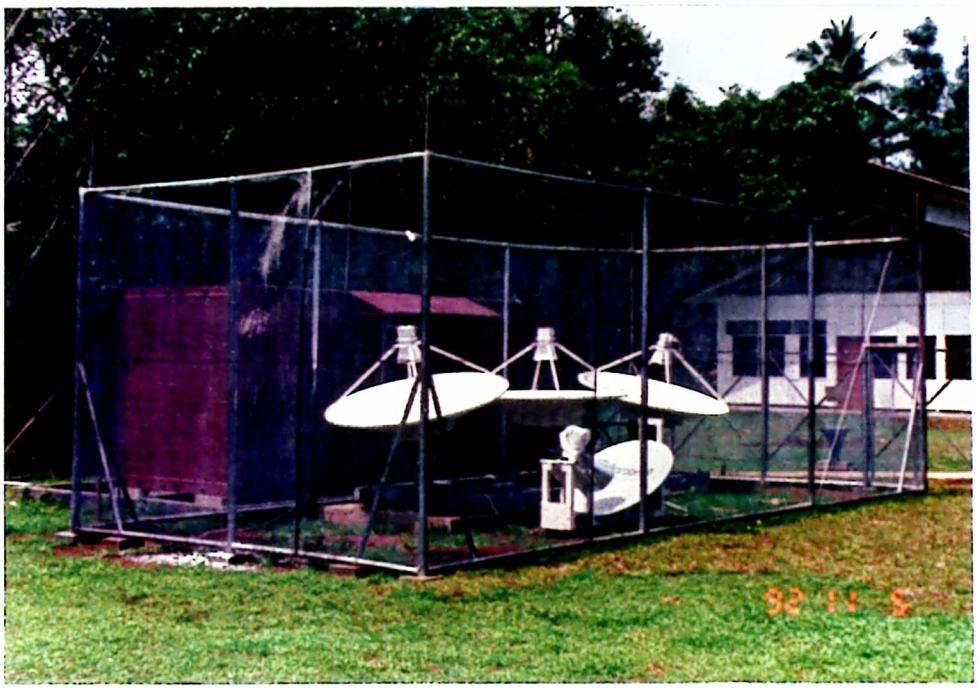

The Kyoto University Boundary Layer Radar (BLR) installed in Serpong, Indonesia (6.4°S, 106.7°E).

Acknowledgments

The author wishes to express his sincere appreciation to Professor Shoichiro Fukao for his guidance and supervision in the present work. The author also wishes to express his hearty gratitude to Emeritus Professor Susumu Kato for his ceaseless encouragement regarding the present work. The author deeply thanks Professors Iwane Kimura and Hisanao Ogura for their helpful advices and suggestions for the present work.

Special thanks are due to Dr. Manabu D. Yamanaka for a number of stimulating discussions, kind guidance, and continuous encouragement throughout the present work, and for careful reading of the manuscript. The author deeply appreciates Dr. Toshitaka Tsuda, of whom the radar observations in Indonesia were planed, were prepared, and have been conducted under the leadership, and who gave many constructive advices and encouragement. The author is grateful to Drs. Toru Sato, Mamoru Yamamoto, Takuji Nakamura, Kaoru Sato, and Mr. Tatsuhiro Adachi for their useful suggestions and comments regarding the present work. The author greatly thanks Professor Grahame Fraser and Dr. William O. J. Brown for his careful reading of the original manuscript. The author thanks Dr. Tsuneichi Makihira, Messrs. Kyosuke Hamatsu, Kiyoyuki Hata, and the other persons of Mitsubishi Electric Corporation regarding the development of the BLR for their cooperation.

Thanks are also due to Dr. Akira Watanabe, Messrs. Adikusumah Nurzaman, Masaki Tsutsumi, Toyoshi Shimomai, and Noriaki Yoshino for their cooperation for the dry and rainy season campaigns. The author thanks Professor Harsono Wiryosumarto, Mrs. Sri Woro B. Harijono, Miss Tien Sribimawati, Mr. Baginda P. Sitorus, Mrs. Mimin Karmini, Messrs. Daniel L. Tobing, Findy Renggono, Bona L. Parapat, Dwipa W. Soehoed, Bambang A. Wahyudi, Rafiq M. Santosa, Rino B. Yahya, all the other operators who maintain the Serpong radar observatory, and colleagues of BPPT, LAPAN, and RASC for their collaborations.

The author thanks Drs. Masato Murakami and Tetsuo Nakazawa for providing the GMS IR data, and Drs. Yukari Takayabu and Atsushi Numaguchi for comments regarding the GANAL data. The helpful comments of and discussions on observational results with Professor Kenji Nakamura, Drs. Tokunosuke Fujitani, Osamu Tsukamoto, Minoru Gamo, Yuji Osaki, Yuichi Ohno, L. Mahrt are warmly acknowledged.

The author thanks Drs. Takuya Sugiyama, Tomoyuki Takami, Messrs. Yoshiaki Shibagaki, Shinya Ogino, Mitsuru Sato, Takaaki Muro, Masanori Hayashi, Ipuk Widiyatmi, and Atsushi Shimizu for the helpful discussions and their technical support regarding computer software. The author indebted to all staffs of Radio Atmospheric Science Center, Kyoto University.

The author was supported by a grant (1289) of the Japan Society for the Promotion of Science (JSPS) under the Fellowships for Japanese Junior Scientists. A part of the present work was financially supported also by Grants-in-Aids (02554012, 04NP0201, 05NP0201) of the Japanese Ministry of Education, Science and Culture.

Abstract

The Planetary Boundary Layer (PBL) is recognized as an important height range connecting the free atmosphere with the earth's surface where almost all sources of energy, momentum, and constituents in the earth's atmosphere are to be found. The importance of the PBL is much enlarged when we consider that the earth's environment is maintained under the atmosphere-ocean and/or atmosphere-land interactions. However, mainly because of a lack of appropriate observational techniques, many aspects of the PBL have not yet been clarified sufficiently. The height range of the PBL is beyond that of continuous observations at a tower, and the complexity of the PBL cannot be resolved by balloon observations.

Those observational difficulties are now being overcome with the advance of radio probing techniques, called low-level wind profilers or boundary layer radars. These techniques provide three-components of the wind velocity vector averaged in a sampling volume with a high time resolution. We have successfully developed a transportable clear-air Doppler radar system (the Kyoto University Boundary Layer Radar, hereafter referred to the BLR), operating at a frequency of 1357.5 MHz (L-band) with a peak transmitter power of 1 kW. The antennas consist of three parabolic antennas with a diameter of 2 m.

The BLR was first installed at the MU (Middle and Upper atmosphere) Observatory at Shigaraki, Japan (34.85°N, 136.10°E) in December 1991, and continuous observations were conducted during May–August 1992. From the continuous four-month observations, we have found that on clear days a thin enhanced echo layer appears at about 500 m height in the morning and ascends up to about 1500 m height in the afternoon. We have found that this enhanced echo layer corresponds to the top of the PBL (mixing layer) defined by the virtual potential temperature profiles obtained simultaneously by radiosondes. The behavior of this layer is consistent with that of the PBL speculated or predicted numerically in earlier studies, but here we further directly observe variations of three-components of the wind velocity vector and smaller-scale turbulence activity. These remarkable diurnal variations of the echo intensity are not always observed every clear day but are limited to a few days each month.

We aimed to observe characteristics of cloud convections and atmospheric waves in the lower troposphere over equatorial Indonesia by means of the BLR. Through collaboration between Japan and Indonesia, we started continuous observations using the BLR in November 1992 at PUSPIPTEK (Indonesia National Center for Research, Science, and Technology) in Serpong (6.4°S, 106.7°E), West Java, which is located in the south-west suburbs of Jakarta. The performance of

the BLR with respect to the observation height range and the wind measurement reliability has been examined on the basis of simultaneous rawinsonde observations.

We have found that there are two types of strong echo structures appearing systematically in the equatorial PBL with diurnal variations on clear days. The first type is the striking appearance of a strong echo layer ascending from below 300 m (in the morning) to above 3–5 km (in the afternoon), which is identified with a diurnal variation of the top of the mixing PBL. This layer appears at higher altitudes in the Indonesian equatorial region than in mid-latitudes. Another type of strong echo structure are layered echoes appearing at an altitude of 2–3 km from night-time to morning, which seem to be coincident with humidity gaps.

We have also found a striking reversal of the wind direction from easterly to westerly at the beginning of December 1992. It is confirmed from geostationary meteorological satellite (GMS) observation data that this reversal was associated with an eastward movement of the convection center (a super cluster) situated between the Indian Ocean monsoon (westerly) dominant area and the Pacific Ocean trade wind (easterly) dominant area. The lower-tropospheric wind variations associated with (super) cloud clusters are presented, and some differences are found between the eastern and western sides of the convection center (corresponding respectively to the easterly and westerly regimes; or to the dry and rainy seasons).

Frequency power spectra are analyzed from zonal and meridional wind velocities observed continuously in a height range below 2.5 km with the BLR. We have found that (i) the spectral slope in a period range from a few hours to a few days is approximately -1; (ii) the power spectral densities in the rainy season are at least about two times larger than those in the dry season; (iii) the diurnal component is dominant both in dry and rainy seasons; (iv) components with periods of about 4 and 10 days are probably associated with mixed Rossby-gravity wavelike cloud clusters and Kelvin wavelike super cloud clusters, respectively, and (v) the power spectral amplitudes increase at least one order of magnitude from the bottom to the top of the equatorial PBL, and the values at the top of the PBL are almost comparable to those in the upper troposphere over mid-latitudes. The last feature suggests strongly that the equatorial PBL is a major source of kinetic energy in the earth's atmosphere.

We believe that these studies must contribute to the spread of BLR observations and to the elucidation of many unknown important roles of the PBL over equatorial Indonesia in the earth's environmental problems.

Contents

List of Figures

List of Tables

Chapter 1

General introduction

1.1 The history of radar studies of the clear atmosphere

The history of radar studies of the clear atmosphere is broken down roughly into four major periods. The first, starting about 1935 and extending until 1949, defines the time when several types of clear-air echoes were observed and reported. The 10–200 m wavelength radars used for ionospheric studies detected reflections in the troposphere where it was known that ionized regions could not exist. Toward the end of this period *Friend* [1949] was able to associate these tropospheric reflections with regions of temperature inversions where large gradients of refractive index would be present. In addition, the first observations of dot echoes, later designated "dot angels," were reported. A controversy arose regarding the source of these dot angels; insects and birds were one possibility and sharp gradients in refractive index were another.

The second period occurred from about 1950 to 1962 and was marked by great interest and experimental work in propagation beyond the radio horizon. One of the mechanisms for the radio propagation was the scattering of radio waves from turbulent structures within the troposphere. The period was significant because the processes responsible for the tropospheric scatter observed on radio propagation links were also a factor in the backscatter of radar energy. This period saw heightened interest in dot angels as shorter wavelength (from 1 to 10 cm) radars were developed and reports of the angels became commonplace. At the same time, horizontally stratified echo layers were also observed with 10-cm wavelength radars, and it became evident that radars could play an important role in probing the clear atmosphere.

The third period from 1963 to 1972 saw a tremendous increase in activity

using powerful and sensitive radars for investigating atmospheric structures. Notable among the achievements during this decade were the *in situ* measurements within the regions of the clear-air radar echoes, the routine detection of clear-air turbulence out to ranges of 10–20 km with 10 cm or longer wavelength radars, and the study of convective processes in the boundary layer. The period came to a close with some incredibly detailed observations using radars which could resolve atmospheric waves and layers at resolutions of 1 m.

The fourth period from 1973 to 1982 was characterized by a major shift in the focus of clear-air radar research from the UHF (300–3,000 MHz) and shorter wavelength radars used in the previous period to longer wavelength radars that operated primarily at lower VHF (30–300 MHz) frequencies. It was shown by *Woodman and Guillén* [1974] that it is possible to detect the radiowave scattered by the neutral atmosphere by using the 50 MHz Jicamarca radar in Peru. Atmospheric radars utilize a physical principle that the radiowave are scattered and/or reflected by fluctuations of the radio refractivity of the atmosphere.

Afterwards, MST (Mesosphere, Stratosphere, and Troposphere) radars like the MU (Middle and Upper atmosphere) radar [*Fukao et al.*, 1985a, b] were established in several places. A number of these radars have been operated at approximately 50 MHz, and had large antenna aperture and strong output power in order to detect very weak radiowave scattered by the neutral atmosphere. The radars operating at this lower part of the VHF band have some prominent advantages over radars operating at higher frequencies. One important advantage is that the atmospheric scattering at lower VHF is nearly as strong as scattering from precipitation. Consequently, vertical atmospheric motion can be measured at these frequencies even during rainfall [*Fukao et al.*, 1985c, *Wakasugi et al.*, 1986, 1987]. The MU radar is located in Shigaraki, Japan (34.85°N, 136.10°E), and has been operated from 1984. The studies concerning the three-dimensional structure of the wind velocity have been performed. Especially, there are the excellent studies concerning the fine structure of the wind field in the typhoon [e.g., *Sato et al.*, 1990; *Sato*, 1993] and in the baiu front [e.g., *Fukao et al.*, 1988]. Many studies concerning the atmospheric waves have also been pursued very much [e.g., *Murayama et al.*, 1992; *Nakamura et al.*, 1993b].

Using radars for clear-air studies was not only challenging and interesting but also led to important operational applications. Two of the major applications developed during the 1980s were as follows:

i) UHF and VHF Doppler radars became to be used for the routine measurement of the wind field within the troposphere;

ii) Requirements for the next operational weather radar (NEXRAD) were developed in U.S., which included the capability to observe low-level wind

fields in the clear atmosphere.

Both of these developments will be incorporated into observing networks which will provide enhanced depictions of the weather on smaller scales than were previously possible.

In the late 1980s, *Ecklund et al.* [1988] of Aeronomy Laboratory of NOAA (National Oceanic and Atmospheric Administration) in U.S. developed a prototype of 915 MHz boundary layer radar (BLR) which is lightweight, transportable, and low powered. In Japan, we and *Nakamura et al.* [1992] of CRL (Communications Research Laboratory) of Ministry of Posts developed *L*-band (1357.5 MHz) BLRs in independence in 1991 [*Hashiguchi et al.*, 1992]. Our BLR was first installed at the MU Observatory in Shigaraki in December 1991, and continuous observations were conducted during May–August 1992. After that, the BLR was transported to and installed in Serpong, Indonesia (6.4°S, 106.7°E), and continuous observations have been conducted since November 1992. *Nakamura et al.*'s BLR has been operated in Thailand since 1994.

1.2 The planetary boundary layer (PBL)

The atmospheric boundary layer (ABL) is usually defined as the layer of air directly above the earth's surface in which the effects of the surface (friction, heating, and cooling) are directly felt on time scales less than a day, and in which significant fluxes of momentum, heat, or matter are carried by turbulent motions on a scale of the order of the depth of the ABL or less (see Figure 1.1). The ABL thickness is quite variable in time and space, ranging from hundreds of meters to a few kilometers.

The atmospheric layer from the surface to about 100 m is called "surface boundary layer" (SBL) because this height range is prominently influenced by the features of the surface. The ABL higher than the SBL is called the "Ekman layer" or "planetary boundary layer" (PBL). The atmosphere higher than the PBL is called the "free atmosphere." The earth's surface and the ABL become sources for the most atmospheric phenomena in the lower and middle atmosphere.

Diurnal variation is one of the key characteristics of the ABL over land. The free atmosphere shows little diurnal variation. This diurnal variation is not caused by direct forcing of solar radiation on the ABL. Little solar radiation is absorbed in the ABL; most is transmitted to the ground where typical absorptivities on the order of 90% result in absorption of much of the solar energy. It is the ground that warms and cools in response to the radiation, which in turn forces changes in the ABL via transport processes. Turbulence is one of the important transport processes, and is sometimes also used to define the ABL.

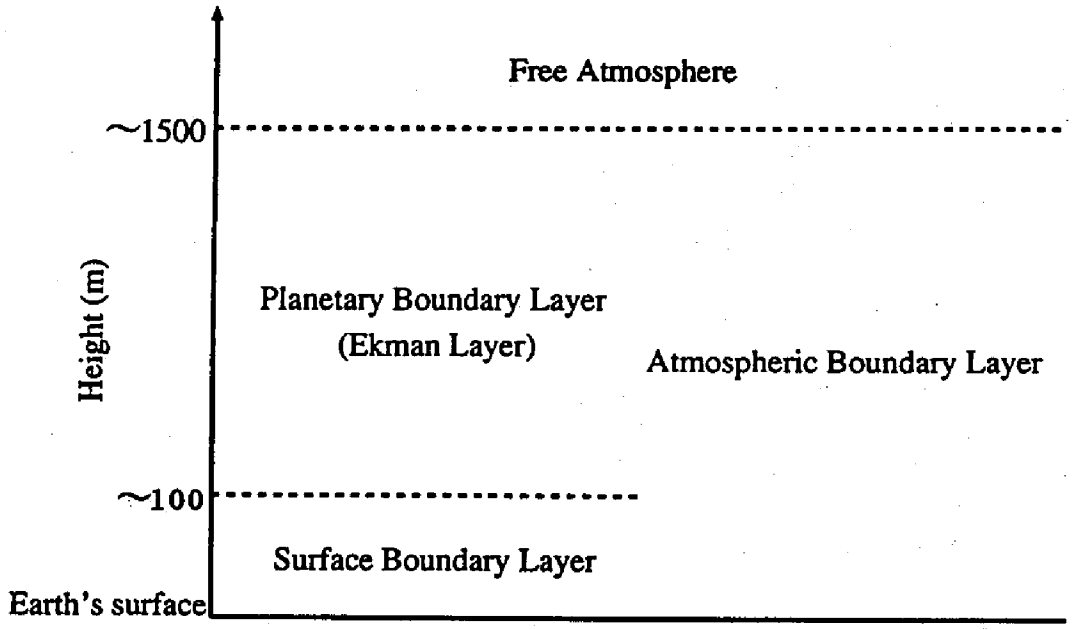

Figure 1.1: Schematic atmospheric boundary layer structure.

The ABL is recognized as an important height range connecting the free atmosphere with the earth's surface where almost all the sources of energy, momentum, and constituents of the earth's atmosphere are to be found. As emphasized in recent textbooks [e.g., *Stull*, 1988; *Garratt*, 1992], the importance of the PBL is much enlarged when we consider that the earth's environment is maintained under the atmosphere-ocean and/or atmosphere-land interactions.

In the SBL, the wind speed rapidly increases according with altitudes, but the mean wind direction hardly changes. The variation of the wind velocity in the PBL is quite different. We assume that the diffusion coefficient K is constant which is independent of heights, and the following boundary conditions are satisfied:

$$\begin{array}{ll} U = V = 0 & (z = 0) \\ U - U_g = V - V_g \to 0 & (z \to \infty) \end{array} \tag{1.1}$$

where z is the height, (U, V) is the horizontal wind velocity, and (U_g, V_g) is the geostrophic wind velocity. In order to simplify the expression, we consider that x axis equals to the direction of the geostrophic wind velocity (i.e. it is parallel to the direction of an isobaric line). Then the geostrophic wind velocity is $(U_g, 0)$,

and the wind velocity (U, V) in the PBL is derived as the following:

$$U = U_g \left\{ 1 - \exp\left(-\frac{z}{D}\right) \cos\frac{z}{D} \right\}$$
$$V = U_g \exp\left(-\frac{z}{D}\right) \sin\frac{z}{D} \tag{1.2}$$

where

$$D = \sqrt{\frac{2K}{f}} \tag{1.3}$$

where f is the Coliolis' parameter. The hodograph of these equations is shown in Figure 1.2. The profile becomes spiral shape called "Ekman spiral." The height

$$z = \pi D = \pi\sqrt{\frac{2K}{f}} \tag{1.4}$$

denotes the boundary between the ABL and the free atmosphere.

In the ABL, there are complicated phenomena of summit-valley breeze circulation, sea-land breeze circulation, and others as shown in Figure 1.3. Especially, to analyze the following phenomena is very important: (i) boundary layer convergence processes, and (ii) their relationship to atmospheric convection. Also (iii) wind fluctuations in the ABL are important since they notably appear with the process of the generation and organization of cloud clusters in the equatorial region and during baiu season in Japan. The analysis of the atmospheric motion in this layer is indispensable to solve the environmental problems of the earth. In order to analyze these complicated phenomena, the high-resolution observation is needed.

Especially, it is now widely recognized that the dynamics of the PBL in the Indonesian equatorial region (the maritime continent) are very important to our understanding of global climate control mechanisms associated with the maritime continent surrounded by high surface temperature ocean. For example, PBL dynamics govern the generation of convection, and the large year-to-year variations of the cloud convection over the maritime continent are closely related to the behavior of the El Niño-southern oscillations (ENSO) [e.g., *Nitta et al.*, 1992]. Tall cumulonimbus clouds often penetrate the tropopause and transport various minor constituents in the troposphere deeply into the stratosphere [*Holton*, 1984]. They also excite various atmospheric waves, such as gravity waves, Kelvin waves, and other long period oscillations [*Tsuda et al.*, 1992, 1994a, b]. However, these studies are based on too coarse (or limited numbers of) observations with satellites or rawinsondes to clarify essential features of PBL dynamics over the maritime continent around Indonesia.

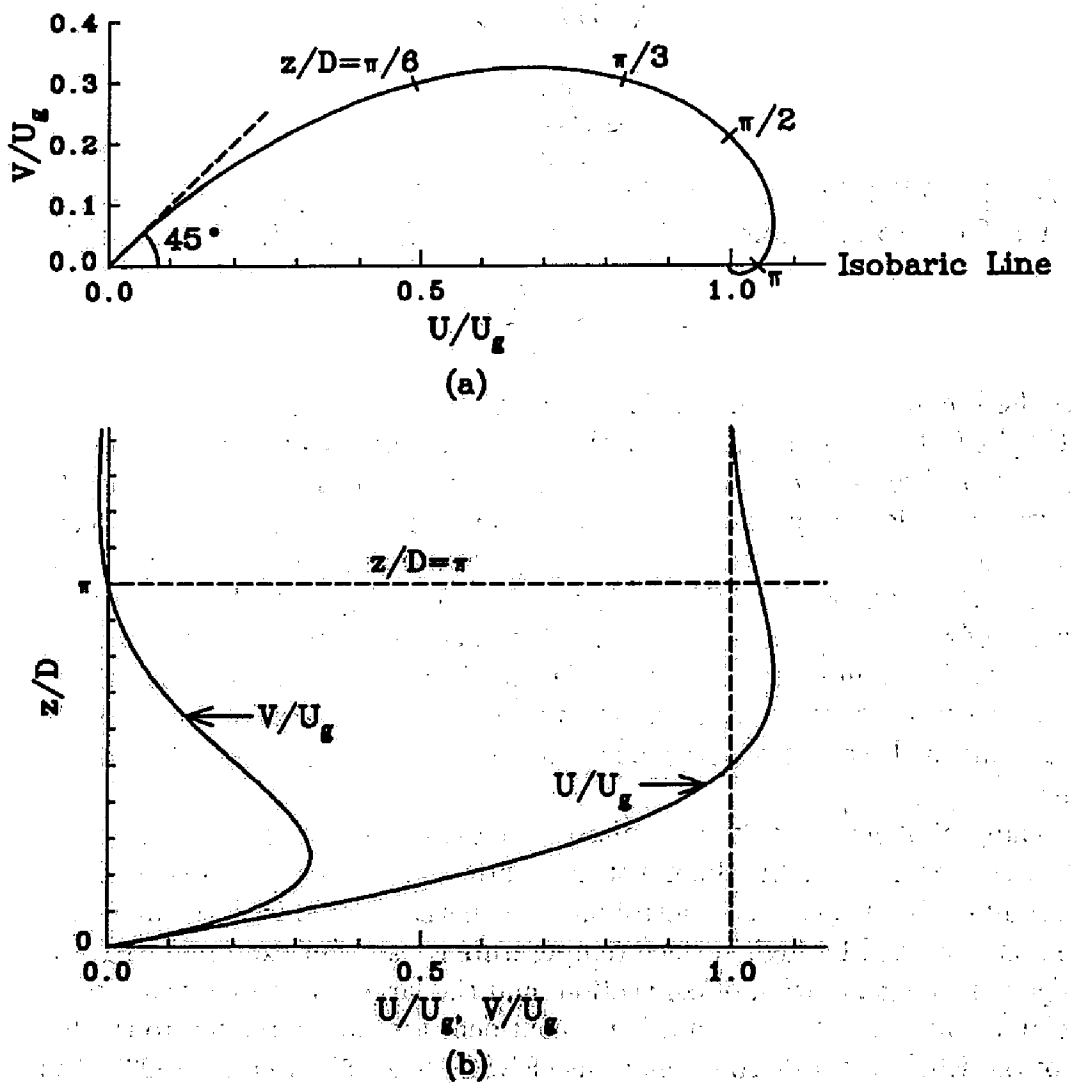

Figure 1.2: Ekman spiral. (a) Hodograph and (b) vertical profiles of the wind velocity [*Takeuchi and Kondo*, 1990].

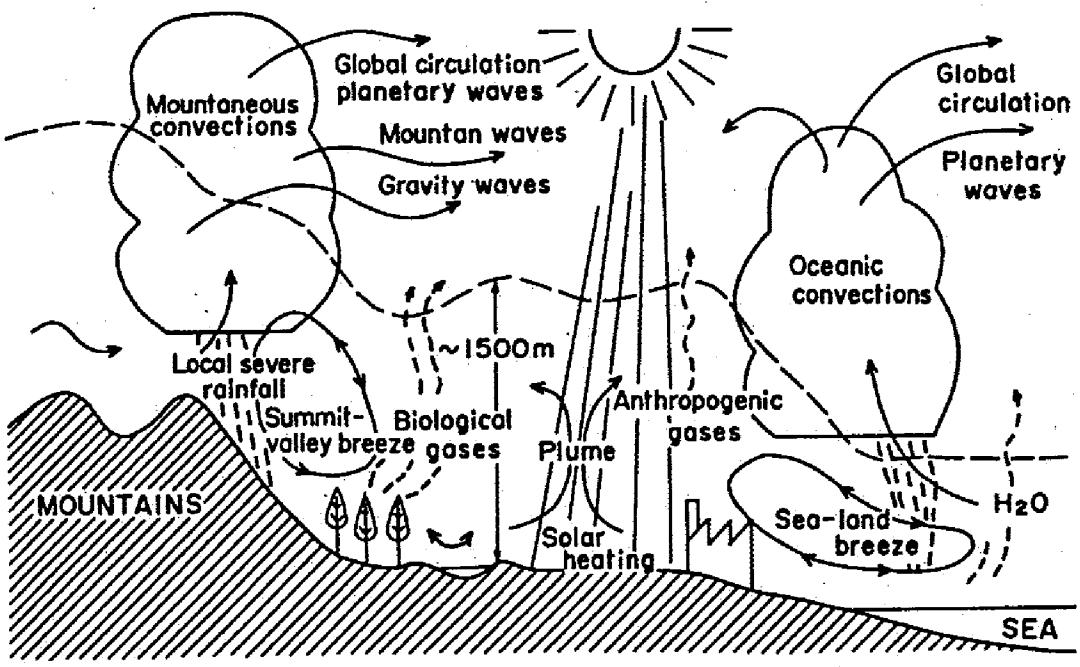

Figure 1.3: A schematic diagram of processes in the atmospheric boundary layer.

1.3 Observations in the PBL

Atmospheric motion in the ABL has mainly been observed so far by *in situ* techniques like balloons, towers, or aircraft. Balloons and towers are good techniques to observe temperature and humidity. However, as observation techniques for the atmospheric motion, the balloon observations have a limitation in the time resolution and cannot measure vertical wind velocities. The maximum observable altitude of towers is generally less than 100 m, and they have also the problem that the wind velocity can be disturbed by themselves. One of the major advantages of using aircraft as atmospheric measurement system is their mobility and capacity for making extended line averages of turbulent quantities (most aircraft flights occur at speeds of about 80 m s^{-1}). Aircraft can be used both for vertical profiling well above the tower layer and for horizontal traverses. The main disadvantage of aircraft measurements is the need to measure accurately the aircraft's motion, since corrections to the velocity and temperature measurements must be made for this motion.

In the last decade or so, ABL observations have been enhanced by remote sensing techniques. These mainly involve transmitted acoustic, radio, or light energy, and the detection of the scattered energy due to natural or artificial atmospheric targets (dust, salt, and/or rain). The instrumentation includes, for example, sodars (acoustic sounders); acoustic radars; lidars (light radars), and Doppler radars. Remote sensing of boundary-layer variables can be done actively and passively. Active techniques involve transmission of acoustic or electromagnetic radiation to the region of interest and measuring the backscattered fraction that is returned to the instrument; sensors include lidar, radar, and sodar. In contrast, passive techniques involve the measurement of radiation naturally emitted from the atmosphere, e.g. as in infrared radiometry.

Remote sensing techniques are attractive where *in situ* methods will not work or are uneconomical, and where the atmosphere interacts with the transmitted or received radiation allowing the meteorological variable of interest to be measured. Remote sensing utilizes spatial averages, usually over volumes, and so is especially suitable if this type of average is desired. However, lidars and sodars have the problems that observations are influenced by the weather conditions, and the highest observation height is relatively low.

As described in Section 1.1, VHF radars have been used to observe the wind field in the lower and middle atmosphere since 1970s. However, atmospheric radars in the low VHF range cannot measure atmospheric motion in altitudes of less than a few kilometers, which is seriously concerned with the human life as described in previous section, due to various technical reasons. To analyze atmo-

spheric motion in this layer is indispensable to solve the environmental problems. Since earlier observational techniques of the PBL have several problems due to their limited height coverage and/or resolution, the PBL have never been known in scales smaller than the internal meteorological phenomena. Therefore, we have developed the BLR to observe continuously height profiles of three-components of the wind velocity vector in the lower troposphere including the PBL with high time and height resolutions.

A radar radiates the radiowave, and accepts the information of targets by using the echo scattered and/or reflected by them. Macroscopic spatial changes of radio refractivity n cause refraction or reflection, but microscopic changes cause scattering. Major contributors to n at frequencies between HF (3–30 MHz) and UHF (300–3,000 MHz) bands are the partial pressure of water vapor e, the total atmospheric pressure p, and the electron density N_e. The experimental expression of n is

$$n - 1 = \frac{3.75 \times 10^{-1} e}{T^2} + \frac{7.76 \times 10^{-5} p}{T} - \frac{N_e}{2N_c} \tag{1.5}$$

where T is the absolute temperature, and N_c is the critical plasma density [*Balsley and Gage*, 1980]. The first term represents the contribution from water vapor, the second term gives the contribution from dry air, and the third term gives the contribution from free electrons. Figure 1.4 shows typical height profiles of these three terms. In the lower atmosphere, the first term is dominant, and the third term is negligible.

Random fluctuation of radio refractivity generated by the atmospheric turbulence is the major source of the echoes detected by the atmospheric radar [*Woodman and Guillén*, 1974]. Local fluctuations of radio refractivity is known to scatter radiowave and to move with the background atmospheric motion. We can obtain the information of the atmospheric motion by measuring the Doppler shift of the echoes. Since the scattering echo power is roughly proportional to the square of the number of scattering targets, we can also accept the information of intensity of the atmospheric turbulence by using the echo intensity.

A typical atmospheric radar is a monostatic pulse radar, which uses the same antenna in transmission and reception. The radar equation for a pulse radar is [*Sato*, 1988]

$$\overline{P_r} = \frac{\pi P_t A_e \cos\theta \Delta r^2 a^2 L}{64(\ln 2) c T_{IPP} r^2} \eta \tag{1.6}$$

where $\overline{P_r}$ is the received echo power, η is the radar volume reflectivity, c is the speed of light, r is the range, P_t is the peak transmitter power, θ is the zenith angle of the beam direction, Δr is the range resolution, a is the efficiency of the radar antenna and transmission line, L is the loss factor, T_{IPP} is the inter-pulse

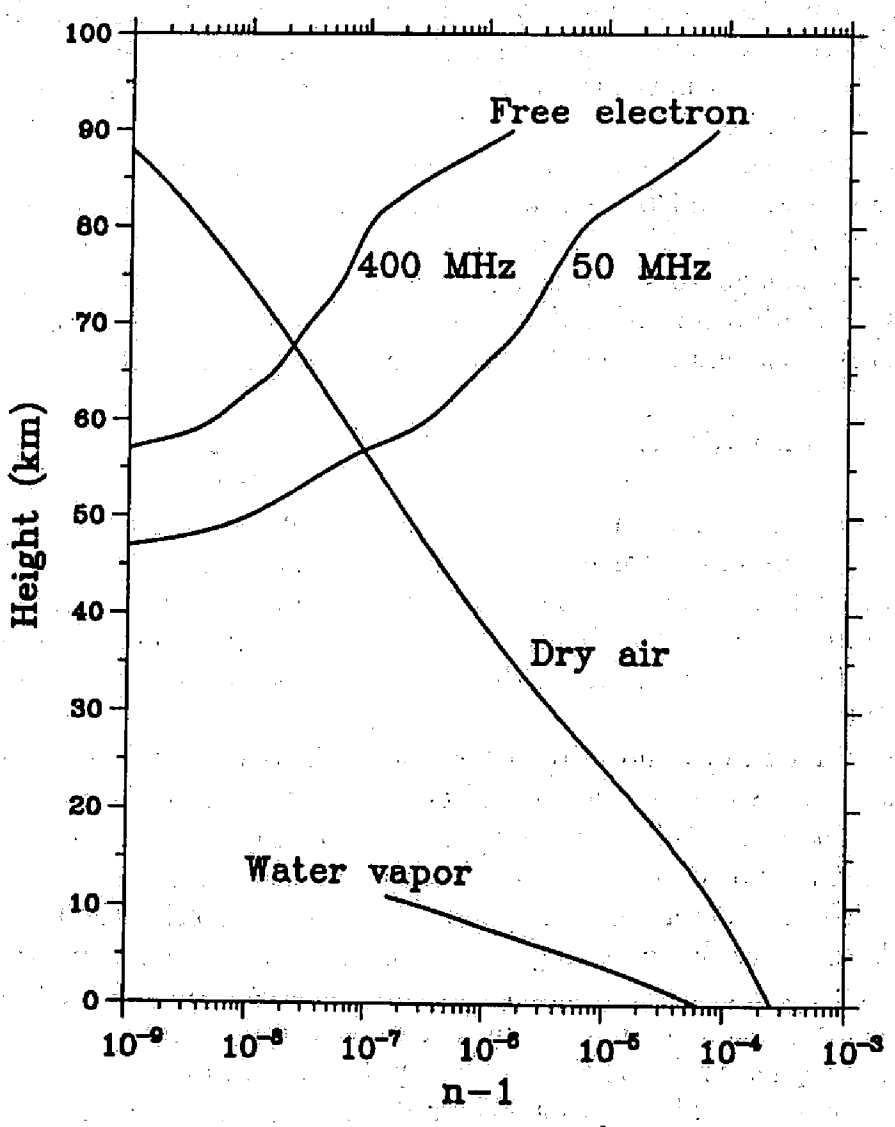

Figure 1.4: Typical height profiles of water-vapor, dry-air, and free-electron contributions to the radio refractivity n. The pressure and temperature are taken from the U.S. standard atmosphere. The saturation pressure is used for the water vapor. The electron density is adopted from *Mechtly et al.* [1972].

period (IPP), and A_e is the effective antenna area, which is given by [*Silver*, 1951]

$$A_e = \frac{\lambda^2 G_t}{4\pi} \tag{1.7}$$

where G_t is the antenna gain, and λ is the radar wavelength. The factor $\cos\theta$ accounts for the apparent reduction of the antenna area in the case using an active phased array antenna like the MU radar when it is viewed obliquely.

A pulse radar estimates a range from the radar to scattering target by using a time interval τ between the pulse transmission and reception. The range to a scattering target r is given by

$$r = \frac{1}{2} c\tau . \tag{1.8}$$

When a received signal is sampled at some time after transmission, the radar receives the echo from the target at the range corresponding to the delay time as shown in Figure 1.5. A range resolution Δr of a pulse radar with a pulselength Δt is

$$\Delta r = \frac{1}{2} c\Delta t \tag{1.9}$$

which corresponds to a half power width of the weighting function shown at the right panel in Figure 1.5. Because atmospheric turbulence is distributed target over the range, we can detect many echoes at different ranges by sampling the data every Δt. For example, by using $\Delta t = 1$ μs, we can observe the atmosphere with the range resolution of 150 m. We usually transmit many pulses every IPP, and obtain time series of scattering signal at each height. Therefore, in observations with a pulse radar, we take two dimensional data in altitude and time as shown in Figure 1.6.

Figure 1.7 shows a flow chart of the signal processing. The sampled signals are arranged as a function of a trip-around time from transmission to reception. Because correlation time of the signal is much longer than the IPP for the turbulence echoes in the lower and middle atmosphere, first they are coherently integrated in order to improve the signal-to-noise ratio. When $N_{\rm coh}$ data of complex received signal voltage are coherently added, noise power becomes $N_{\rm coh}$ times as large because we can assume random noise. However, power of the scattering signal becomes ${N_{\rm coh}}^2$ times as large. Therefore, signal-to-noise ratio is improved as

$$10\log_{10}\frac{N_{\rm coh}^2}{N_{\rm coh}} = 10\log_{10} N_{\rm coh} \ \ [\rm dB]. \tag{1.10}$$

This technique is called "coherent integration." The complex time series of the received signal is then Fourier transformed to a Doppler power spectrum. When

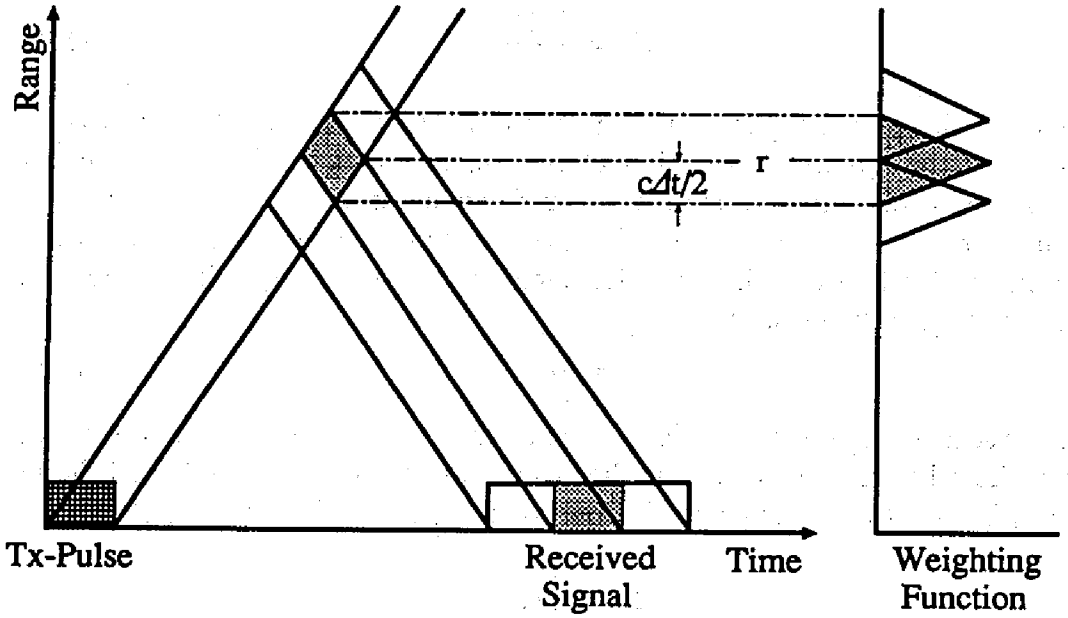

Figure 1.5: A time-height chart when a rectangular pulse is transmitted.

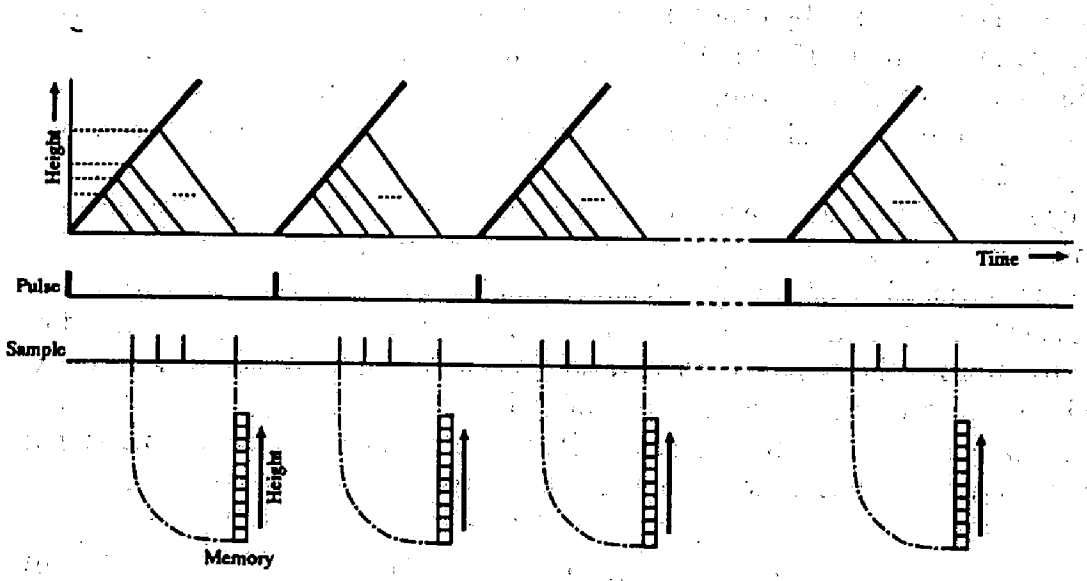

Figure 1.6: Time series of scattering signal.

the IPP is fixed, the number of data in the unit period is reduced by $1/N_{\rm coh}$ by the $N_{\rm coh}$ times of coherent integrations. This drastically reduces the FFT (Fast Fourier Transformation) calculation time. For example, when the FFT points of 4096 is reduced by 128 by conducting coherent integrations of 32 times, the FFT calculation time is reduced by approximately 1/55. If Doppler spectra are averaged as $N_{\rm icoh}$ times, statistical fluctuation of the Doppler spectrum becomes smaller by

$$\frac{1}{\sqrt{N_{\rm icoh}}}. \tag{1.11}$$

This technique is called "incoherent integration." Finally, the noise level and spectral parameters such as the echo power, mean Doppler shift, and spectral width are estimated from the Doppler spectrum, and are stored for the analysis of radar volume reflectivity, wind fields, and turbulence parameters.

Since we can assume that the atmospheric turbulence moves with a background wind, the mean Doppler shift is regarded as the radial component $v_{\rm r}$ of the wind velocity. It is given by [*Sato*, 1988]

$$v_{\rm r} = \frac{c}{2f_0} f_{\rm d} = \frac{\lambda}{2} f_{\rm d} \tag{1.12}$$

where $f_{\rm d}$ is the mean Doppler shift in $\rm s^{-1}$, f_0 is the operational frequency in $\rm s^{-1}$ of the radar. When we use the IPP of $T_{\rm IPP}$ and $N_{\rm coh}$ times of coherent integrations, Nyquist frequency $f_{\rm max}$ of Doppler spectrum is

$$f_{\rm max} = \frac{1}{2T_{\rm IPP}N_{\rm coh}}. \tag{1.13}$$

If Doppler shift is higher than this frequency, the signal causes frequency aliasing, and the estimated wind velocity is different from true one. When FFT points are $N_{\rm FFT}$, frequency resolution Δf is given by

$$\Delta f = \frac{2f_{\rm max}}{N_{\rm FFT}} = \frac{1}{T_{\rm IPP}N_{\rm coh}N_{\rm FFT}}. \tag{1.14}$$

Transforming to a velocity unit by using (1.12),

$$v_{\rm max} = \frac{\lambda}{2} f_{\rm max} = \frac{\lambda}{4T_{\rm IPP}N_{\rm coh}} \tag{1.15}$$

$$\Delta v = \frac{\lambda}{2}\Delta f = \frac{\lambda}{2T_{\rm IPP}N_{\rm coh}N_{\rm FFT}}. \tag{1.16}$$

Total time $T_{\rm obs}$ to obtain one Doppler spectrum including the incoherent integration is

$$T_{\rm obs} = T_{\rm IPP}N_{\rm coh}N_{\rm FFT}N_{\rm icoh} \tag{1.17}$$

where $N_{\rm icoh}$ is the number of incoherent integrations.

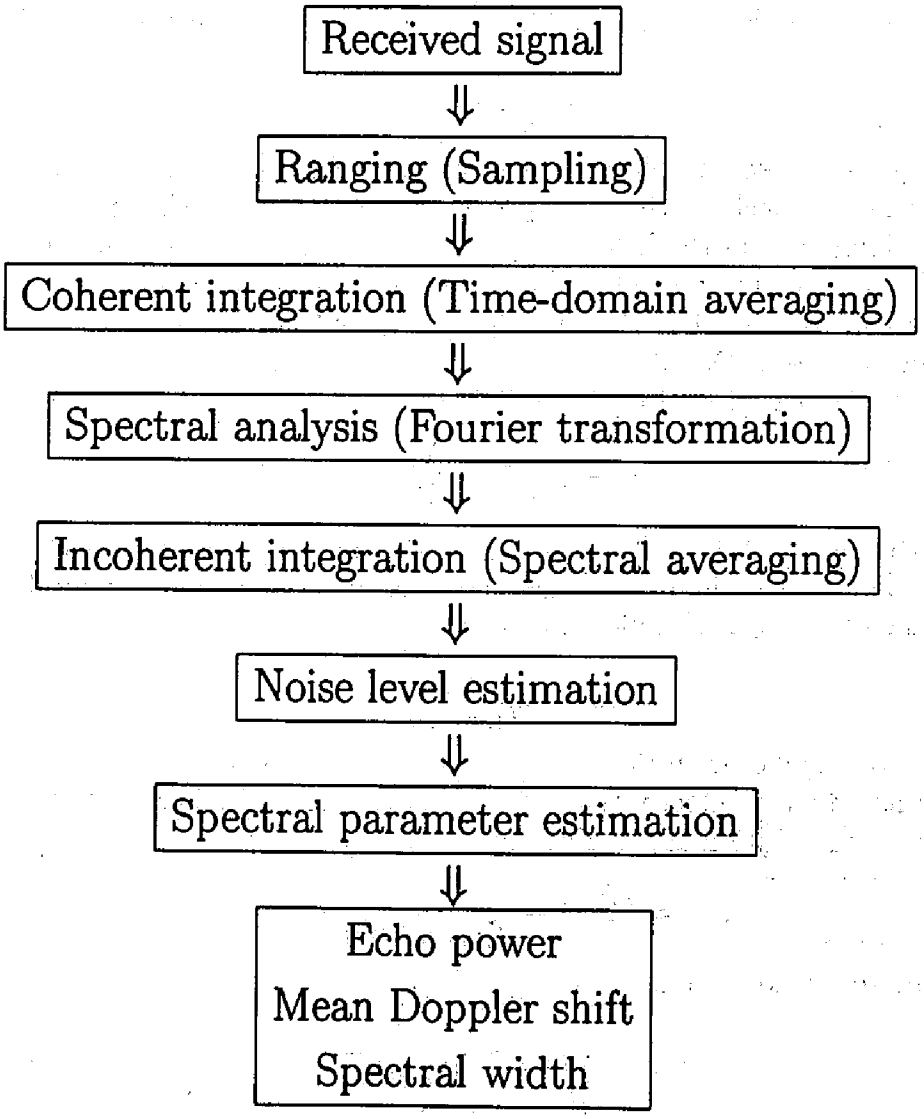

Figure 1.7: Flow diagram of a typical digital signal processing.

1.4 Contents of the thesis

As shown in the previous sections, the BLR is a powerful tool to investigate the dynamics of the PBL. The contents of this thesis are as follows.

In Chapter 2, system requirements of the BLR are first discussed. The hardware and software systems of the BLR designed based on the above discussions are shown. The method to estimate the spectral parameters from the echo power spectrum observed with the BLR is also described.

In Chapter 3, we present the results of the BLR simultaneously observed with the MU radar on 6 January 1992, and discuss the performance of the BLR in comparison with the results observed with the MU radar. The features of PBL diurnal variation obtained from four-month continuous observations in Shigaraki, Japan are also described.

In Chapter 4, we describe the outline of the observation project in equatorial Indonesia. The performance of the BLR in Indonesia, mainly concerning the observation height range and the wind measurement reliability are also described.

In Chapter 5, observational evidence concerning the vertical extent and diurnal variations of the equatorial PBL using the data observed with the BLR, rawinsondes, and standard ground-based instruments in the dry season campaign (8–15 October 1993) is described.

In Chapter 6, a striking reversal of the wind direction from easterly to westerly observed with the BLR at the beginning of December 1992 is presented. Geostationary meteorological satellite (GMS) observation data are also shown in order to discuss the relationship between this reversal and cloud clusters.

In Chapter 7, we present frequency power spectra of zonal and meridional wind velocities observed continuously in a height range below 2.5 km with the BLR, and describe the features of these spectra.

The summary and conclusions of this thesis are presented in Chapter 8.

Chapter 2

Development of the Kyoto University boundary layer radar (BLR)

In this chapter, the system requirements of the Kyoto University boundary layer radar (BLR) are first described in Section 2.1. The hardware system and the software configuration of the BLR designed based on the discussions in Section 2.1 are described in Sections 2.2 and 2.3, respectively. The method to estimate the spectral parameters — the echo power, the mean Doppler shift, and the spectral width — and the noise power density from the Doppler spectrum observed with the BLR is also described in Section 2.4.

2.1 System requirements

The BLR described in this thesis was designed to meet the following requirements:

i) The BLR should receive backscattered echoes from refractive index fluctuations, which are mainly generated by fluctuations of humidity and atmospheric stability profiles associated with atmospheric turbulence.

ii) The system should be transportable and have a small antenna with a far field of less than 100 m.

iii) System recovery should be fast enough to obtain useful data at heights as low as 300 m.

iv) The system should have a range resolution of 100 m or better and have a beamwidth of 9° or better.

v) The BLR should be sensitive enough to observe profiles of three-components of the wind velocity vector up to the height of 2–3 km with a time resolution of less than 1 min under typical atmospheric conditions.

vi) The BLR should be able to measure height profiles of temperature by using a RASS (Radio Acoustic Sounding System) technique.

Although radars in the low VHF range are practically operated to observe atmospheric motion, they cannot measure atmospheric motion near the ground. In the case of the MU radar [*Fukao et al.*, 1985a, b], the lowest observable height is approximately 2 km. This height limitation arises from various factors as the following:

i) Although these radars usually adopt the monostatic radar system, the switching speed and the system recovery from transmission to reception cannot be fast enough at relatively low operating frequency. For example, the height of 2 km corresponds to the switching speed of about 13 μs.

ii) The radar with the large aperture antenna system cannot inherently form well-defined beams within a few kilometers. In the case of the MU radar, the length of the near field is about 1.6 km.

iii) There is a practical limitation of the system bandwidth. For example, a range resolution of 75 m requires a transmitted pulselength of 0.5 μs and a corresponding bandwidth of about 2 MHz, which is very difficult to use in the VHF band.

We investigated a radar system to satisfy the above requirements for the BLR. In order to reduce the system recovery time (i.e. to lower the lowest observation height), an operating frequency of the BLR should be high. However, as shown in Figure 2.1 the radar volume reflectivity for the atmospheric turbulence becomes much smaller than that for the precipitation in the high frequency range. Namely, a radar that an operating frequency is very high cannot observe atmospheric motion directly even in cloudy conditions. The refractivity turbulence structure constant (C_n^2) and the radar refractivity index (Z) are approximately 10^{-15} m$^{-2/3}$ and 10^3 mm^6 m^{-3}, respectively, in the typical condition. When the operating frequency is 46.5 MHz of the MU radar, the volume reflectivities are $\eta_a \sim 2.0 \times 10^{-16}$ m^{-1} for the atmospheric turbulence and $\eta_p \sim 1.6 \times 10^{-16}$ m^{-1} for the precipitation. Namely, the MU radar has almost the same sensitivity for both turbulence and precipitation echoes [*Fukao et al.*, 1985c; *Wakasugi et al.*, 1986, 1987]. The BLR developed by *Ecklund et al.* [1988, 1990] uses the operating frequency of 915 MHz. Then, $\eta_a \sim 5.5 \times 10^{-16}$ m^{-1} and $\eta_p \sim 2.5 \times 10^{-11}$ m^{-1}. The echo intensity by the atmospheric turbulence is much smaller than the echo

by the precipitation. However, their radar could observe the atmospheric motion up to the height of a few kilometers. In Japan, this frequency cannot be used owing to the frequency allocation plan of the government. Instead, it is decided that our BLR uses the frequency of 1357.5 MHz (L-band). Then, $\eta_a \sim 6.3 \times 10^{-16}$ m^{-1} and $\eta_p \sim 1.2 \times 10^{-10}$ m^{-1}. It is expected that the BLR can obtain the 60 dB more intense precipitation echo compared with the atmospheric turbulence echo. Because the volume reflectivity is almost the same as that of the BLR of *Ecklund et al.*, our BLR can be also used to observe the atmospheric motion.

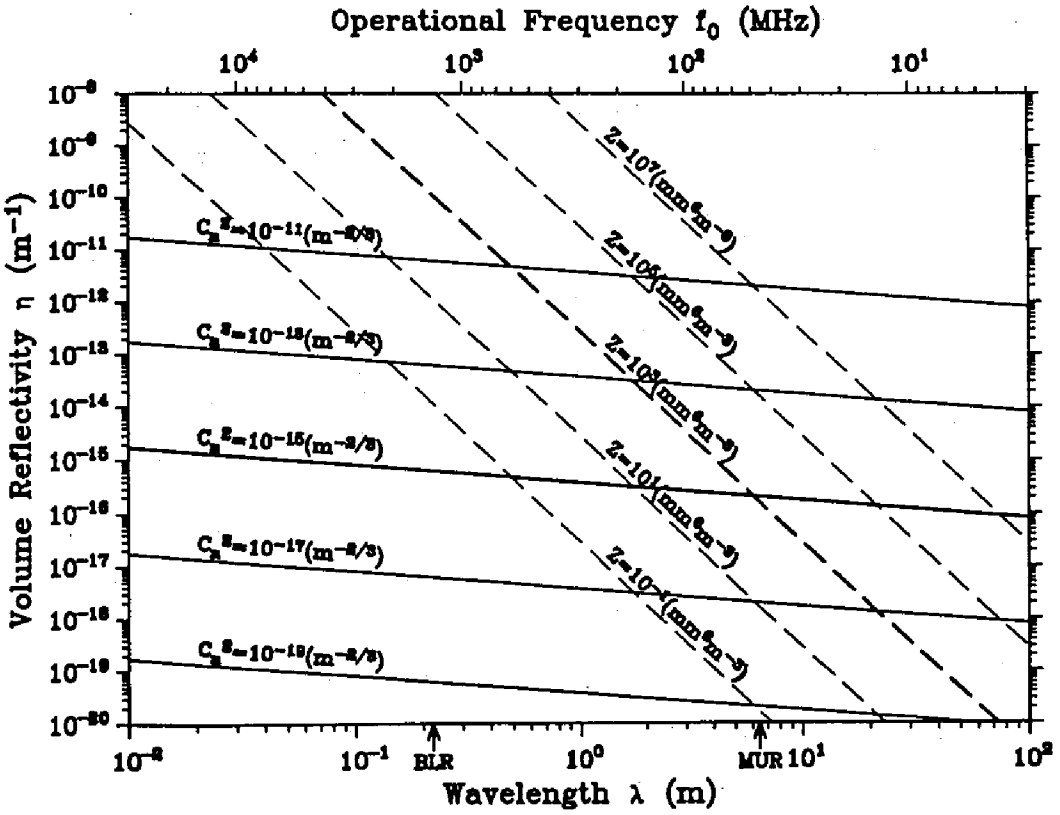

Figure 2.1: Volume reflectivity for the atmospheric turbulence (solid lines) and the precipitation (dashed lines) versus radar wavelength ($\eta = 0.38 C_n^2 \lambda^{-1/3} = 284 Z \lambda^{-4}$). Thick lines indicate typical values.

A far field of the circular antenna is given by D^2/λ, and a beamwidth is proportional to λ/D, where D is the antenna diameter and λ is the wavelength. As shown in Table 2.1, *Arimura* [1990] has studied the performance of the square antenna system for the operating frequency of 1350 MHz. When the antenna

aperture is 4.2×3.2 m^2, the beamwidth is about 4° but the length of the far field is longer than 100 m. When it is 1.2×0.8 m^2, the far field is 19 m long but the beamwidth is wider than 9°. Therefore, we should use the antenna of the second case (2.2×1.6 m^2) in order to satisfy the requirements that an antenna becomes as small as possible and a beamwidth becomes as narrow as possible. Finally, we determined to use the parabolic antenna with a diameter of 2 m for our BLR. The maximum output power was determined to be 1 kW. This was the maximum output power of the commercial products which were available to us.

Table 2.1: Comparison of performance for three kinds of antenna aperture [*Arimura*, 1990].

Parameter		Value		
Aperture	(m^2)	1.2×0.8	2.2×1.6	4.2×3.2
Beamwidth	Azimuth (°)	19.8	8.49	4.20
	Elevation (°)	13.1	6.53	3.26
Gain	(dB)	20.7	27.6	34.1
Sidelobe level	Azimuth (dB)	17.0	20.9	24.7
	Elevation (dB)	24.5	25.2	25.5
Far field	(m)	19	67	251

In order to observe three-components of the wind velocity vector, a radar needs to observe radial velocities at least in three different directions. There are following methods to change beam directions:

i) electric or electronic switching of three or more antennas;

ii) mechanical rotation of one antenna;

iii) electrical beam swinging by using an active phased array antenna like the MU radar.

For our BLR, we decided to use the first method because of the simple hardware construction and of the expected good performance.

Because the possibility to cause the range aliasing is little for the BLR that has relatively small output power, the shortest inter-pulse period (IPP) of 50 μs is suitable. When the zenith angle of a beam direction is 15°, the time interval of the time series must be less than 3 ms in order to measure the horizontal wind velocity up to 70 m s^{-1}. Then, the coherent integrations of 60 times can be performed, which make it possible to improve the signal-to-noise ratio. In order

to obtain the resolution of the horizontal wind of about 1 m s^{-1}, FFT points of 128 is required, and then it takes 384 ms to obtain one Doppler spectrum. If the beam direction can be changed for every Doppler spectrum, the simultaneity of observations in different beam directions can be satisfied. Therefore, the BLR does not need to change beam directions every IPP such as the MU radar. Finally, it was decided that the antennas should be switched after taking one time series of data for one Doppler spectrum as shown in Figure 2.2.

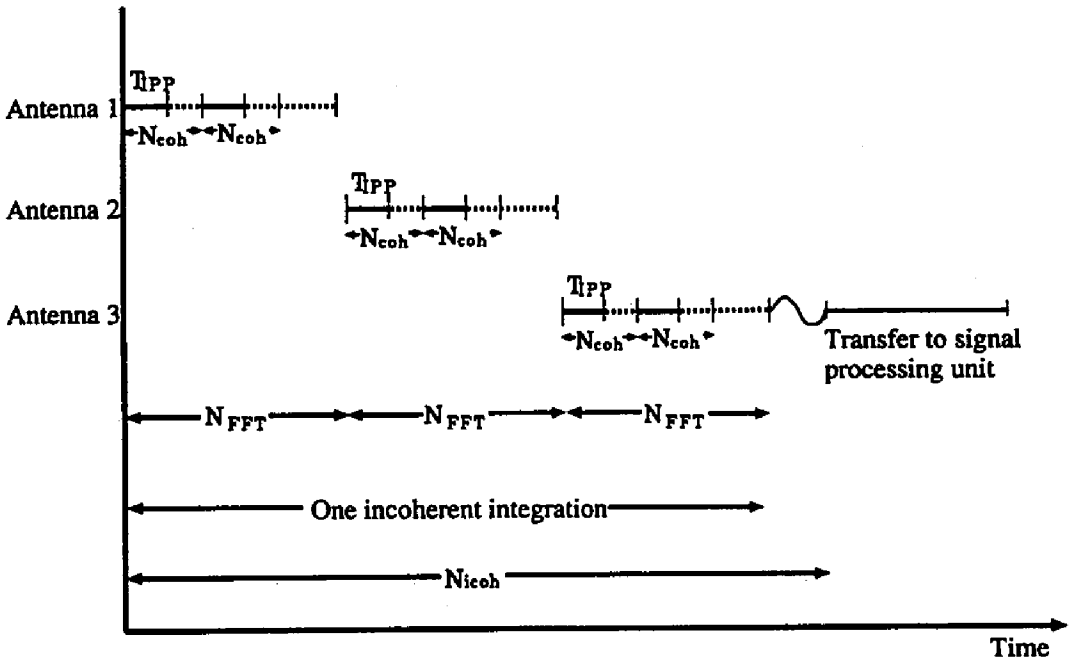

Figure 2.2: Time chart of data acquisition of the BLR. The horizontal axis indicates time, and in the vertical axis there are three charts for three antennas. T_{IPP}, N_{coh}, N_{FFT}, and N_{icoh} indicate IPP, the number of coherent integrations, the number of FFT points, and the number of incoherent integrations, respectively.

The radar to observe the PBL was first developed by *Ecklund et al.* [1988]. Specifications of their BLR is shown in Table 2.2. Their radar is more transportable than our BLR because the antenna is lightweight by using microstrip array, but their output power of 400 W is almost half of ours. Therefore, we expect that maximum observable height of our BLR is higher than their BLR. In Japan, *Nakamura and Masuda* [1992] have developed a BLR in independence of us. Specifications of their radar is shown in Table 2.3. The operating frequency

of 1357.5 MHz is the same as ours. Since their BLR mechanically rotates one parabolic antenna, the time resolution is not so good in comparison with ours. Digital signal processing is almost performed by software in our BLR so that observations could be very flexible, but performed by hardware in their BLR.

Table 2.2: Specifications of the BLR developed by *Ecklund et al.* [1988].

Radar system:	Monostatic pulse radar
Operating frequency:	915 MHz
Antenna:	Microstrip array
Aperture:	1.8×1.8 m^2
Beamwidth:	9°
Transmitter:	
Peak power:	400 W (maximum)
Pulselength:	0.7 μs
IPP:	50 μs
Controller/Processor:	PC-based

Table 2.3: Specifications of the BLR developed by *Nakamura and Masuda* [1992].

Radar system:	Monostatic pulse radar
Operating frequency:	1357.5 MHz
Antenna:	One parabolic antenna
Aperture:	12 m^2 (4 m in the diameter)
Beamwidth:	5°
Gain:	29 dB
Transmitter:	
Peak power:	1000 W (maximum)
Average power:	50 W (maximum)
Bandwidth:	8 MHz
Pulselength:	0.5~6 μs (variable)
IPP:	40~100 μs (variable)

There is a RASS observation as one of the important applications of the BLR [*Tsuda et al.*, 1994d]. RASS is an observation technique to estimate a vertical profile of the temperature by using the acoustic wave together with the radar. An

acoustic wave transmitted aside the radar propagates upward with the speed of sound. The radar is used to detect echoes reflected by the transmitted acoustic wave, and measures the motion of the wave front. Thus, by using the radar, we can observe the speed of sound above the radar. Temperature profile can be observed since the speed of sound is mainly a function of temperature [*May et al.*, 1990]. When the wavelength of the acoustic wave is half of the radar wavelength, the Bragg condition is satisfied, and the radar can detect the most intense echoes. For the wavelength of the BLR of 0.22 m, the acoustic wave with the frequency around 3 kHz is suitable because the wavelength of the acoustic wave becomes 0.11 m at the temperature of 0°C.

A Doppler power spectrum shown in the upper panel of Figure 2.3(a) is expected to obtain by the RASS observation mode. The clutter echo appears at the zero Doppler component, the atmospheric echo around it, and the RASS echo at around 350 m s^{-1}. In order to improve velocity resolution, the number of FFT points must be very large to maintain the maximum velocity of 370 m s^{-1}. For example, when the number of FFT points is 2048, the velocity resolution becomes approximately 0.36 m s^{-1}. However, such number of FFT is difficult to calculate in the real-time. One of the idea is to shift the receiving frequency from the transmitting frequency for around 3 kHz. For our BLR system, this is feasible by shifting the frequency of the local oscillator (LO). The frequency shift of 3 kHz was selected since it corresponds to an acoustic velocity of 331 m s^{-1} at temperature around 0°C. As shown in Figure 2.3(b), by shifting the LO frequency, the velocity resolution becomes 0.39 m s^{-1} even with the number of FFT points of 128.

A problem of this technique is that the clutter and the atmospheric echoes contaminate the RASS echo due to the aliasing effect. In Figure 2.4, with the receiving frequency shifted of 3 kHz, Nyquist limit (the velocity range of the Doppler spectra) is shown by an area without hatching. Positions of the clutter echo due to aliasing are shown by cross symbols. The number of coherent integrations cannot be selected freely because of the limitations of the hardware (see Table 2.4). The dashed lines show the positions of the RASS echoes corresponding to the temperature of −30°C, 0°C, and +30°C, respectively. The lateral bars crossing the cross symbols indicate the area where atmospheric echoes (±10 m s^{-1}) may appear due to aliasing. If the number of coherent integrations is selected 44 and 36, RASS echoes can be separated from the clutter and the atmospheric echoes, and the temperature can be safely estimated for the low and high temperature cases, respectively.

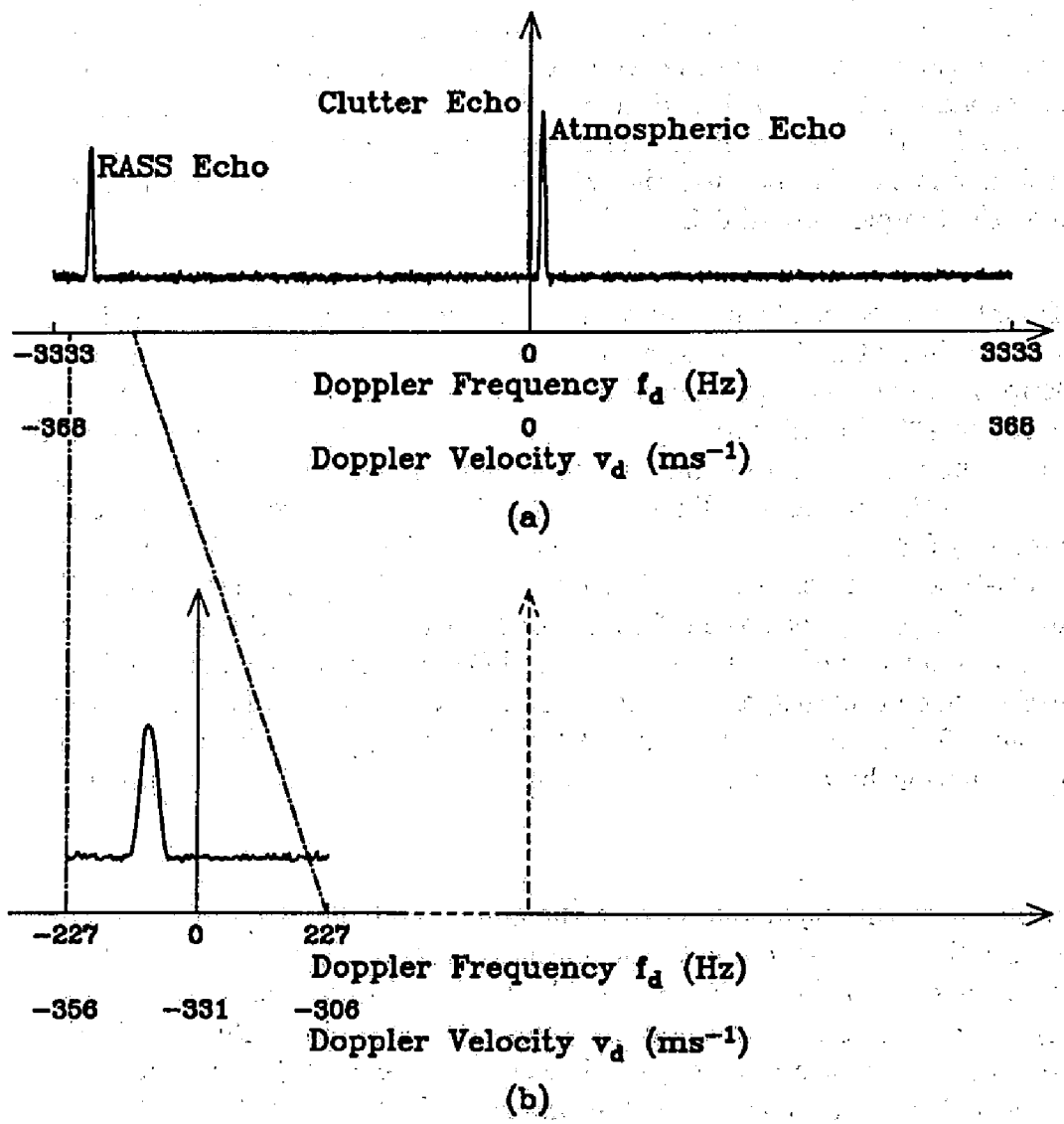

Figure 2.3: A Doppler spectrum expected to obtain by the RASS observation mode. (a) indicates the case by using the usual observation mode. (b) indicates the case by using the RASS observation mode with the receiving frequency shift of 3 kHz.

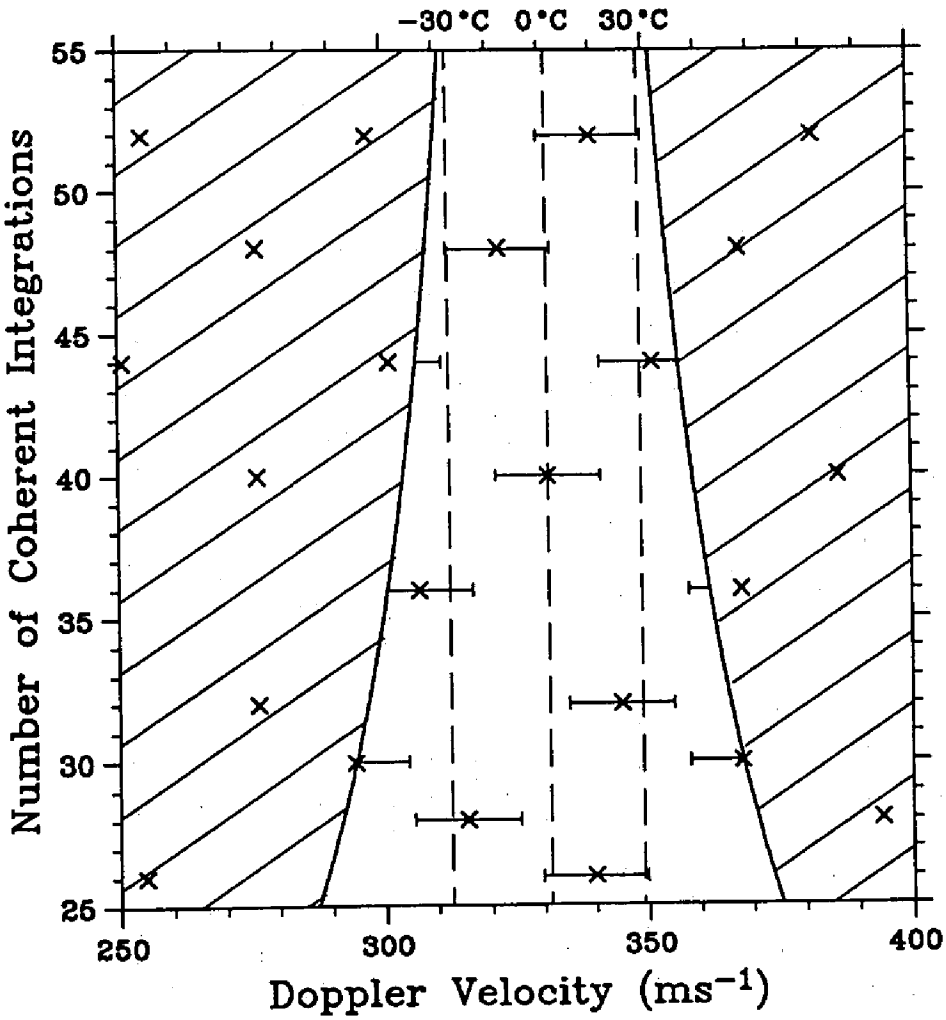

Figure 2.4: The range of the Doppler velocity expected with the receiving frequency shift of 3 kHz (an area without hatching). Cross symbols (×) show positions of the clutter echo due to aliasing. Dashed lines show the positions of the RASS echoes corresponding to the temperature of −30°C, 0°C, and +30°C, respectively. Lateral bars crossing the cross symbols indicate the area where atmospheric echoes (±10 m s^{-1}) may appear due to aliasing.

Table 2.4: The number of integrations (NCOH) performed in the coherent integrator (hardware; HW) and in the signal processing unit (software; SW), respectively, for the number of coherent integrations of 1–256.

NCOH	HW	SW	NCOH	HW	SW	NCOH	HW	SW
1	1	1	18	9	2	72	9	8
2	2	1	20	10	2	80	10	8
3	3	1	22	11	2	88	11	8
4	4	1	24	12	2	96	12	8
5	5	1	26	13	2	104	13	8
6	6	1	28	14	2	112	14	8
7	7	1	30	15	2	120	15	8
8	8	1	32	16	2	128	16	8
9	9	1	36	9	4	144	9	16
10	10	1	40	10	4	160	10	16
11	11	1	44	11	4	176	11	16
12	12	1	48	12	4	192	12	16
13	13	1	52	13	4	208	13	16
14	14	1	56	14	4	224	14	16
15	15	1	60	15	4	240	15	16
16	16	1	64	16	4	256	16	16

2.2 System description

Table 2.5 and Figure 2.5 show the specifications and the block diagram of the BLR, respectively, which were determined based on the discussions in the previous section. Although some sets of the transmitted pulselength and IPP can be selected, they are only permitted within the condition that the duty ratio (defined by a ratio of the pulselength to IPP) should be equal to or less than 2%. The minimum range resolution is 100 m corresponding to the pulselength of 0.67 μs. The hardware system of the BLR consists of mainly five parts of (i) an antenna unit; (ii) a transmitter unit; (iii) a receiver unit; (iv) a data acquisition unit, and (v) a signal processing unit. In the observations with using the BLR, the radio frequency (RF) signal amplified in the transmitter unit is radiated from a parabolic antenna through a SF cable. The weak signal scattered by atmospheric turbulence is gathered by the antenna and is transferred to the receiver unit. The received signal is amplified, is detected, and is converted to a video signal in the receiver unit. The video signal is transferred to the data acquisition unit, and is converted to a digital signal. The digital signal is transferred to the signal processing unit.

Figure 2.6 shows the antenna unit of the BLR. The antenna unit has three parabolic antennas with the diameter of 2 m. In order to estimate the three components of the wind velocity vector, the antennas are now pointed into the vertical and two oblique directions aligned to the east and north at a zenith angle of 15°. The antennas can be steered only manually within one azimuthal direction within ±30° from the zenith. Each antenna is composed of a reflection mirror and the first radiation device of a pyramid horn. Figure 2.7 shows the antenna pattern of the BLR obtained by the computer simulation. The half power beamwidth is 7.6° in the E-plane and 7.7° in the H-plane. The maximum gain is 25 dB, and the first side-lobe level is −23.6 dB in the E-plane and −25.2 dB in the H-plane. It is designed so that the side-lobe level should be as small as possible to save the intensity of the ground clutter echoes to the minimum. It can bear up to the instant maximum wind velocity of 70 m s^{-1} (the average wind velocity of 20 m s^{-1}) on the ground in order to be able to observe strong wind such as in a typhoon.

Figure 2.8 shows the detailed block diagram of the transmitter unit composed of an *L*-band transmitter with an output power of 1 kW. The sine wave carrier of 1197.5 MHz generated by the stable local oscillator (STALO) is fed to the mixer of the transmitter and receiver units, respectively. In the mixer of the transmitter unit, the STALO signal is modulated with a pulsed CW (continuous wave) of 160 MHz, and is converted to the RF signal of 1357.5 MHz.

Table 2.5: Specifications of the BLR system.

Radar system:	Monostatic pulse radar
Operating frequency:	1357.5 MHz
Antenna:	Three parabolic antennas
Aperture:	3.1 m^2 (2 m in the diameter)
Beamwidth:	7.6° (half power)
Beam directions:	(Azimuth, Zenith) = (0, 0), (0, −30° ∼30°), (90°, −30° ∼30°)
Beam shape:	Pencil beam
Gain:	25 dB
First side-lobe level:	−24 dB
Fast Antenna switcher	
Form:	SPST switch
Loss:	1.8 dB
Isolation:	60 dB
Transmitter:	
Peak power:	1000 W (maximum)
Average power:	20 W (duty ratio 2.0%) (maximum)
Bandwidth:	4 MHz
Pulselength:	0.67, 1.0, 2.0 μs (variable)
IPP:	50, 100, 200 μs (variable)
Amplifier:	High power transistor amplifier
Receiver:	
Form:	Double super heterodyne
Output signal:	I and Q video
Bandwidth:	2.0, 1.5, 0.7 MHz (variable)
Noise figure:	3.5 dB
Dynamic range:	60 dB
Minimum receivable power:	−110 dBm
Data acquisition unit:	
Sampling frequency:	2.0, 1.5, 0.7 MHz (variable)
A/D converter:	12 bits
Coherent integrations:	1∼16 (variable)
Memory capacity:	8 Mbytes × 3
Interface:	SCSI-II

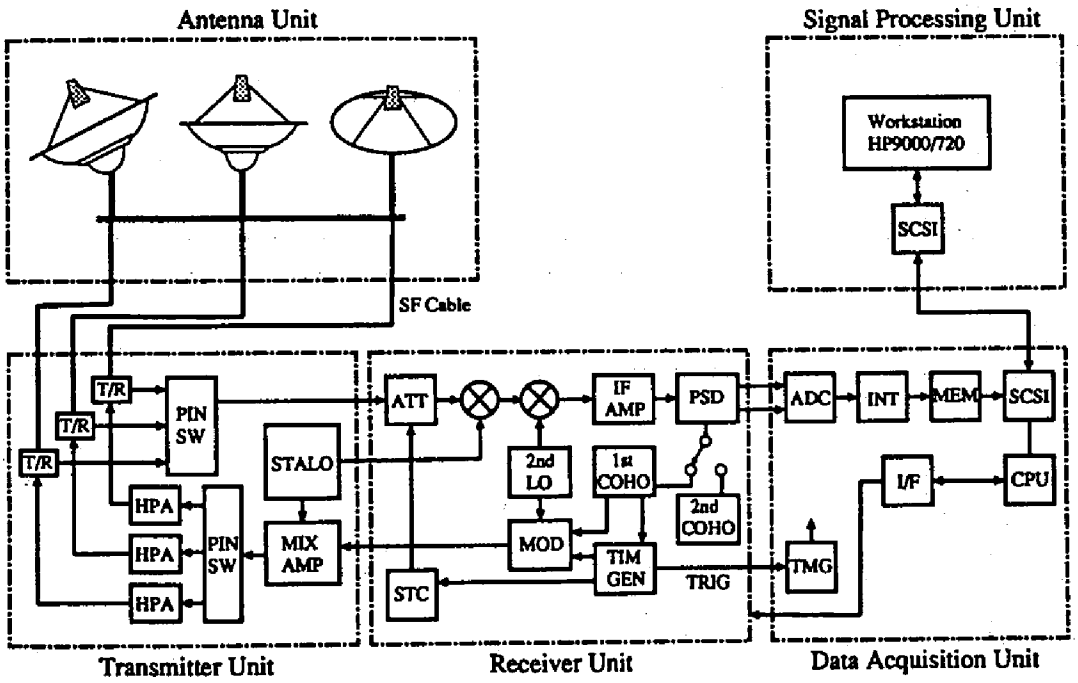

Figure 2.5: Block diagram of the BLR.

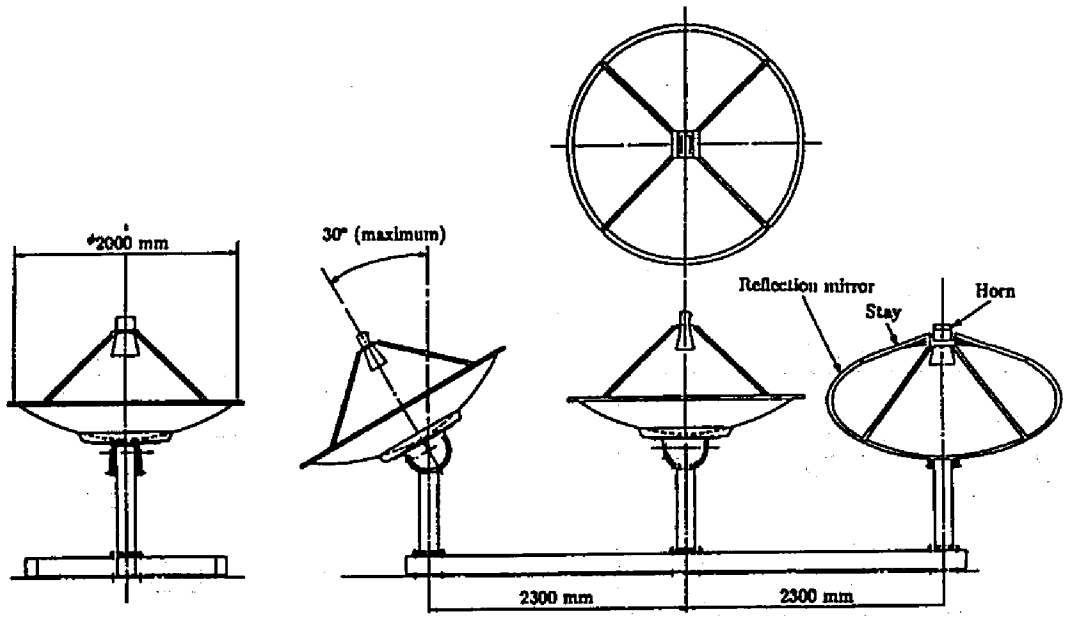

Figure 2.6: Antenna unit of the BLR.

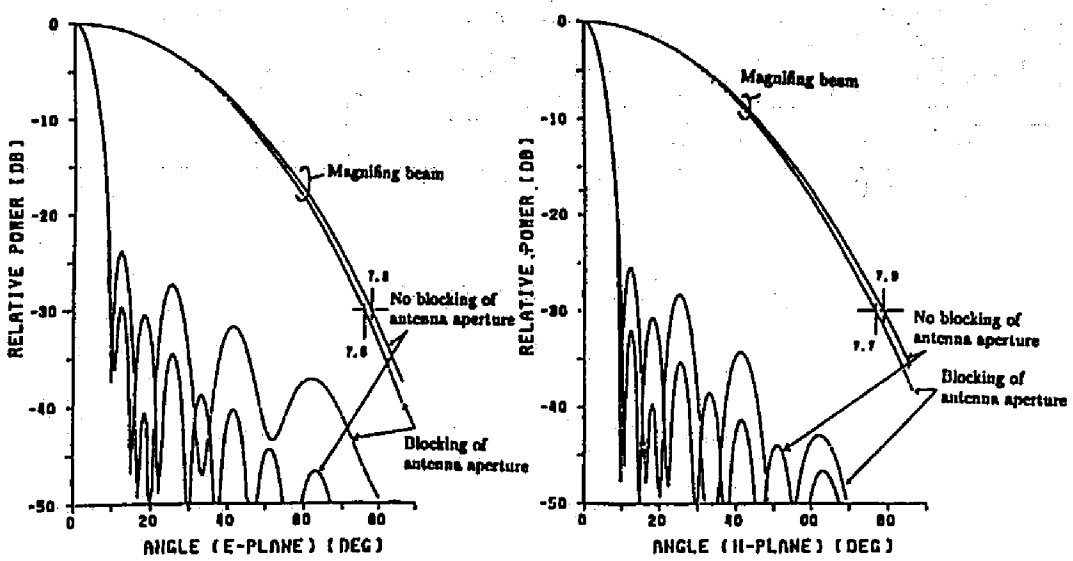

Figure 2.7: Antenna pattern of the BLR (results of the simulation).

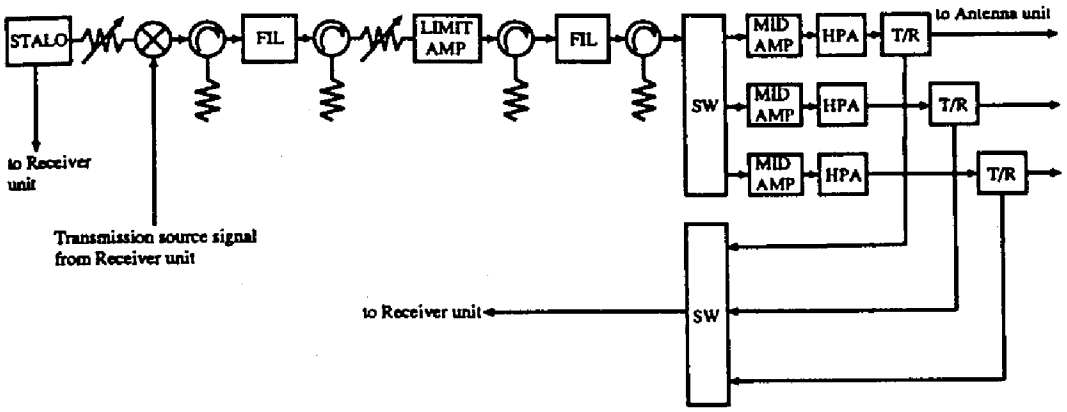

Figure 2.8: Block diagram of the transmitter unit.

The transmitter unit has three sets of mid-amplifiers and high power amplifiers. We use a pin switch, which has the isolation of more than 80 dB and the switching speed of 150 ns, in low power stage to switch the antennas, and can quickly change beam directions. The RF signal is amplified to the output power of 1 kW by the mid-amplifier and the high power amplifier. This RF signal is transmitted from an antenna through a TR switch composed of a circulator, which protects the receiver from damage caused by the high power transmitter during the transmission. The transmitted radiowave is backscattered toward the radar. The radar echo is fed to the receiver unit through the TR switch.

Figure 2.9 shows the block diagram of (a) the mid-amplifier and (b) the high power amplifier used in the transmitter unit. They are composed of six and five transistors, respectively. The first and the second step transistors of the mid-amplifier are A-class ones in order to amplify the signal of relatively low power. The amplifiers of the last three stage are all C-class amplifiers. The high power amplifier is driven by the mid-amplifier. All transistors of the high power amplifier are used as C-class ones and have the same performance.

Figure 2.10 shows the detailed block diagram of the receiver unit. The received RF signal passes through the limiter and is attenuated by a sensitivity time control (STC) circuit in order to seemingly extend the dynamic range. The STC circuit attenuates the signal scattered by the targets in range closer than a few hundred meters to limit the dynamic range within 60 dB[1]. The RF signal passing through the STC circuit is pre-amplified by a low noise amplifier. The RF signal

[1]Since actually the effects of STC were not so good and the estimation of the echo intensity became difficult by using STC, we have not used STC in routine observations.

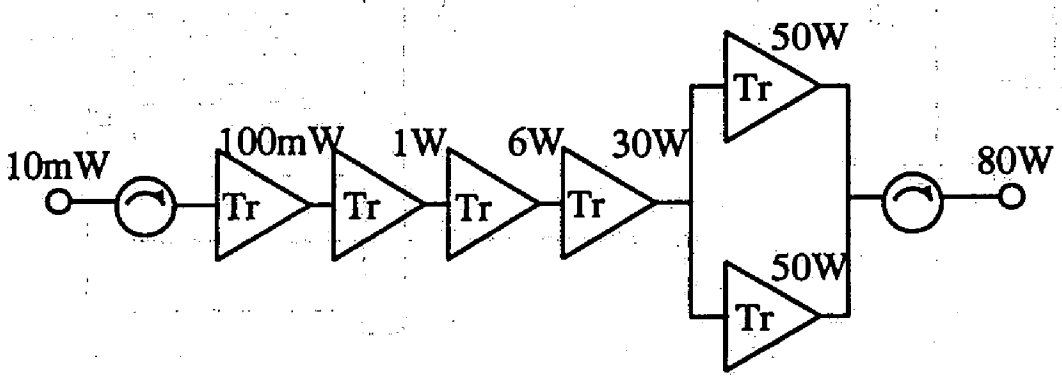

(a)

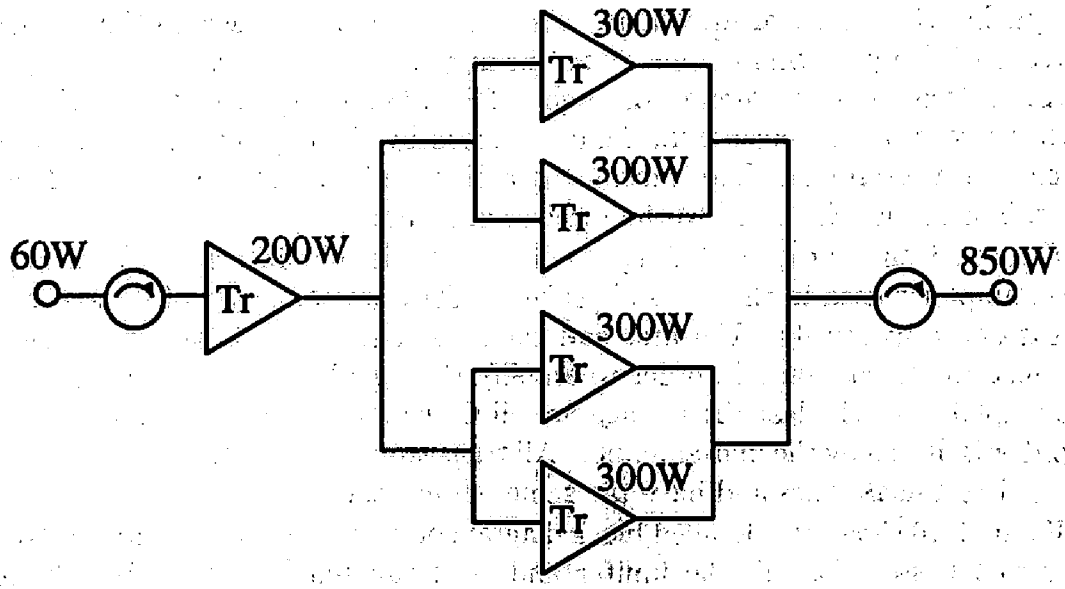

(b)

Figure 2.9: Block diagram of (a) the mid-amplifier and (b) the high power amplifier.

is down-converted with the STALO signal fed from the transmitter unit to a first intermediate frequency (IF) of 160 MHz. The first IF signal is down-converted with a second LO signal of 128 MHz to a second IF of 32 MHz. After amplified in the IF amplifier, the IF signal is detected by the phase detector which produces a time series of sine (I) and cosine (Q) components of the received signal. This detected video signal is fed to the data acquisition unit. The imbalance between I and Q video is less than 2° in phase. The bandwidth B of the IF amplifier is the function of the transmitted pulselength Δt, and we use $B = 1.4/\Delta t$. The minimum detectable signal of the receiver is -110 dBm with the bandwidth of 0.7 MHz.

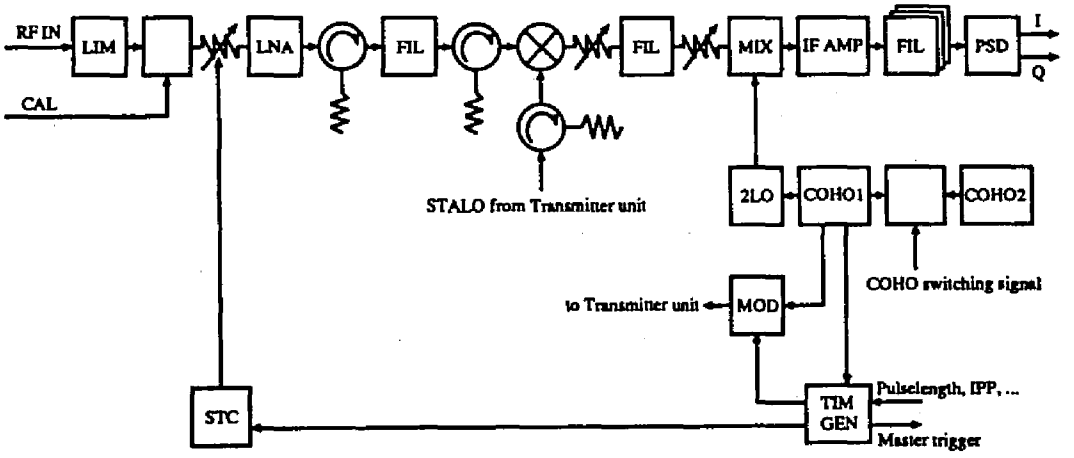

Figure 2.10: Block diagram of the receiver unit.

The pulsed CW is produced as following. First, a coherent local oscillator (COHO) signal of 32 MHz, which has the short stability of 10^{-9} and the daily variation of 10^{-7}, respectively, to the frequency of 32 MHz, is converted to the pulsed CW of 32 MHz in a pulse circuit. This signal is modulated with the second LO signal of 128 MHz, and is converted to the pulsed CW of 160 MHz. For RASS observations, the receiver unit has a second COHO lower about 3 kHz than the first COHO used in usual observations (see Section 2.1 for details). The switch between the two COHOs has the isolation of 80 dB in order to reduce ghost image generated by another COHO.

Figure 2.11 shows the detailed block diagram of the data acquisition unit. The I and Q video signal fed from the receiver unit is converted to a digital signal by the analogue-to-digital converter (ADC). The digital signal is coherently integrated by a coherent integrator, and stored in the memory unit. The numerical

expression of the coherent integrator and of the ADC are 16 bits and 12 bits, respectively. Therefore, the number of coherent integrations is limited up to 16 (4 bits) times in order not to loose any bit of information. When we need coherent integrations of more than 16 times, additional integrations over 16 times should be performed in the signal processing unit (see Table 2.4). The capacity of the memory unit is 8 Mbytes for one beam, i.e. 24 Mbytes for all three beams. For example, when an observation is set to use FFT points of 512 and the number of incoherent integrations of 32, the necessary memory size is exactly 8 Mbytes for one beam. The stored data are transferred to the signal processing unit.

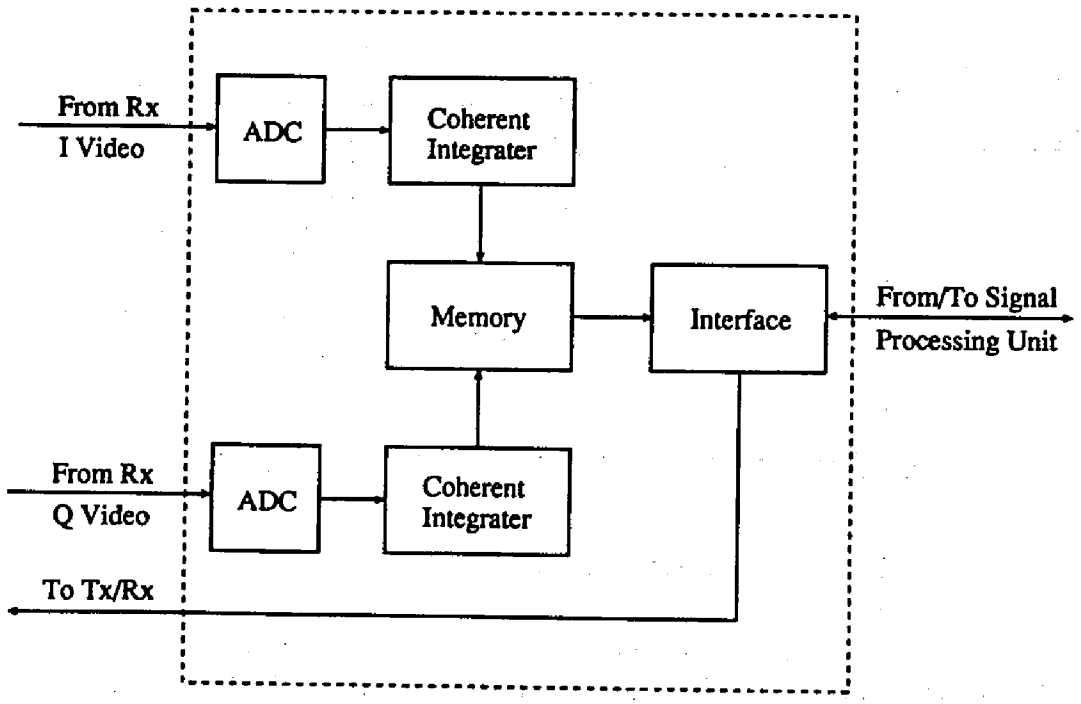

Figure 2.11: Block diagram of the data acquisition unit.

The BLR system uses an engineering workstation as the signal processing unit. This workstation can execute one 1024-points of fast Fourier transformation (FFT) in about 12 ms and estimates one set of spectral parameters in about 3 ms. In order to interface the data acquisition unit with the signal processing unit, the small computer system interface (SCSI) is used because this is a standard interface, and can transfer data with the maximum speed of 5 Mbytes s^{-1}. Since this SCSI is very popular for personal computers and workstations, it is not difficult to utilize different types of computers as a signal processing unit of

the BLR. All the parameters to control the system and the observed data are transferred to and from the signal processing unit through the SCSI.

2.3 Software configuration

The functions of the BLR are mainly separated in following three parts:

i) A part to transmit and receive radiowave, and to obtain time series data, which depends on the hardware;

ii) A part to transfer the time series of data to the workstation, which depends on the interface controlled by the software;

iii) A part to process the data, which depends on the software.

It is impossible that (i) and (ii) are performed in parallel due to the limitation of the hardware. Since the software system used in the BLR observation is variously contrived, (i) and (iii), and a part of (ii) and (iii) can be performed in parallel as shown later in detail.

Specifications of the workstation of the BLR is shown in Table 2.6. The operating system is UNIX which is a very popular multi-user and multi-task operating system, and has excellent user interface. Our observation software is composed of several programs utilizing the multi-task function. UNIX has system calls for the "creation of process" that one program executes another new program. There are also several system calls to control the execution of multi-task processes. They are inter-process communications: "semaphore" and "shared-memory."

The "semaphore" is used to synchronize execution of two or more processes. Figure 2.12 illustrates this function. Program A controls the timing of the execution of Program B. Both programs are simultaneously started at time "a." Program A reset the semaphore at time "b," and proceed to a next step. When Program B tries to reset the semaphore at time "c," it fails because the semaphore is already reset by Program A. Then, Program B starts to wait for the semaphore to be set by other processes. Program B does not use the CPU resources during this waiting. When Program A sets the semaphore at time "d," Program B is awaken, succeeds to reset the semaphore, and starts to proceed to a next step.

Usually, separated programs cannot access the same memory address in UNIX. The "shared-memory" is the function to access same memory address by separated programs. UNIX adopts a virtual memory system which regards the hard disk as memory and expands memory spaces in appearance. However, reading from and writing to hard disk is much slower than real memory. We can lock

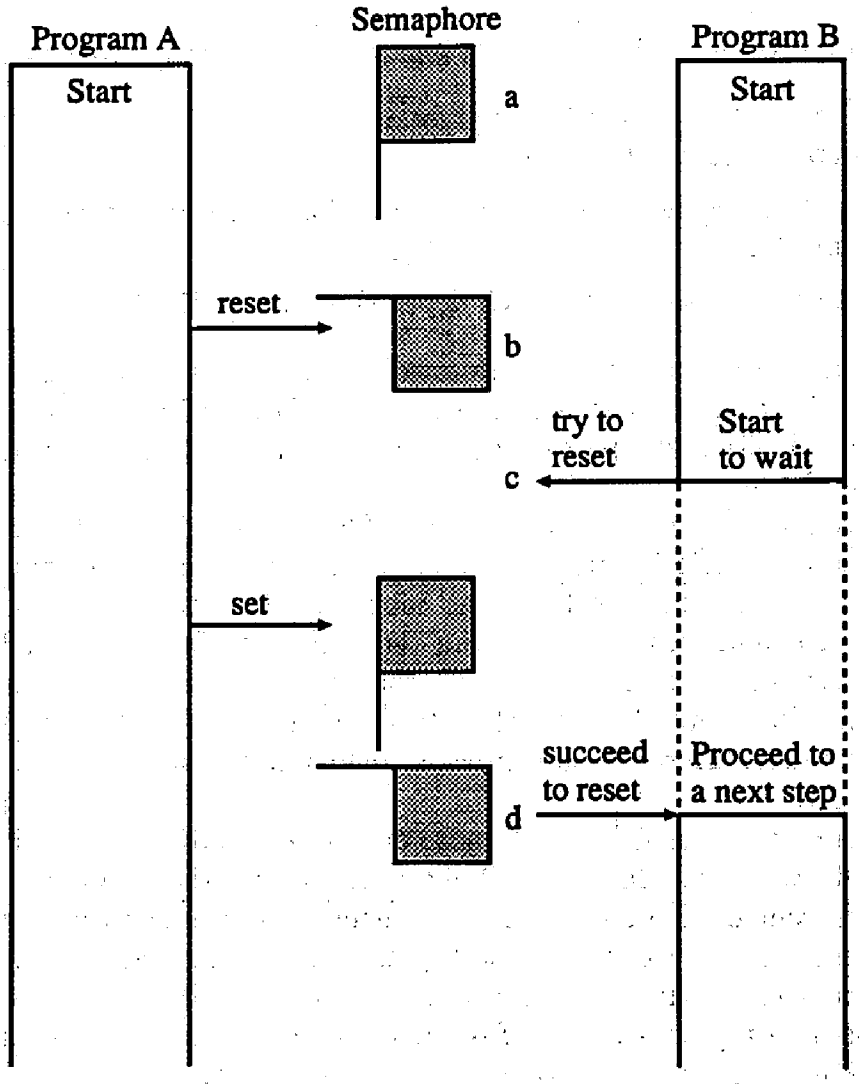

Figure 2.12: A schematic diagram to explain the function of the semaphore in the UNIX operating system.

Table 2.6: Specifications of the workstation (HP9000/720) [*Hewlett Packard*].

Operating system:	HP-UX
CPU:	PA-RISC (50 MHz)
Performance:	17.2 MFLOPS, 57 MIPS (value of catalog)
	8.8 MFLOPS (value measured by us)
Main memory:	32 Mbytes
Interface to the BLR:	SCSI-II (differential)
Data transfer rate:	5 Mbytes s^{-1} (maximum)
Hard disk:	420 Mbytes(inner), 1.3 Gbytes(outer)
Sequential access rate:	6 Mbytes s^{-1}
DAT:	1.3 Gbytes (tape of 120 min)
Data transfer rate:	1.5 Mbytes s^{-1} (maximum)

the "shared-memory" within the real memory. Then, all of the access to the "shared-memory" can be performed to the real memory.

The software to control observations and to process the data must have the performance to utilize the excellent hardware of the BLR. An observer controls all the radar system with this observation software. The performance of the observation software determines the easiness of the radar operations. The observation software should have following functions:

i) The function to set up observation parameters and to control observations;

ii) The function to schedule the order of the observation;

iii) The function to process the data: the coherent integration, FFT, the estimation of spectral parameters and so on;

iv) The function to transfer data from (to) the radar to (from) the workstation;

v) The function to preserve data in DAT;

vi) The function to graphically display the observation data simultaneously with the observation.

Before starting an observation, it is needed to set up observation parameters — the pulselength, the number of coherent and incoherent integrations, the FFT points and so on — to the radar. In this observation software, the observer does not need to set up observation parameters for every observation, but makes a observation parameter file as shown in Figure 2.13. The symbol "%" in the first column expresses a comment line. The observation parameters are set by the

substitution of a value in the variable. This example shows that the number of coherent integrations (`ncoh`) is 64 and the number of FFT points (`nfft`) is 128. The "Observation Control" program reads the file and interprets the observation parameters into the binary data transferred to the radar. When observation parameters would conflict with the limitation of the hardware — duty ratio is equal to or less than 2%, the number of coherent integrations by the coherent integrator is equal to or less than 16 and so on, — "Observation Control" displays an error message, and shows a recommendatory value.

In order to start an observation, the command "observe" should be executed. The file name of the observation parameter, times of the observation start and end, the number of observations can be specified by the operands. We can make observation schedule by using "shell script" of UNIX. The observations can be automatically changed in the schedule file as shown in Figure 2.14. The observation is orderly conducted according to the "observe" command lines. Loop, branch, condition judgment etc. can be used in the "shell script." In the example of Figure 2.14, the first observation is found in the line 4, which is to conduct the observation with the parameter file "para1" to 12:00 on 14 February. The next line corresponds to the next observation which is to start at 13:00 and to obtain 10 records of data. Afterwards, according to the loop from line 7 to line 9, observations start at 0:00, 2:00, and 4:00 on 15 February for one hour for each.

The observation software used in the BLR system is composed of "Observation Control," "Signal Processing," "Data Transfer," "DAT Control," and "Quick Look" programs as shown in Figure 2.15. "BLR" in this figure denotes the whole system except for the workstation. When an observer starts an observation, by executing the "Observation Control," the observation parameters are read from the parameter file, and the "shared-memory" and the "semaphores" are initialized. The "shared-memory" is used to share the observation data etc. with other programs.

Figure 2.16 shows the time chart of the observation software. The "Observation Control" executes the "Signal Processing" automatically, then the "Signal Processing" executes the "Data Transfer." The "Data Transfer" sends the observation parameters to the "BLR." Then, it starts the observation, and requests for the data transfer by sending commands to the "BLR." Afterwards, it waits for the data ready. After an observation is over, the "Data Transfer" transfer the time series of data from the "BLR" through the SCSI, and write them into the "shared-memory." When the "Data Transfer" takes the data corresponding to one beam, it sends a signal by using the "semaphore" to the "Signal Processing." The "Signal Processing" starts the calculations of coherent integrations, FFT, incoherent integrations, and the estimation of spectral parameters which is de-

```
%
% Constant Definitions ( General purpose )
%
#define OFF 0
#define ON 1

#define STD 1
#define RASS 2

%
% Constants for This Parameter File
%
#define STC OFF
#define LOCAL_OSC STD

%
%------------------------------ Memo ------------------------------
%
% Comment ( 80 characters )
%
comment = "Continuous observations."
%
% Beam Directions ( Azimuth, Zenith (degree) )
%
beam(1) = (  0,  0 )
beam(2) = (  0, 15 )
beam(3) = ( 90, 15 )
%
% Receiver Gain ( MGC ) ( 0 - 50 )
%
rx_gain = 25
%
%------------------------------------------------------------------
%
% Number of Coherent Integrations ( See Other Table )
%
ncoh = 64
```

Figure 2.13: An example of the observation parameter file. (Continues)

```
%
% Number of Incoherent Integrations ( 1 to 32 )
%
nicoh = 32
%
% Number of FFT Points ( Only Power of 2 )
%
nfft = 128
%
% Range Resolution ( 100, 150, or 300 (m) )
%
resolution = 150
%
% Sampling Interval ( 75, 100, or 200 (m) )
%
sample_int = 100
%
% Receiver Bandwidth ( 2000, 1500, 750 (kHz) )
%
bandwidth = 1500
%
% Inter Pulse Period ( 50, 100, or 200 (micro sec) )
%   Range of Aliasing : ipp = 50 -> 7500m, 100 -> 15000m, 200 -> 30000m
%
ipp = 50
%
% Sampling Position ( 0 to 255 )
%
sample_pos = 0
%
% Number of Height Points ( Note Range Aliasing )
%   nhigh(i) = 0 --> not using beam i
%
nhigh(1) = 64
nhigh(2) = 64
nhigh(3) = 64
```

Figure 2.13: (Continues)

```
%
% Sampling Start Range (m)
%  sample_start = sample_int * (sample_pos + non-negative integer)
%
sample_start = 0
%
% STC ( ON or OFF )
%
stc = STC
%
% Local Oscillator ( STD( LO1 only ) or RASS( LO1 and LO2 ) )
%
local_osc = LOCAL_OSC
%
% Observation Program Name
%
program = "dopplfit"
%
% Number of Fitting Points
%   nfit = 0 --> not fitting
%
nfit = 20
%
%---------------------------- Comment ----------------------------
%
% Number of Beam Directions(nbeam) <-- Number of Height Points
% Antenna No. <-- Number of Height Points
%
% Observation Mode(mobs) <-- Observation Program
% Transmitted Pulthwidth(jpwdth) <-- Range Resolution
%
% Latitude(platit) <-- Environment Variable
% Longitude(plongi) <-- Environment Variable
% Above Sea Level(sealvl) <-- Environment Variable
% Place Name(place) <-- Environment Variable
%
%-----------------------------------------------------------------
```

Figure 2.13: (Continued)

```
 1 #!/bin/csh
 2       onintr TERMINATE
 3
 4       observe para1 99999999 02141200
 5       observe para2 02141300 10
 6
 7       foreach st (02150000 02150200 02150400 )
 8            observe para3 $st 99990100
 9       end
10
11       exit
12
13 TERMINATE:
14       echo 'terminate schedule'
15       set pid = `ps -e | awk ' $4 == "observe" { print $1 } '`
16       if ( $pid != "" ) then
17            kill $pid
18            wait
19       endif
20
21 ##########################################################################
22 #                                                                        #
23 # observe file1 [ file2 ... file5 ] start end                            #
24 #   or                                                                   #
25 # observe file1 [ file2 ... file5 ] start number                         #
26 #                                                                        #
27 #     file? : File name of an observation parameter                      #
28 #     start : Start time [MMDDhhmm] (99999999 -> immediate start)        #
29 #     end   : End   time [MMDDhhmm] (9999hhmm -> observation period)     #
30 #     number: Number of observations [nnnn]                              #
31 #                                                                        #
32 ##########################################################################
```

Figure 2.14: An example of the schedule file.

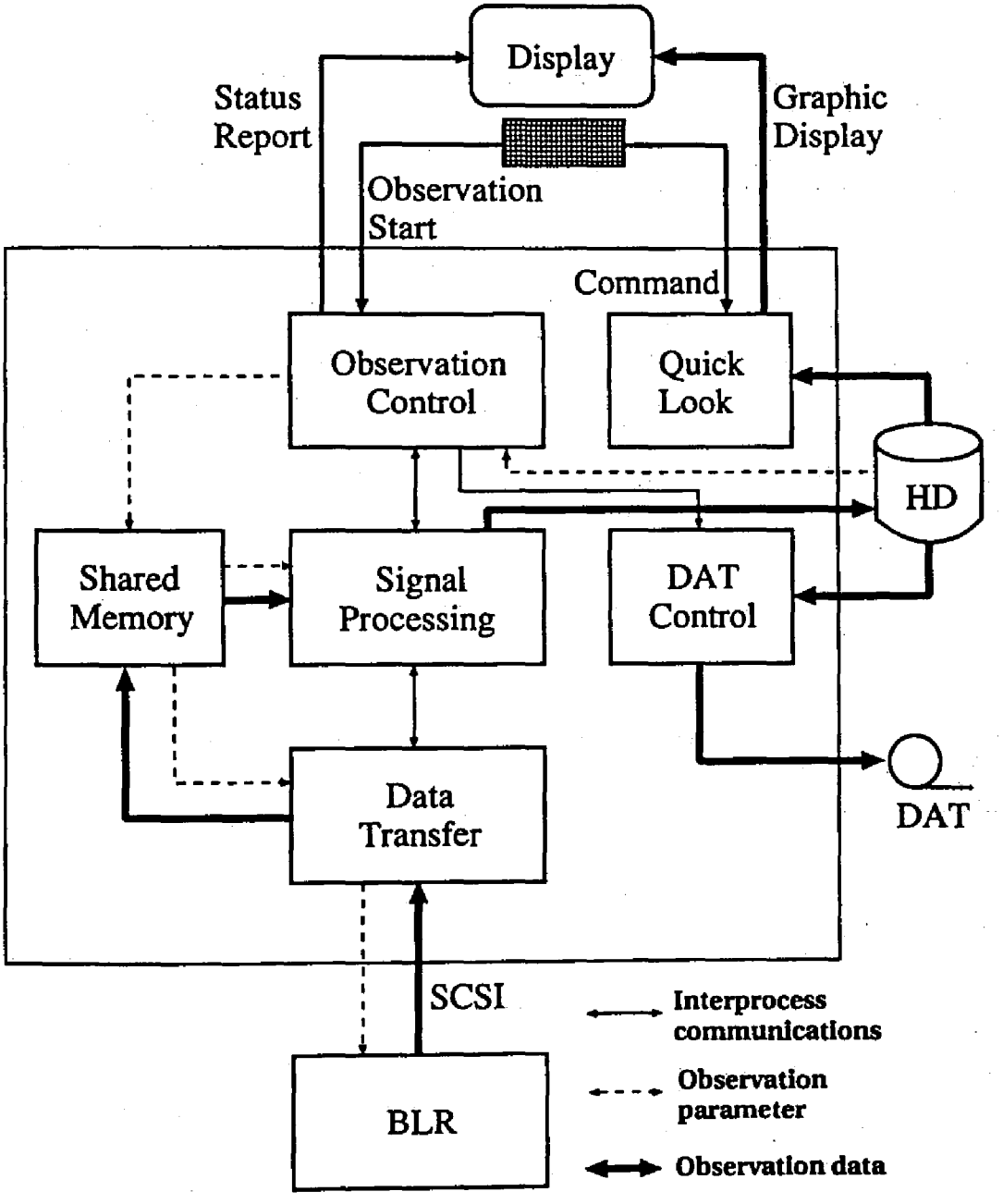

Figure 2.15: Block diagram of the observation software.

scribed in the following section. Meanwhile, the "Data Transfer" starts receiving data of the next beam from "BLR," and write them in the "shared-memory." When the data of all beams are transferred from "BLR," the "Data Transfer" starts the next observation without waiting for the finish of the calculations by the "Signal Processing." The spectra and the spectral parameters calculated by "Signal Processing" are also written in the "shared-memory." When all the spectra and estimated parameters are ready in the "shared-memory," the "Signal Processing" writes them into one of the 10 areas allocated in the hard disk. As shown in Figure 2.17, the data are recorded in the same area for a while. The data size is usually a few Mbytes for observations for one hour. When the data size in one area exceeds 100 Mbytes, the "Observation Control" executes the "DAT Control," and let the "Signal Processing" change the area to the next unused one. The "DAT Control" reads the data recorded in the hard disk and writes them into DAT without stopping observations. Since UNIX does not support to put labels to the files on the DAT, we decided to use the label structure of ANSI standard (see Table 2.7). Then, the file name, the recorded time and so on are found in the label of the observation data file.

Table 2.7: The label structure of ANSI standard used to record the BLR data into DAT. (Continues)

(a) Volume label fields.

Character position	Field (length in bytes)	Contents
1–3	Label identifier (3)	Alphabetic characters VOL
4	Label number (1)	Numeric character 1
5–10	Volume identifier (6)	Volume label consists of ASCII characters.
11	Accessibility (1)	Volume accessibility; provides compatibility with some non-VAX/VMS systems. A space indicates no restrictions.
12–37	Reserved (26)	Spaces
38–50	Owner identifier (13)	Volume ownership. The contents of this field are used for volume protection.
51	DIGITAL standard version (1)	Numeric character 1
52–79	Reserved (28)	Spaces
80	Label standard version (1)	Numeric character 3

Table 2.7: (Continues)

(b) First file header label fields.

Character position	Field (length in bytes)	Contents
1–3	Label identifier (3)	Alphabetic characters HDR
4	Label number (1)	Numeric character 1
5–21	File identifier (17)	A user-supplied file name and file type
22–27	File-set identifier (6)	Same as the file-set identifier of the first file on the first volume, whether single or multivolume configuration
28–31	File-section number (4)	Numeric characters starting at 0001 and incrementing by 1 for each additional volume with respect to the first volume on which the file begins
32–35	File-sequence number (4)	File number within the volume set for this file; consists of numeric characters, starting at 0001 that indicate the position of this file with respect to the first file of the set
36–39	Generation number (4)	Numeric characters that indicate the unique generation of a file
40–41	Generation-version number (2)	Numeric characters that indicate the version of a particular generation of a file
42–47	Creation date (6)	System stores the date in the Julian format (#YYDDD); the default is the current date
48–53	Expiration date (6)	User specified Julian date (#YYDDD) or default is the creation date, indicating file expires immediately
54	Accessibility (1)	File accessibility; provides compatibility with some non-DIGITAL systems. A space indicates no restrictions.
55–60	Block count (6)	Always 000000 for the HDR1 label
61–73	System code (13)	Identifies the file system that created the file.
74–80	Reserved (7)	Spaces

Table 2.7: (Continued)

(c) Second file header label fields.

Character position	Field (length in bytes)	Contents
1–3	Label identifier (3)	Alphabetic characters HDR
4	Label number (1)	Numeric character 2
5	Record format (1)	Character definition: F (fixed-length), D (variable-length) or S (spanned record)
6–10	Block length (5)	Five numeric characters specifying the maximum number of characters per block
11–15	Record length (5)	Numeric characters indicating the record length for fixed-length records or the maximum record length for variable-length records
16	System-dependent (1)	Space
17–36	System-dependent (20)	Spaces available for future use.
37	Form control (1)	Defines the carriage control applied to the records within a file: A (First byte of record contains FORTRAN control characters), M (Record contains all form control information) or Space (Line feed/carriage return will be inserted between records (default))
38–50	System-dependent (13)	Spaces available for future use.
51–52	Buffer offset (2)	The numeric characters 00
53–80	Reserved (28)	Spaces

(d) Third file header label fields.

Character position	Field (length in bytes)	Contents
1–3	Label identifier (3)	Alphabetic characters HDR
4	Label number (1)	Numeric character 3
5–68	VAX-11 RMS attributes (64)	Files-11 record attributes that override information in fields of the HDR2 label
69–80	System-dependent (12)	Spaces

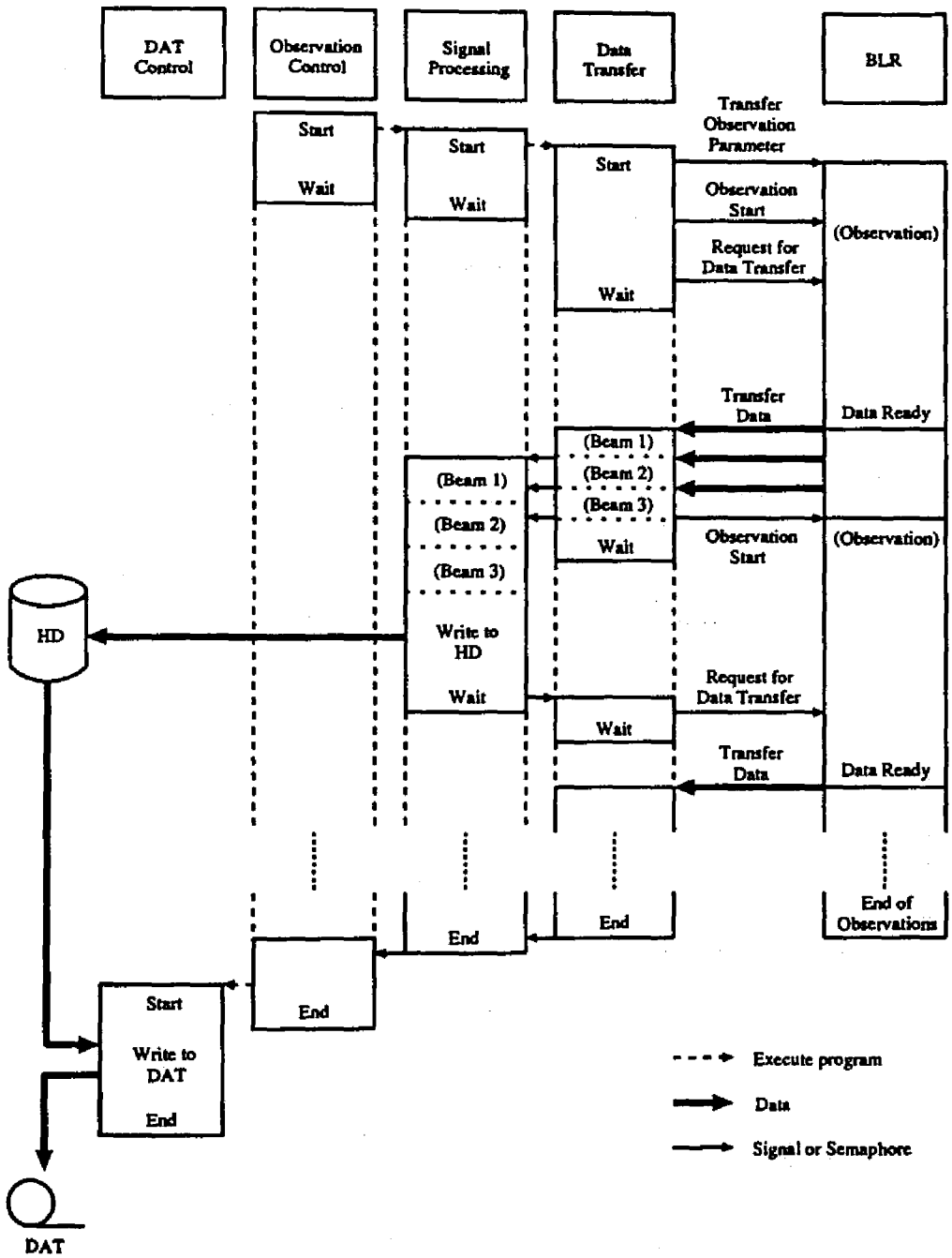

Figure 2.16: Time chart of the observation software.

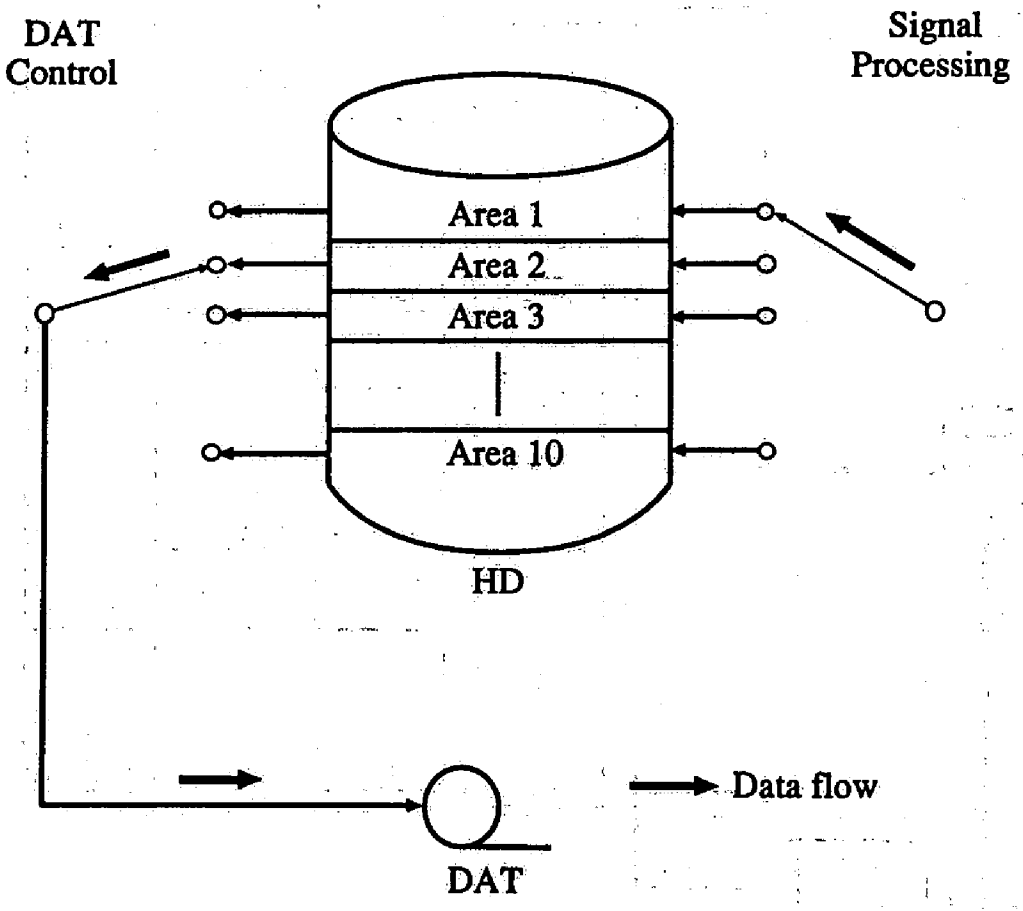

Figure 2.17: A schematic diagram to show how to record data to the hard disk and DAT.

We have added header information — observation parameters, observation time and so on — to every observation data so that we can easily refer to the observation parameters. The format of the header is shown in Table 2.8. The header includes the areas to write a comment and to be reserved for the future use.

In order to monitor the data during the BLR operation, there is a "Quick Look" executed independently. The "Quick Look" reads the data from the hard disk, and plots them to the graphic display of the workstation or of another computer system.

When observation parameters are the values shown in Table 2.9, the data size that should be transferred from the radar to the workstation is

$$\begin{aligned} & N_{\mathrm{FFT}}(N_{\mathrm{coh}}/16)N_{\mathrm{high}}N_{\mathrm{icoh}}N_{\mathrm{beam}}N_{\mathrm{I,Q}} \times 2 \\ = \; & 128 \times 64/16 \times 64 \times 32 \times 3 \times 2 \times 2 \\ = \; & 12 \text{ [Mbytes]}. \end{aligned} \tag{2.1}$$

Since the data transfer rate of SCSI of the BLR is about 0.8 Mbytes s^{-1}, it takes $12/0.8 = 15$ s to transfer all data. Since the observation time is

$$\begin{aligned} & T_{\mathrm{IPP}}N_{\mathrm{coh}}N_{\mathrm{FFT}}N_{\mathrm{icoh}}N_{\mathrm{beam}} \\ = \; & 50 \times 10^{-6} \times 64 \times 128 \times 32 \times 3 \\ = \; & 39 \text{ [s]} \end{aligned} \tag{2.2}$$

for three beam directions, the time resolution (the period to obtain data for one profile of three-dimensional wind velocities) is $39 + 15 = 54$ s. In order to obtain the data within the above mentioned period, the signal processing must finish within 39 s that is an observation period of the radar. Since the workstation can execute the calculations including the estimation of spectral parameters in about 6 s, even while "Quick Look" program is running at the same time, the computer performance is enough.

2.4 Data analysis techniques

The signals received by the BLR consist of echoes due to the atmospheric scattering, the noise, and the ground clutter shown in Figure 2.18. The noise is separated into two elements: (i) the sky noise due to the cosmic, the solar, and the atmospheric radiation, and (ii) the noise generated by the receiver itself. For the frequency of 1357.5 MHz, the sky noise temperature is less than 100 K as shown in Figure 2.19 [*Skolnik*, 1980], and the receiver noise temperature is about 670 K if the noise figure is considered to be 3.5 dB. Therefore, the sky

Table 2.8: Format of the header information of the BLR. (Continues)

Int.	Position	Name	Contents
1	1–4	LNBLK	Length of a Data Block ($\geq$512)
2	5–8	NTBLK	Number of Total Blocks (Header, Spectra & Parameters)
3	9–12	NDBLK	Number of Data Blocks (Spectra only)
4	13–16	LNSEG	Length of Segment ($\leq$LNBLK)
5	17–20	NHBLK	Number of Header Blocks
6	21–24	NPBLK	Number of Parameter Blocks
7	25–28	IREC	Record Number (since Observe Program started)
8	29–32	ISTA	Record Start Time (s) (since Epoch)
9	33–36	IEND	Record End Time (s) (since Epoch)
10	37–40	ITIME	Pure Observation Time (ms) ($\neq$IEND$-$ISTA)
11	41–44	MOBS	Observation Mode
			0 : raw data
			1 : FFT-spectra only
			10 : FFT-parameters only
			11 : FFT-spectra & parameters
			2 : FFT-complex spectra (Reserved)
			99 : unknown
12	45–48	MTYPE	Data Type (Reserved)
13	49–52	NCOH	Number of Coherent Integrations
14	53–56	NDATA	Number of FFT Points
15	57–60	NICOH	Number of Incoherent Integrations
16	61–64	MSINT	Sampling Interval (m)
17	65–68	IPP	IPP (μs)
18	69–72	JBWDTH	Receiver Bandwidth (kHz)
19	73–76	JPWDTH	Transmitted Pulthwidth (ns)
20	77–80	JSTC	STC (off : 0, on : 1)
21	81–84	JSAMPL	Sampling Position (0 to 255)
22	85–88	LOCOSC	Local Oscillator (LO1 only : 1, LO1 & LO2 : 2)
23	89–92	NHIGH(1)	Number of Height Points (Beam 1)
24	93–96	NHIGH(2)	Number of Height Points (Beam 2)
25	97–100	NHIGH(3)	Number of Height Points (Beam 3)
26	101–104	NBEAM	Number of Beam Directions

Table 2.8: (Continued)

Int.	Position	Name	Contents	
27	105–108	IAZ(1)	Direction of Beam 1 (°) (Azimuth)	... Memo.
28	109–112	IAZ(2)	Direction of Beam 2 (°) (Azimuth)	... Memo.
29	113–116	IAZ(3)	Direction of Beam 3 (°) (Azimuth)	... Memo.
30	117–120	IZE(1)	Direction of Beam 1 (°) (Zenith)	... Memo.
31	121–124	IZE(2)	Direction of Beam 2 (°) (Zenith)	... Memo.
32	125–128	IZE(3)	Direction of Beam 3 (°) (Zenith)	... Memo.
33	129–132	MSTART	Sampling Start Range (m)	
34	133–136	NFIT	Number of Fitting Points	
35	137–140	RXGAIN	Receiver Gain (dB)	... Memo.
36	141–144	PLATIT	Latitude (°)	... Memo.
37	145–148	PLONGI	Longitude (°)	... Memo.
38	149–152	SEALVL	Above Sea Level (m)	... Memo.
39	153–156	WINDG(1)	Wind Velocity on the Ground ($m\ s^{-1}$) (Vertical)	... Memo.
40	157–160	WINDG(2)	Wind Velocity on the Ground ($m\ s^{-1}$) (Northward)	... Memo.
41	161–164	WINDG(3)	Wind Velocity on the Ground ($m\ s^{-1}$) (Eastward)	... Memo.
42	165–168	RAIN	Rainfall Intensity ($mm\ hour^{-1}$)	... Memo.
43	169–172	PN(1)	Noise Power Density (Beam 1) (Unit : Relative)	
44	173–176	PN(2)	Noise Power Density (Beam 2) (Unit : Relative)	
45	177–180	PN(3)	Noise Power Density (Beam 3) (Unit : Relative)	
46	181–204	RECSTA	Record Start Time [DD-MMM-YYYY hh:mm:ss]	
52	205–216	RECEND	Record End Time [hh:mm:ss]	
55	217–248	PARNAM	Parameter-file Name (32 Bytes)	
63	249–280	PRGNAM	Signal Processing Program Name (32 Bytes)	
71	281–312	PLACE	Place Name (32 Bytes)	... Memo.
79	313–392	COMENT	Comment by User (80 Bytes)	... Memo.
99	393–512		Reserved for the Future (120 Bytes)	

Table 2.9: Typical observation parameters of the BLR.

Parameter	Value
Pulselength:	1 μs
IPP:	50 μs
Number of coherent integrations:	64
Number of incoherent integrations:	32
FFT points:	128
Range resolution:	100 m
Maximum observable horizontal wind velocity:	67.1 m s^{-1}
Resolution of horizontal wind velocity:	1.0 m s^{-1}

noise can be neglected as compared with the receiver noise. The spectrum of the receiver noise is much wider than that of the atmospheric scattering signal and can be regarded as a white noise in Doppler spectra. The ground clutter is the echo scattered by mountains, forests, the sea surface and so on within the side-lobe of an antenna. If the target does not move, the ground clutter appears at the zero Doppler component of the spectrum. However, the spectrum of the ground clutter sometimes shows a little spread because of the fluctuates of the atmospheric refraction or the motion of the ground clutter itself like trees [*Morimoto*, 1985].

The Doppler spectrum of the atmospheric echo can be parameterized with three spectral parameters: (i) the echo power; (ii) the mean Doppler shift (corresponding to the wind velocity), and (iii) the spectral width. As shown in Figure 2.20, by assuming the Gaussian distribution of the spectra, the spectral parameters are estimated by using the least squares fitting method.

The model function to fit to the observed Doppler spectrum is selected to be the Gaussian function [*Woodman*, 1985]

$$g(f) = P_r \exp\left[-\frac{(f - f_d)^2}{2\sigma^2}\right] \tag{2.3}$$

where f is the Doppler frequency and f_d is the mean Doppler shift. The spectral half-width $\sigma_{\frac{1}{2}}$ defined as the one where a power spectral density is half of the maximum P_r is given by

$$\sigma_{\frac{1}{2}} = \sqrt{2 \ln 2}\sigma . \tag{2.4}$$

The echo power $\overline{P_r}$ is then

$$\overline{P_r} = \sqrt{2\pi}\sigma P_r . \tag{2.5}$$

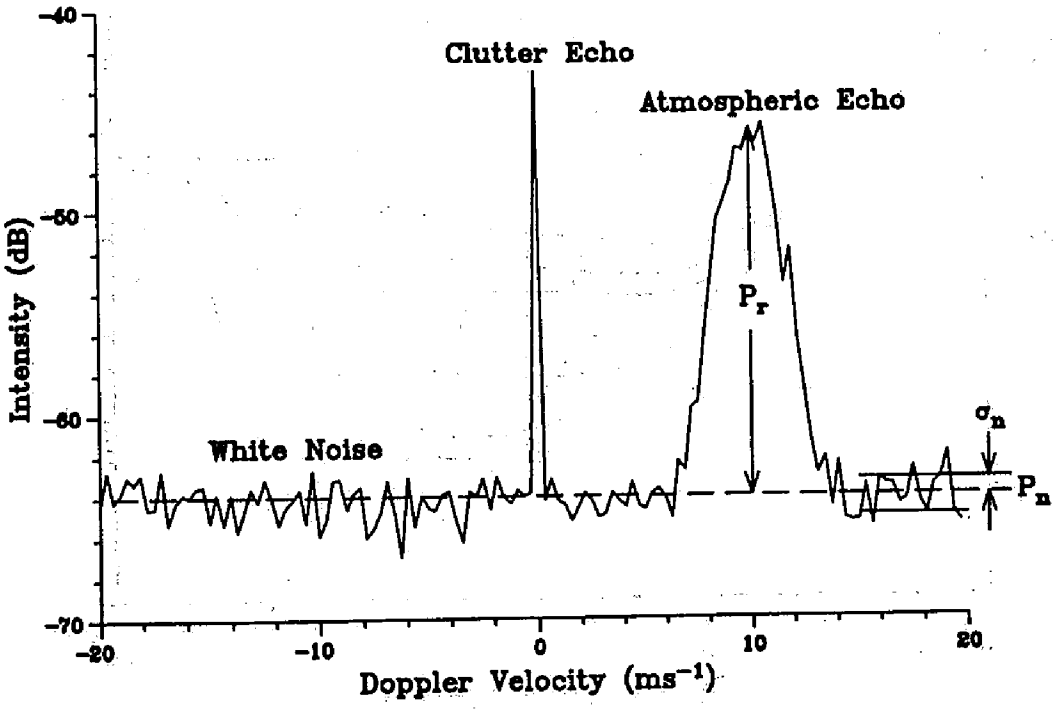

Figure 2.18: An example of the Doppler spectrum.

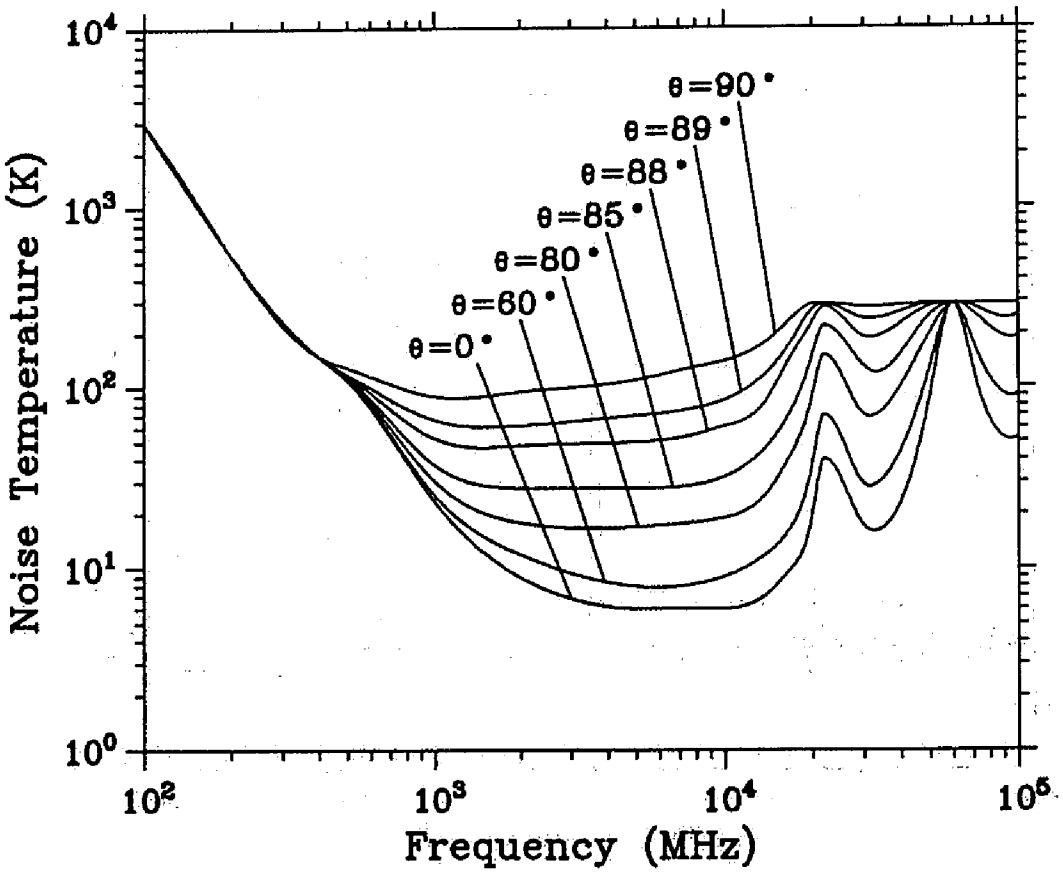

Figure 2.19: Sky noise temperature versus frequency [*Skolnik*, 1980]. Solid curves are for various zenith angle θ of the antenna beam direction for geometric-mean galactic temperature, sun noise ten times quiet level, sun in unity-gain side lobe, cool temperate-zone troposphere, and 2.7 K cosmic black body radiation.

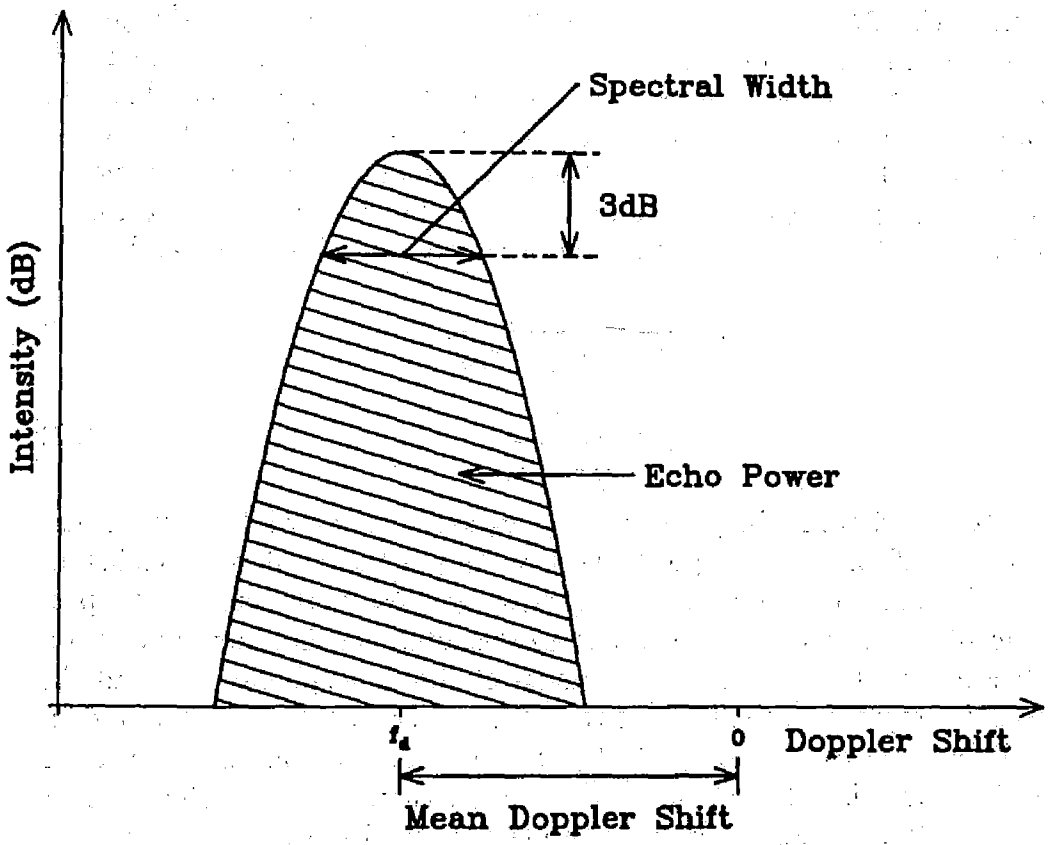

Figure 2.20: Spectral parameters of the atmospheric echo.

These spectral parameters are estimated by the non-linear least squares fitting method because $g(f)$ is a non-linear function.

The principle of the least squares fitting method is to determine the parameters with which the square sum of errors between the model function and the observed data becomes minimum. The initial value of the fitting is determined by the following procedure. The initial value of P_r is set as the maximum value of the smoothed echo power spectrum. The initial value of f_d is set as the frequency corresponding to the initial P_r. The initial value of σ is 2 m s^{-1} which is determined in experience. The Doppler spectrum of the received signals includes the ground clutter and the white noise in addition to the atmospheric scattering signal. We do not use the zero Doppler component of the spectrum in order to exclude the ground clutter. We consider that the noise power density (noise level) varies in time and in beam directions, but not in heights. Before the spectral parameters are estimated, we subtract the noise level from the observed power spectrum.

The reliability of the estimated spectral parameters can be evaluated by

$$D_1 = \frac{P_r}{\sigma_n} = \frac{P_r}{P_n/\sqrt{N_{icoh}}} \tag{2.6}$$

$$D_2 = \frac{P_r}{\sqrt{V/N_{fit}}} \tag{2.7}$$

where P_r is the maximum echo power density, σ_n is the standard deviation of the noise fluctuation, P_n is the noise power density, N_{icoh} is the number of incoherent integrations, V is square sum of the fitting error, and N_{fit} is the number of spectral components used in the fitting. D_1 is a parameter that is generally called a signal detectability. If received signal consists of the atmospheric echo and the white noise, D_1 represents the ratio of the echo power to the noise fluctuation, and the reliability of estimated spectral parameters can be found. However, if the fitting is wrong, i.e. the estimated P_r is larger than the true value, and/or the noise fluctuation estimated from a noise level is smaller than true value due to interference signal, D_1 is different from the reliability of spectral parameters. Therefore, we also use D_2 that directly represents the quality of the fitting operation, and use the estimated spectral parameters when both of D_1 and D_2 are more than 3.

The radial component of the wind velocity v_r is proportional to the mean Doppler shift. For the BLR, the mean Doppler shift of 1 Hz corresponds to the wind velocity of about 0.11 m s^{-1}. We need more than three beam directions to estimate three components of the wind velocity. One beam should be directed to the zenith and estimates the vertical wind because the vertical wind velocity is usually much weaker than the horizontal wind velocity. Other two beams are

tilted from the zenith with the angle of 15°. If the wind velocity is uniform over the radar, the horizontal component of the wind velocity along the beam direction v_h is given by

$$v_h = \frac{v_r - v_z \cos 15°}{\sin 15°} \tag{2.8}$$

where v_z is the vertical velocity.

Chapter 3

System performance of the BLR

The BLR system (see Figure 3.1) was first installed at the MU Observatory in Shigaraki, Japan (34.85°N, 136.10°E, 385 m above sea level) on 9 December 1991. The location of the BLR was surrounded by relatively low mountains. It gets sometimes colder than 0°C even in the daytime in winter.

In this chapter, we show the results of simultaneous observations of the BLR and the MU radar, and discuss the performance of the BLR in comparison with the observation results with the MU radar in Section 3.1. The feature of diurnal variations of the PBL is described from the continuous four-month observations during May–August 1992 in Section 3.2.

3.1 Simultaneous observations of the BLR and the MU radar

We conducted the first simultaneous observations of the BLR and the MU radar on 6 January 1992. The observation parameters of the BLR and the MU radar are shown in Tables 3.1 and 3.2, respectively. The range and time resolutions were 150 m and 1 min, respectively, which were approximately the same for both radars. For vertical, northward, and eastward beams, we chose the same beam directions with the MU radar. The sampling interval of the BLR was 0.67 μs corresponding to the range of 100 m.

Figure 3.2 shows the Doppler spectra observed with the BLR. Throughout this thesis a height from the ground is used. During the observations, the rainfall of 1.1 mm hour^{-1} was observed on the ground in average. The echo scattered by the precipitation appeared up to the height higher than 5 km. Because echo intensity in the height range lower than about 2 km was very strong, the Doppler spectra were distorted by the limited data length and the frequency aliasing.

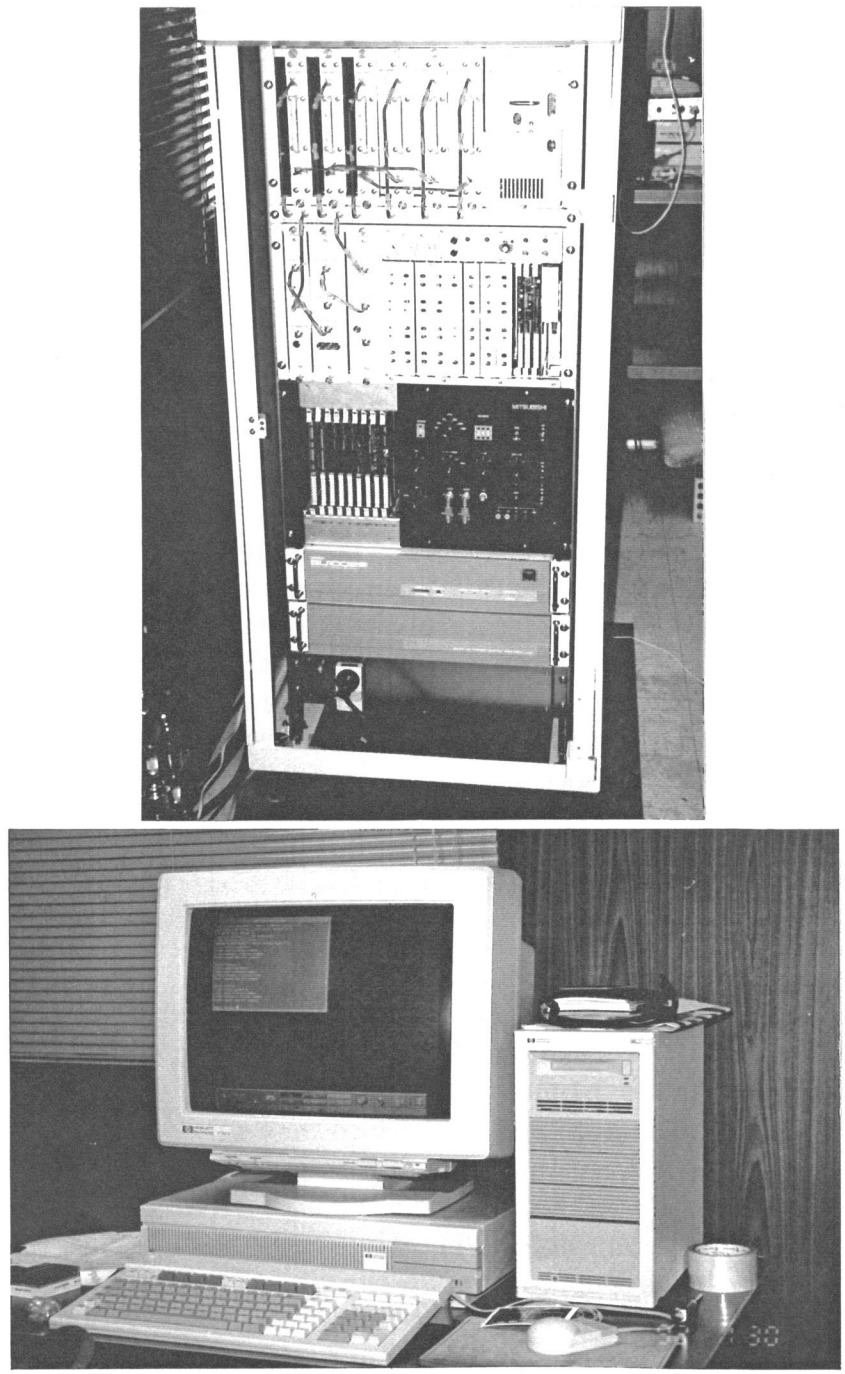

Figure 3.1: The transmitter-receiver and data acquisition units (upper panel) and the signal processing unit (lower panel) of the BLR. View of the BLR is shown in the first page of this thesis.

Table 3.1: Observation parameters of the BLR used on 6 January 1992.

Parameter	Value
Pulselength:	1 μs
IPP:	100 μs
Beam direction (Azimuth, Zenith):	(0, 0), (0, 15°), (90°, 15°)
Number of coherent integrations:	32
Number of incoherent integrations:	32
FFT points:	128
Range resolution:	150 m
Sampling interval:	0.67 μs (100 m)
Time resolution:	$\sim$ 1 min
Maximum observable horizontal wind velocity:	67.1 m s^{-1}
Resolution of horizontal wind velocity:	1.0 m s^{-1}

Table 3.2: Observation parameters of the MU radar used on 6 January 1992.

Parameter	Value
Pulselength:	1 μs
IPP:	400 μs
Beam direction (Azimuth, Zenith):	(0, 0), (0, 15°), (90°, 15°), (180°, 15°), (270°, 15°)
Number of coherent integrations:	38
Number of incoherent integrations:	5
FFT points:	128
Range resolution:	150 m
Sampling interval:	1 μs (150 m)
Time resolution:	$\sim$ 1 min
Maximum observable horizontal wind velocity:	82.0 m s^{-1}
Resolution of horizontal wind velocity:	1.3 m s^{-1}

This results in the higher noise floor of the Doppler spectra than that in other altitudes. In first three ranges, because of the very intense ground clutter echo, we can recognize the Doppler width of the clutter. Moreover, because either I or Q channel of the receiver was saturated, the image of the echoes appeared at the negative Doppler components which were symmetrical to the real ones with the zero Doppler shift. The noise level was constant in the height range higher than 2 km, which showed that the noise generated by the receiver did not fluctuate.

Figure 3.3 shows the contour plots of the Doppler spectra. The Doppler shift of the echo in the vertical beam (left panel) was downward in all height range. The downward velocity rapidly increased in the height below 1.5 km, where the echoes were probably scattered by the precipitation. The echoes above 1.5 km constantly shows small but downward Doppler shift. We consider that they are scattered by the descending crystal of ice and/or snow.

Figure 3.4 shows the height profile of the volume reflectivity η and the radar reflectivity index Z, converted according to

$$Z = \frac{\lambda^4}{284}\eta \tag{3.1}$$

of the BLR. Since η and Z were maximum at 1.0–1.5 km heights, it is considered that there existed the bright band in these heights. It is known in experience that the relationship between the radar reflective index Z and the rainfall rate R is expressed by [*Kodaira et al.*, 1980]

$$Z = BR^{\beta} \tag{3.2}$$

where B and β are the constants owing to the condition of the rainfall. It is known that $B = 200$ and $\beta = 1.6$ show good approximation in many cases [*Battan*, 1973]. The rainfall rate on the ground was $R = 1.1$ mm hour^{-1}, then the radar reflective index was $Z = 233$ mm^6 m^{-3} by using the above constants. Considering the uncertainty of B and β, we infer that this result is reasonable compared with Figure 3.4.

Figure 3.5 shows the height profile of the volume reflectivity η and the refractivity turbulence structure constant C_n^2, converted according to

$$C_n^2 = \frac{\lambda^{1/3}}{0.38}\eta \tag{3.3}$$

of the MU radar. Although fluctuations of C_n^2 were much larger than those of Z in Figure 3.4, C_n^2 was approximately 10^{-15} m$^{-2/3}$ in the height range above 1 km. Converting this C_n^2 to η for the frequency of 1357.5 MHz, $\eta = 6.3 \times 10^{-16}$ m^{-1}. The echo intensity by the atmospheric turbulence was 60–70 dB weaker

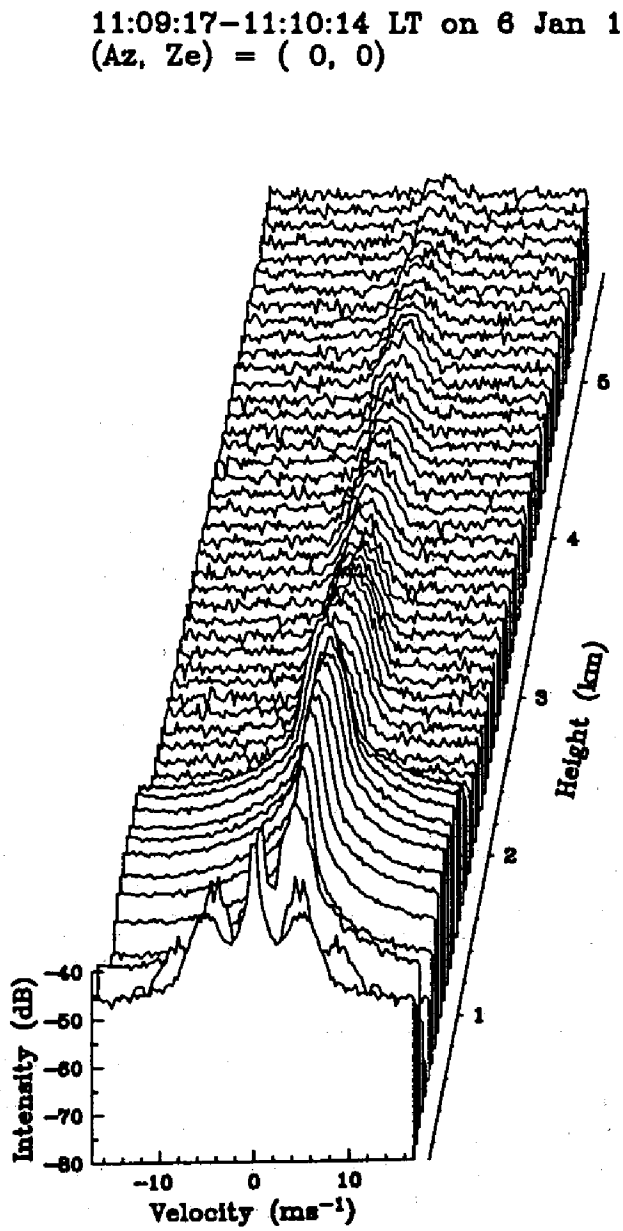

Figure 3.2: Doppler spectra observed with the BLR on 6 January 1992 for the vertical beam. The positive Doppler shift indicates the direction toward the radar. The zero Doppler component is interpolated by using two components next to it.

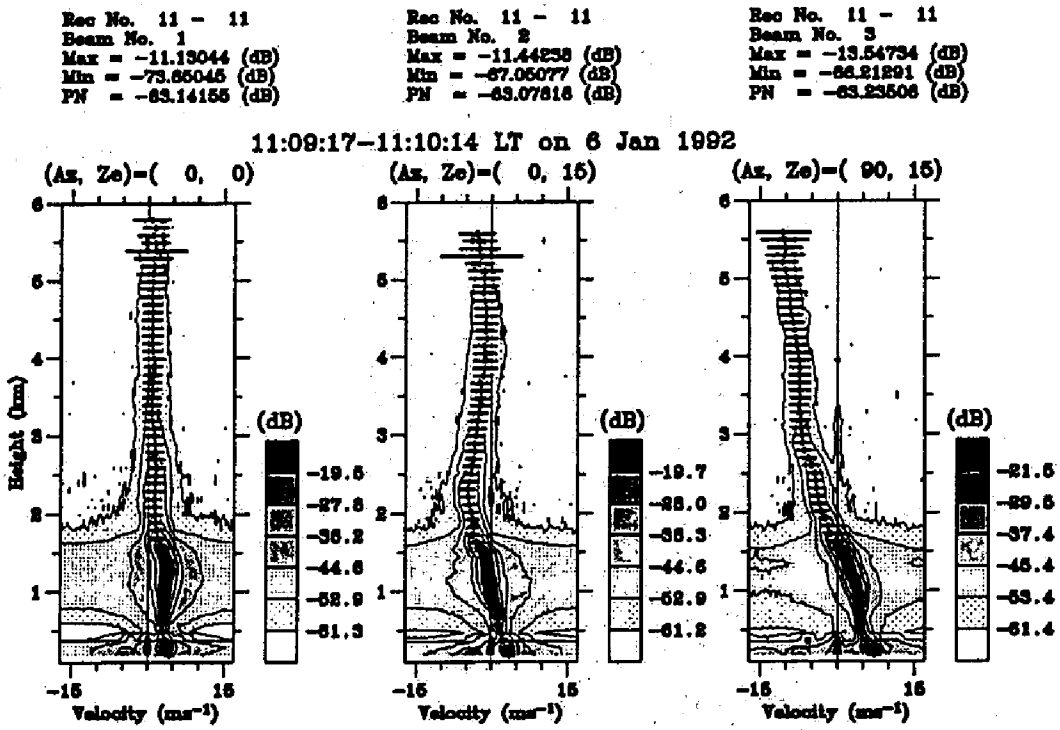

Figure 3.3: Contour plots of the Doppler spectra observed with the BLR on 6 January 1992. Left, center, and right panels indicate vertical, northward, and eastward components, respectively. The positive Doppler shift indicates the direction toward the radar. The zero Doppler component is interpolated by using two components next to it. Vertical and lateral bars indicate the estimated mean Doppler shift and spectral width, respectively.

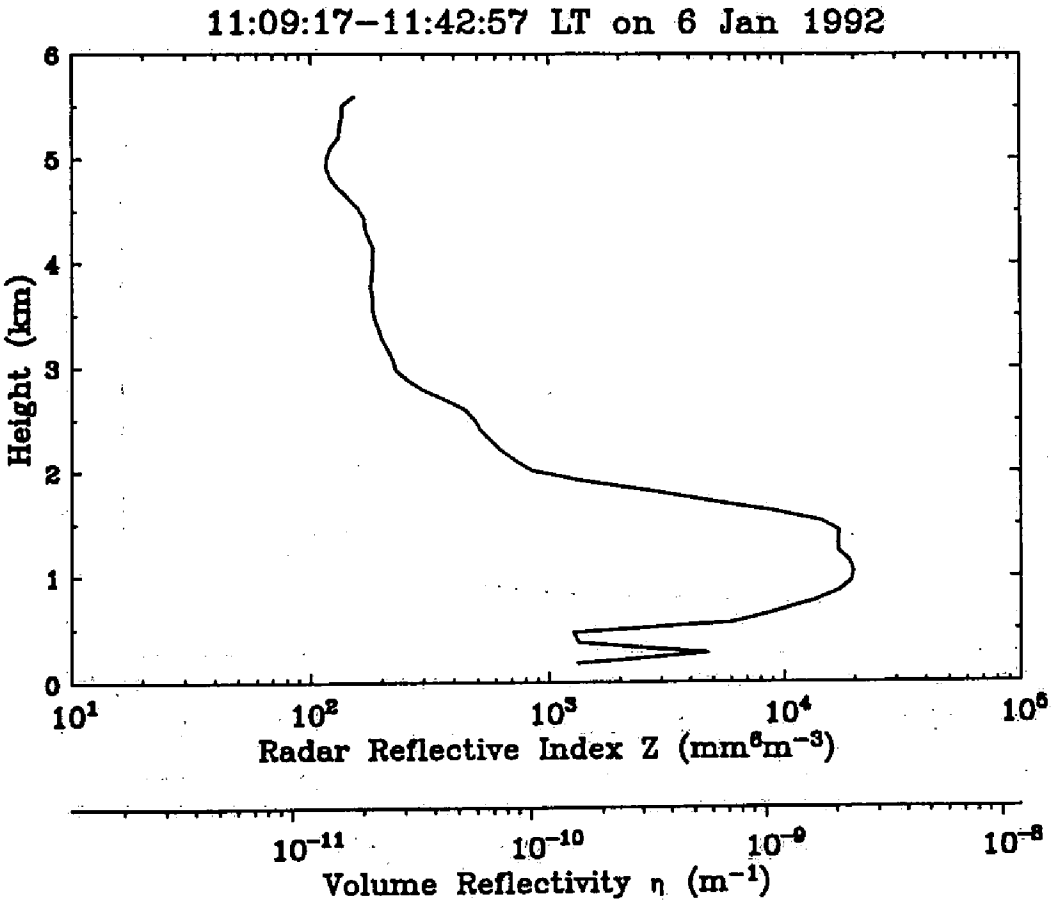

Figure 3.4: Height profile of the volume reflectivity η and the radar reflective index Z observed with the BLR on 6 January 1992.

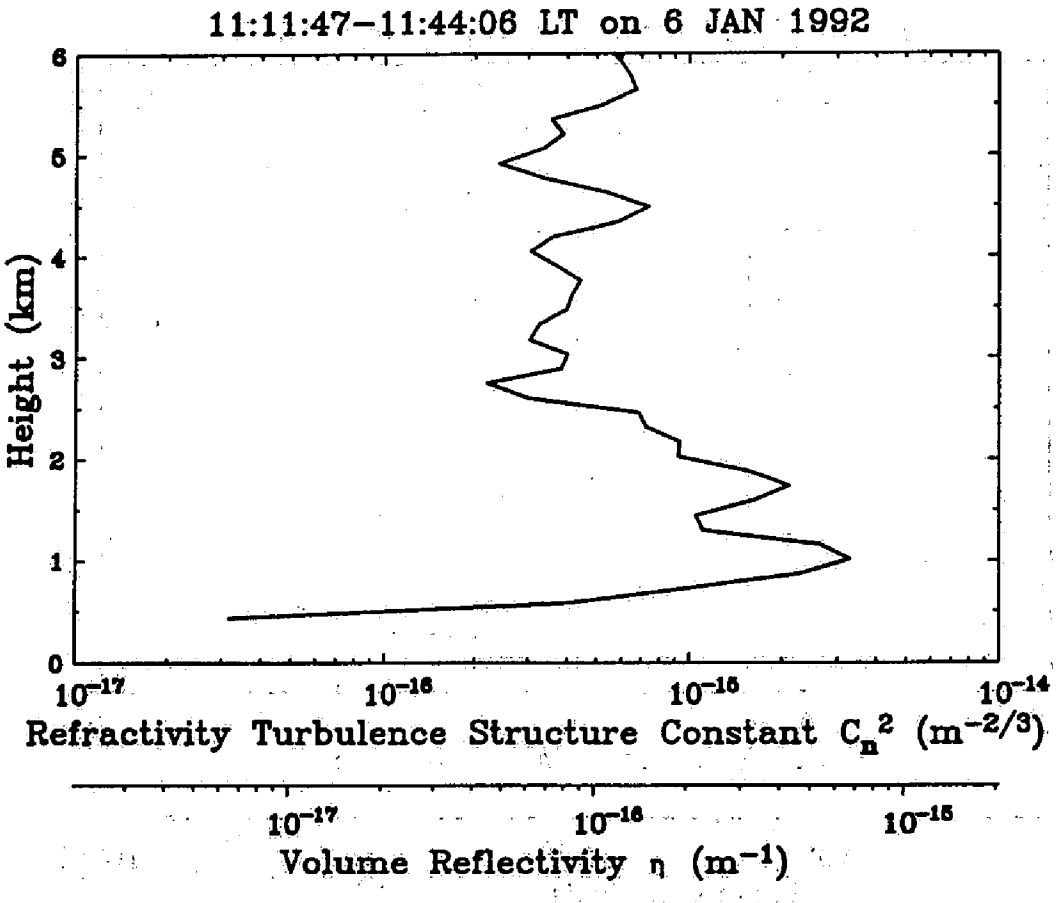

Figure 3.5: Height profile of the volume reflectivity η and the refractivity turbulence structure constant C_n^2 observed with the MU radar on 6 January 1992.

compared with the precipitation echo obtained by the BLR. When we refer to Figure 2.1, the intensity difference is reasonable.

Solid and dashed lines in Figure 3.6 show the height profiles of the wind velocity observed with the BLR and the MU radar, respectively. These are wind profiles averaged over 30 min. The BLR could obtain the wind velocities in the height range of 0.2–5 km. It is known from the observation with the MU radar that the horizontal motion of the precipitation is identical with the atmospheric motion [*Fukao et al.*, 1985c; *Wakasugi et al.*, 1986, 1987]. Because the system delay of the BLR was still uncertain in this observations, there were some discrepancy in the height between the both horizontal wind velocities. However, the horizontal wind velocity observed with the BLR showed an almost identical profile compared with that observed with the MU radar.

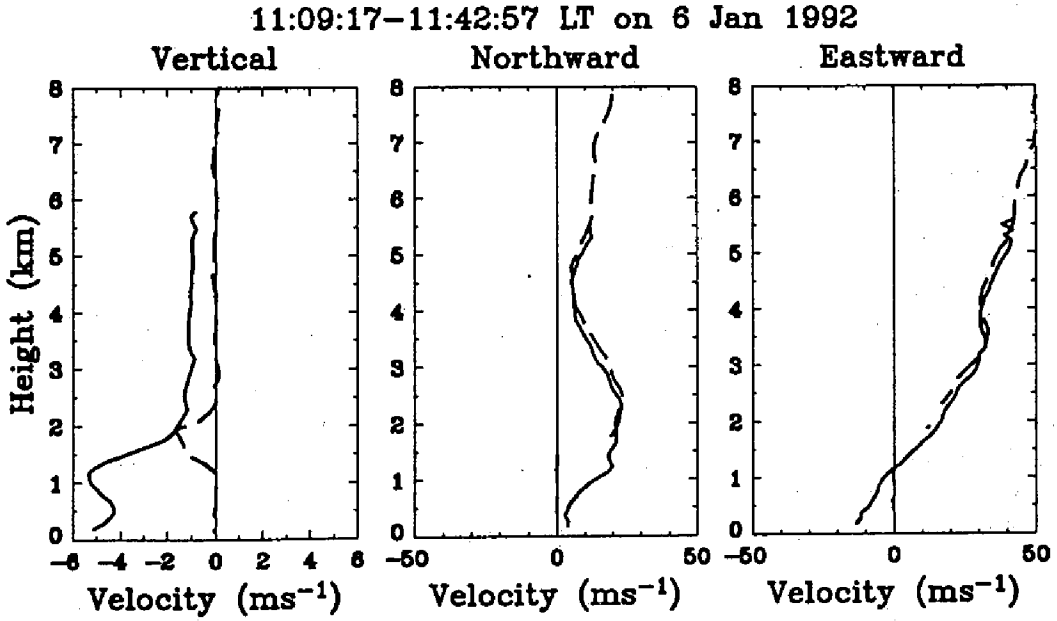

Figure 3.6: Height profiles of wind velocities averaged over 30 min observed with the BLR (solid line) and the MU radar (dashed line) on 6 January 1992. Left, center, and right panels indicate vertical, northward, and eastward components, respectively.

We compared the standard deviation of the wind velocity between the BLR and the MU radar as shown in Figure 3.7. The standard deviation of the wind velocity estimated from the Doppler spectra includes the real fluctuations of the wind velocity and the fluctuations owing to the estimation error. In the vertical

component (left panel), because the vertical motion of the precipitation detected by the BLR was different from that of the atmosphere detected by the MU radar, there were relatively large discrepancy between each other. However, the standard deviation of zonal and meridional wind velocity was almost identical with each other.

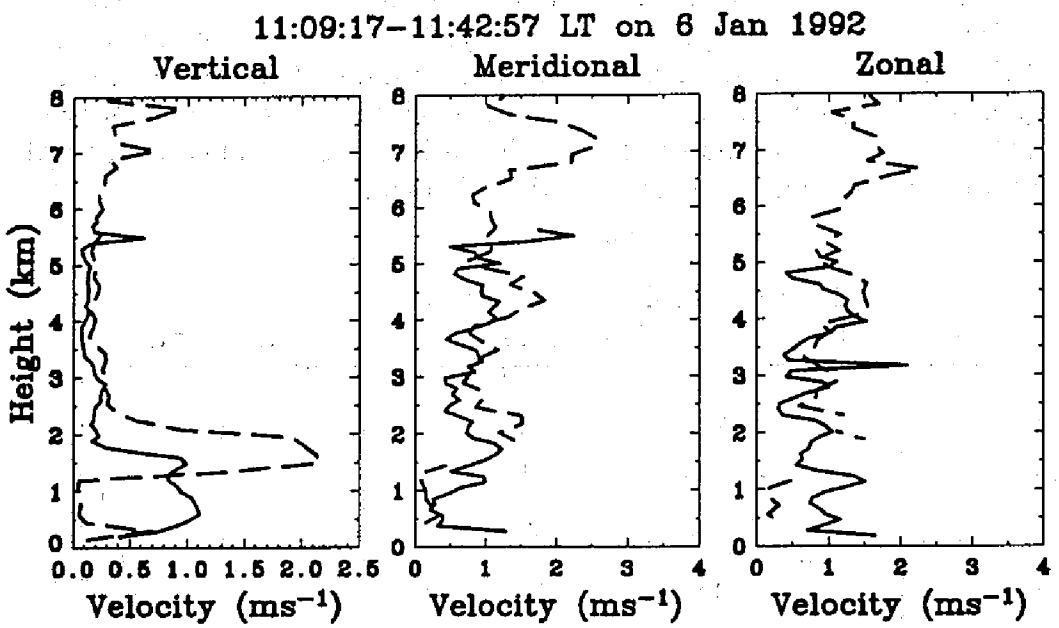

Figure 3.7: Height profiles of the standard deviation of the wind velocities for 30 min observed with the BLR (solid line) and the MU radar (dashed line) on 6 January 1992. Left, center, and right panels indicate vertical, meridional, and zonal components, respectively.

The estimation error of the wind velocity has been studied by *Yamamoto et al.* [1988]. According to their result, it is found that the estimation errors of the line-of-sight velocity and the horizontal velocity are 0.16 m s^{-1} and 0.43 m s^{-1} for the MU radar, 0.064 m s^{-1} and 0.35 m s^{-1} for the BLR, respectively. The horizontal velocity was estimated by using the line-of-sight velocities obtained from vertical and two oblique beams in the case of the BLR (see Chapter 2) and from four oblique beams without using a vertical beam in the case of the MU radar. However, the estimation error of the horizontal wind is almost the same with each other, and is within the floor of the fluctuation of the horizontal velocity. The fluctuations over estimation errors seem to show spatial and time fluctuations of the wind velocity field.

3.2 Continuous observations in Japan

We conducted continuous observations with the BLR for about four months during May–August 1992 at the MU observatory in Shigaraki, Japan. In the routine observations with the BLR, the echoes from each of 64 observed heights (0.1–6.4 km) are integrated coherently for 3.2 ms to form each sampled value and a 128-point time series of these values is stored. A 128-point (0.4 s average) Doppler spectrum is then calculated for each height by using FFT. Beam direction is instantly changed after taking the Doppler spectrum. Finally 32 Doppler spectra are averaged for each height. We can obtain height profiles for 3 directions in about 50 s, including the data transfer time ($\sim$ 10 s) to the computer.

3.2.1 Diurnal variation of echo intensity

Figure 3.8 shows the time-height cross section of the BLR echo intensity (averaged every 30 min) during 1–30 June 1992. Throughout this thesis all echo intensity plots are corrected by the square of range. In general the *L*-band BLR echoes are coming from the clear atmosphere (Bragg scattering and Fresnel reflection) and/or precipitation particles [see, e.g., reviews by *Gage*, 1990, and *Röttger and Larsen*, 1990]. Very intense echoes covering the whole height range (such as on June 7, 11, 15, 17, 19, 23, 27, and 30) suggest enhancement due to raindrops. We find that strong atmospheric echoes appear in general in the daytime.

The echo intensity obtained by atmospheric radar is usually determined by non-uniformity of the atmospheric refractivity. The vertical gradient of potential refractive index M in the neutral atmosphere is given by [*Ottersten*, 1969a, b; *Gage et al.*, 1985]

$$M = -\frac{77.6 \times 10^{-6} p}{T}\left(\frac{N^2}{g} + \frac{15600q}{T}\frac{N^2}{g} + \frac{7800}{T}\frac{dq}{dz}\right) \tag{3.4}$$

where p is the atmospheric pressure in hPa, T is the absolute temperature, N is the Brunt-Väisälä frequency in s^{-1}, g is the acceleration of gravity in m s^{-2}, q is the specific humidity in g kg^{-1}, and z is the altitude in meters. In the lower atmosphere, the third term due to the humidity gradient is dominant. In the case of the BLR operating at the frequency of *L*-band, it is known that the echo intensity is proportional to $N^{-2}M^2$ [*Gage*, 1990]. Since N is proportional to the square root of the vertical gradient of (potential) temperature, the echo intensity must be determined mainly by the vertical gradients of humidity and temperature. In the PBL atmospheric conditions are vertically almost uniform since the atmosphere is well mixed by convection and/or turbulence. Therefore,

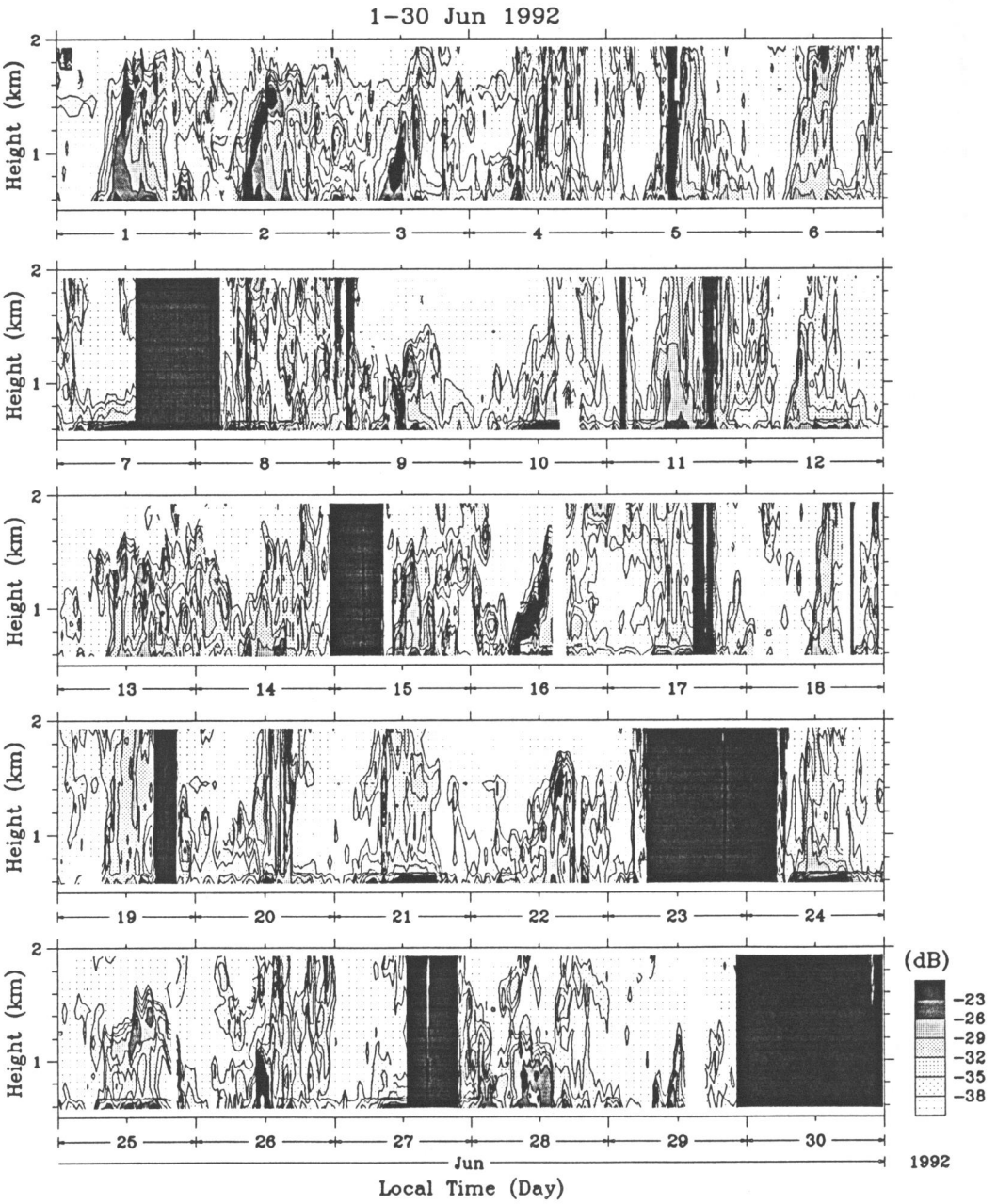

Figure 3.8: Time-height cross section of the BLR echo intensity averaged every 30 min for the eastward beam (azimuth=90°, zenith=15°) during June 1992.

the echo intensity becomes very strong at the boundary between the PBL and the free atmosphere, at which both the temperature and humidity gradients become quite significant.

In order to confirm the relationship between echo intensity and the temperature/humidity gradient considered above, we have carried out radiosonde experiments at the radar site every six hours on 25 June 1992. As shown in Figure 3.9, the echo intensity took a clear maximum just at the level above which the virtual potential temperature gradient becomes large, both in the morning ($\sim$ 0825 LT) and in the afternoon ($\sim$ 1433 LT). We detected that the height of the maximum echo intensity corresponds to the top of the PBL (or the mixing layer). Such a relationship was not found in the night-time ($\sim$ 02 LT and $\sim$ 20 LT, not shown) when the PBL itself must be smeared and suppressed. Similar observations to detect the top of a lower (surface) boundary layer have been done by many other types of radars (see, e.g., a review by Gossard, 1990, and references therein), and those to detect the frontal surface and/or tropopause have also been accumulated by similar types of wind-profiling (UHF/VHF) radars [e.g., *Gage and Green*, 1978; *Röttger*, 1979; *Larsen and Röttger*, 1983; *Fukao et al.*, 1989; *Larsen et al.*, 1991]. As shown in Figure 3.8, in the period from 1 June through 3 June 1992, we find out striking diurnal variations of strong echoes as mentioned above. We have detected from both radar and meteorological observations that the weather was fine throughout those three days. Figure 3.10 shows a magnified time-height cross section of the echo intensity (averaged every 10 min) during the three days. A thin enhanced echo layer appears at about 500 m height in the morning ($\sim$ 08 LT) every day and ascends up to about 1500 m height in the afternoon ($\sim$ 14 LT). After 14 LT the enhanced echo layer gradually disappears. We understand that such a thin enhanced echo layer corresponds to the top of the PBL. By using the BLR, we can vividly observe the diurnal variations of the PBL in clear days. It must be noted that the variation of echo intensity is not discussed in the earlier similar study by *May and Wilczak* [1993].

As shown in Figure 3.8, such remarkable diurnal PBL variations as observed during 1–3 June are not always observed every clear day. In the whole observational period of about four months in Shigaraki, they were limited to a few days each month. It should be noted, however, that such a remarkable diurnal variation has a tendency that once it appears continues for two or three days. These features will be again discussed in Subsection 3.2.4, in relation to conditions to generate diurnal variations of the PBL.

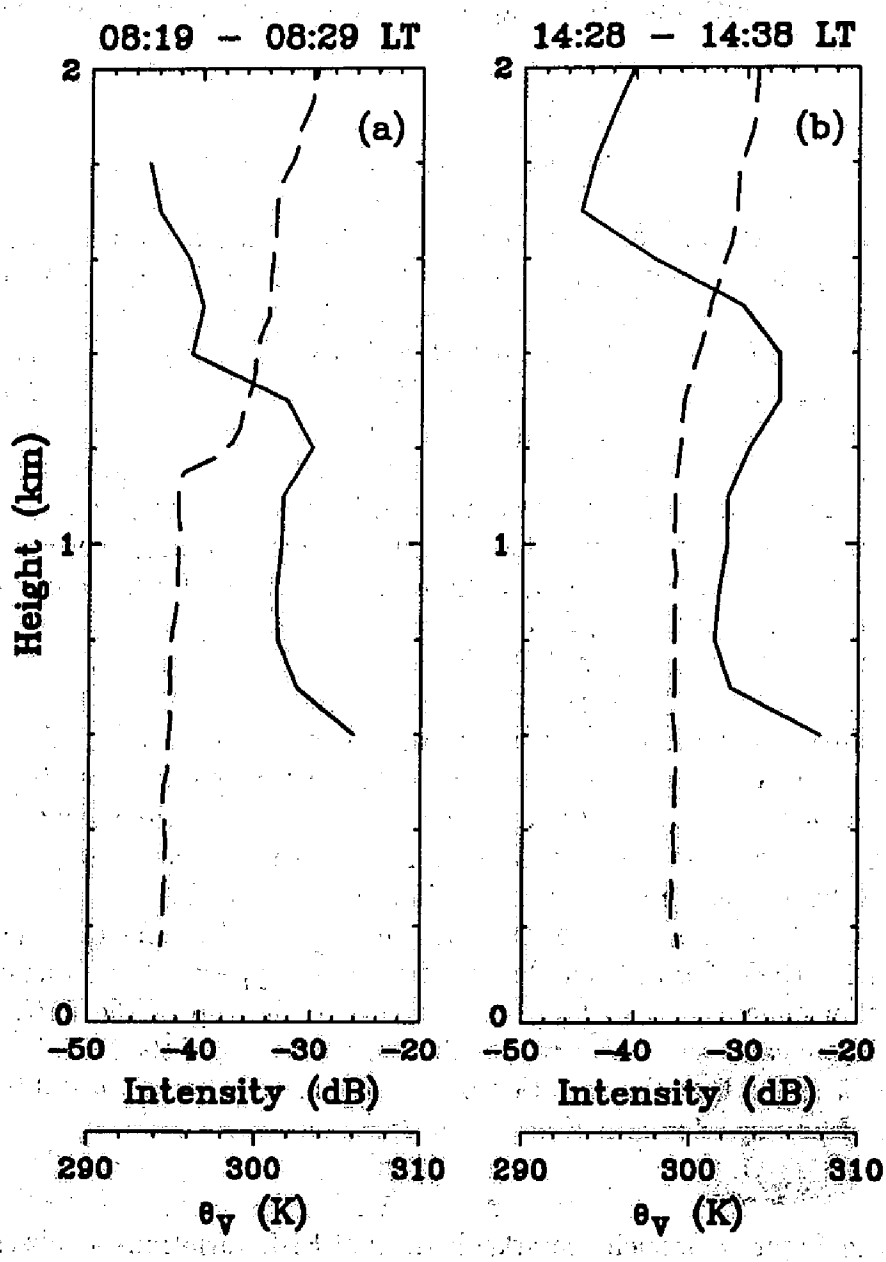

Figure 3.9: Profiles of virtual potential temperature obtained by radiosonde observations (dashed curves) and echo intensity of the BLR averaged over 10 min (solid curves). The BLR and the radiosonde simultaneously obtained the data at (a) ~0825 LT and (b) ~1433 LT on 25 June 1992.

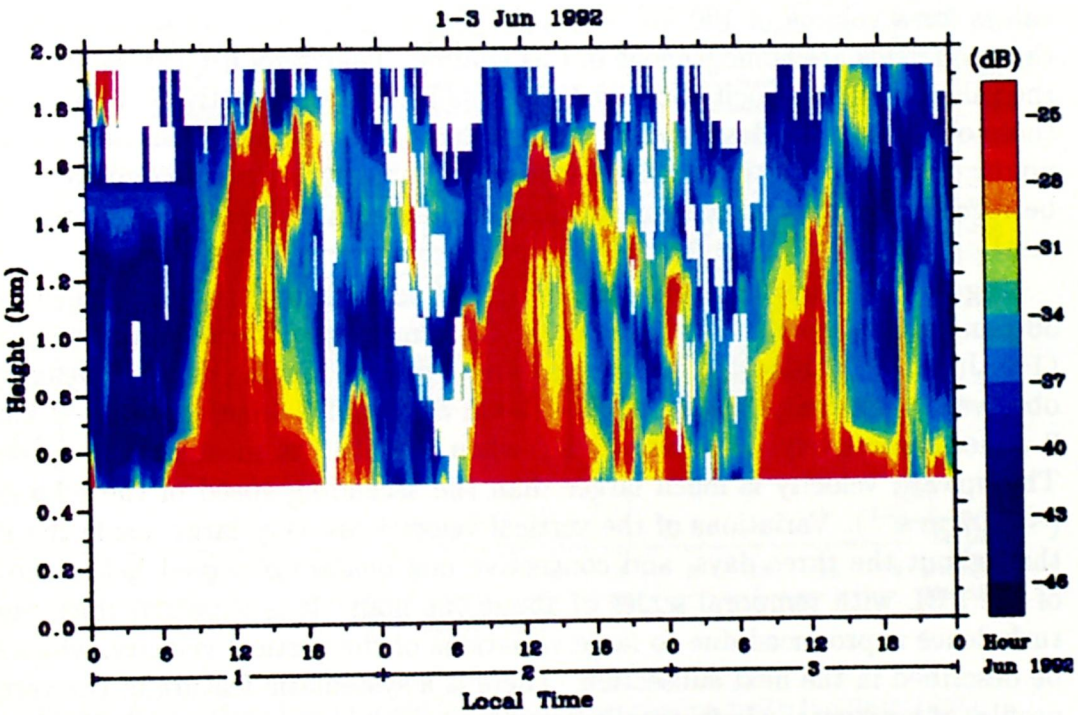

Figure 3.10: Time-height cross section of the echo intensity averaged every 10 min on clear days during 1–3 June 1992.

3.2.2 Variations of atmospheric motion

The BLR detects the radial Doppler velocity associated with atmospheric eddies with the Bragg length scale (given by half the radar wavelength ≈ 0.22 m) inside a sampling volume (given by the beam width $\approx 7.6°$ for one beam and the vertical resolution ≈ 100 m) under the Taylor's frozen turbulence hypothesis. The vertical velocity determined by using one vertical beam corresponds to the mean value for a volume of 100 [m] $\times \pi(z \tan 3.8°)^2$ [m^2], where z is the height in meters. Since the zonal and meridional velocities are determined by using vertical and 15°-oblique beams, these velocity components obtained by the BLR are the mean values for a volume of 100 [m] $\times \pi(z \tan 18.8°)^2$ [m^2] under an assumption that the wind fields are homogeneous in this volume. Therefore, it must be noted that the values of wind velocity observed with the BLR are qualitatively different from those obtained with classical anemometer and balloon observations at a localized point. On the other hand, these estimated values of velocity components can be regarded as instantaneous values in time taken at the sampling interval (≈ 1 min).

Figure 3.11 shows the meridional-vertical wind distribution (averaged every 30 min) observed with the BLR during the remarkable diurnal variation period (1–3 June 1992) reported in the previous section. Strong upward velocity is observed in the height range of 0.6–1.1 km on 1 and 3 June, and of 1–2 km on 2 June, respectively, at about 08 LT when the PBL is most rapidly growing. The upward velocity is much larger than the ascending speed of the echo layer (~ 0.07 m s^{-1}). Variations of the vertical velocity are very large inside the PBL throughout the three days, and convective motions are observed below the top of the PBL with temporal scales of about one hour. It is expected that intense turbulence is produced due to large variations of the vertical velocity, which will be described in the next subsection. There is a systematic feature in the vertical profiles of horizontal winds, that is an upward clockwise rotation of the horizontal wind vector as shown in Figure 3.12. This feature is consistent with that known as the Ekman's spiral hodograph in the PBL (see Section 1.2).

Figures 3.13 (a) and (b) show diurnal variations of zonal-vertical and zonal-meridional wind averaged for the three days during 1–3 June. Mountain-valley breeze circulation is not so clear, but we find that southward winds are predominant in the height range higher than 1 km almost throughout the three days. In almost all the cases when the remarkable diurnal variation of the enhanced echo layer is observed during May–August, the southward wind component dominants in the free atmosphere. Indeed on 4 June when dominant wind became northward, the diurnal variation was not very obvious in spite of the clear day as shown in Figure 3.14. Figure 3.15 shows the monthly-mean diurnal varia-

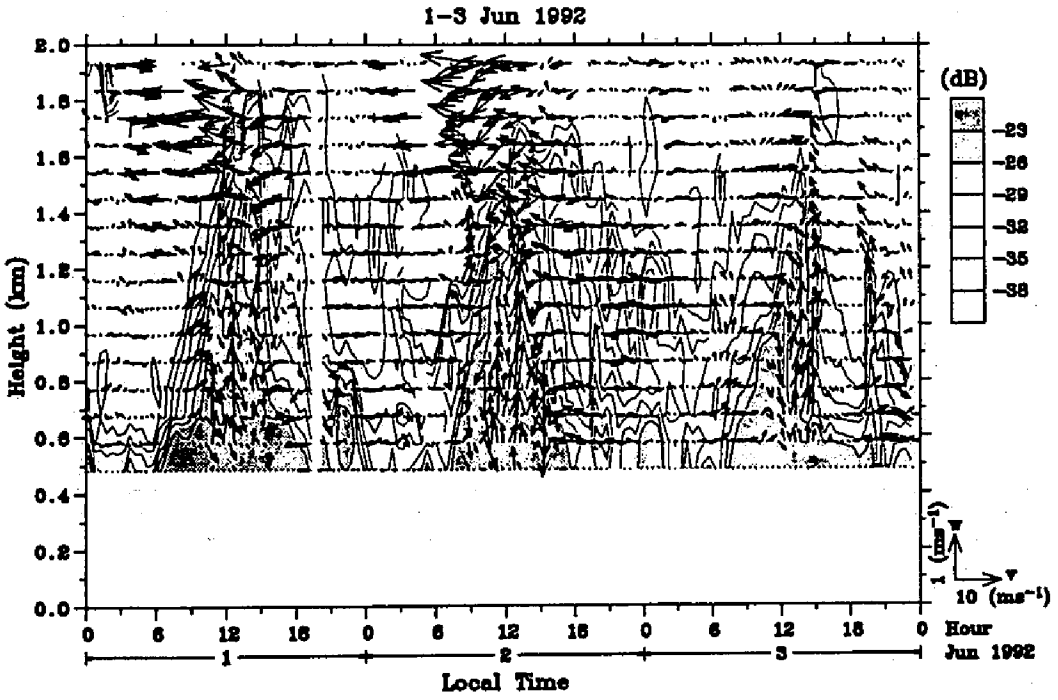

Figure 3.11: Time-height cross section of the echo intensity (contour plot), and meridional and vertical wind velocity (vector plot) observed during 1–3 June 1992. Vectors are directed upward for an upward component, and towards the right for a northward component. Both of intensity and winds are averaged every 30 min.

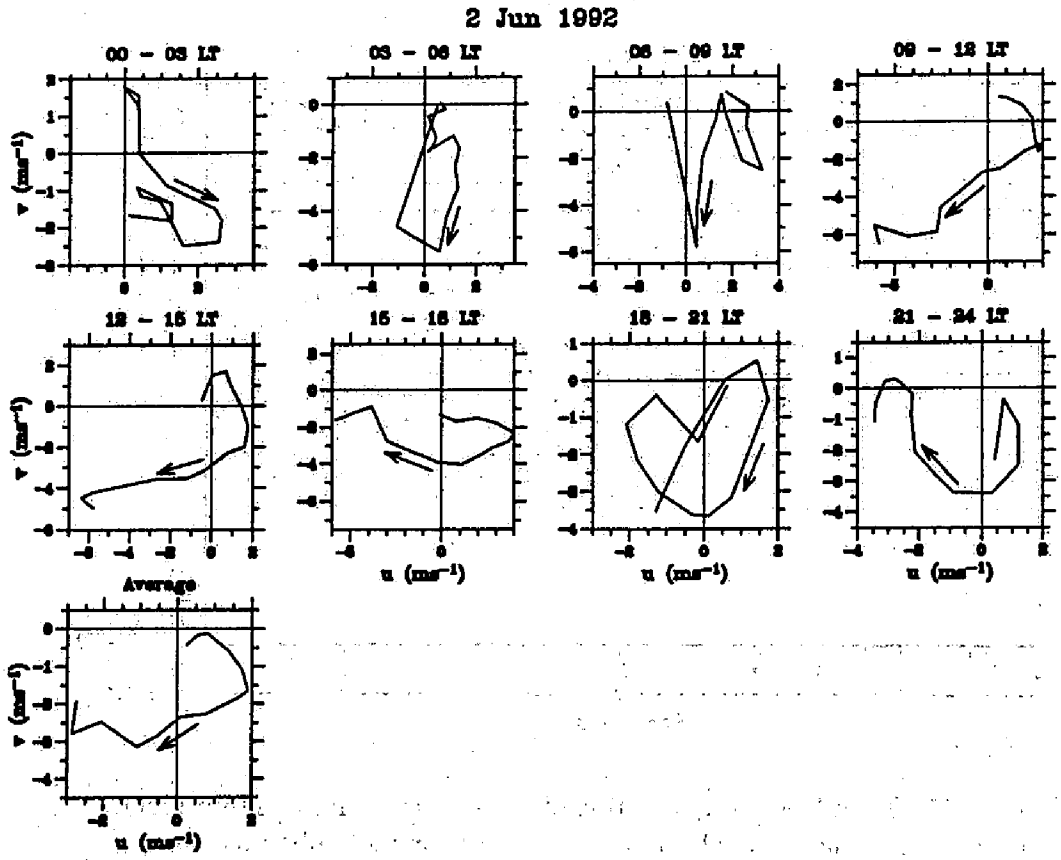

Figure 3.12: Vertical hodographs of horizontal wind vectors (averaged every three hours) in the height range of 0.5–2.0 km observed with the BLR on 2 June 1992.

tion of horizontal winds in the PBL. We confirm again that a mountain-valley breeze-like circulation is not clear, and that horizontal wind vectors are almost always rotating clockwise with height as predicted in the classical Ekman theory. These features are somewhat different from the earlier results by *May and Wilczak* [1993] at Denver, U.S. which include a downslope circulation and a diurnal wind oscillation.

3.2.3 Turbulence activities inside the PBL

The echo intensity discussed in Subsection 3.2.1 is a result of turbulence activity and morphology through Bragg scattering and Fresnel reflection. However, a quantitative discussion for turbulence parameters based on the echo intensity is in general not so easy because the refractivity is strongly dependent on the temperature and humidity fields as formulated in (3.4). Instead, we can estimate turbulence parameters from the spectral width of the Doppler frequency spectrum of radar echoes, which corresponds to the statistical velocity variations of eddies with the scale of the Bragg length. For example, the kinetic energy dissipation rate ε and the (vertical) eddy diffusivity K are calculated by using the following approximate equations [*Hocking*, 1985; *Fukao et al.*, 1994; *Yamanaka et al.*, 1994; *Kurosaki et al.*, 1995]:

$$\varepsilon \approx 0.3N(\sigma^2_{\frac{1}{2}\mathrm{obs}} - \sigma^2_{\frac{1}{2}\mathrm{beam}}) \tag{3.5}$$

and

$$K \approx 0.1\frac{\sigma_{\frac{1}{2}\mathrm{obs}}{}^2 - \sigma_{\frac{1}{2}\mathrm{beam}}{}^2}{N} \tag{3.6}$$

where $\sigma_{\frac{1}{2}\mathrm{obs}}$ is the half-power half-width of a Doppler velocity spectrum, and

$$\sigma_{\frac{1}{2}\mathrm{beam}} = \delta_{\frac{1}{2}}|\overline{u}_h| \tag{3.7}$$

represents beam broadening due to the background horizontal wind $\overline{u}_h$ for the half-power half-width $\delta_{\frac{1}{2}}$ of the effective (two-way) radar beam (2.7° for the BLR).

Figure 3.16 shows the time-height cross section of K calculated under an assumption that N is a constant ($= 1.7 \times 10^{-3}$ s^{-1}). The eddy diffusivity K is enhanced every morning at about 08 LT when upward velocity is strong. Turbulence is intense inside the PBL where BLR echoes are not the strongest. If we consider that N may be smaller inside the PBL (where the potential temperature gradient becomes in general very small) than the assumed value, K might be much larger than the values shown in Figure 3.16. Based on these considerations, we confirm that the strong echo intensity at the top of the PBL discussed in Subsection 3.2.1 is induced mainly by the stable temperature/humidity gradient

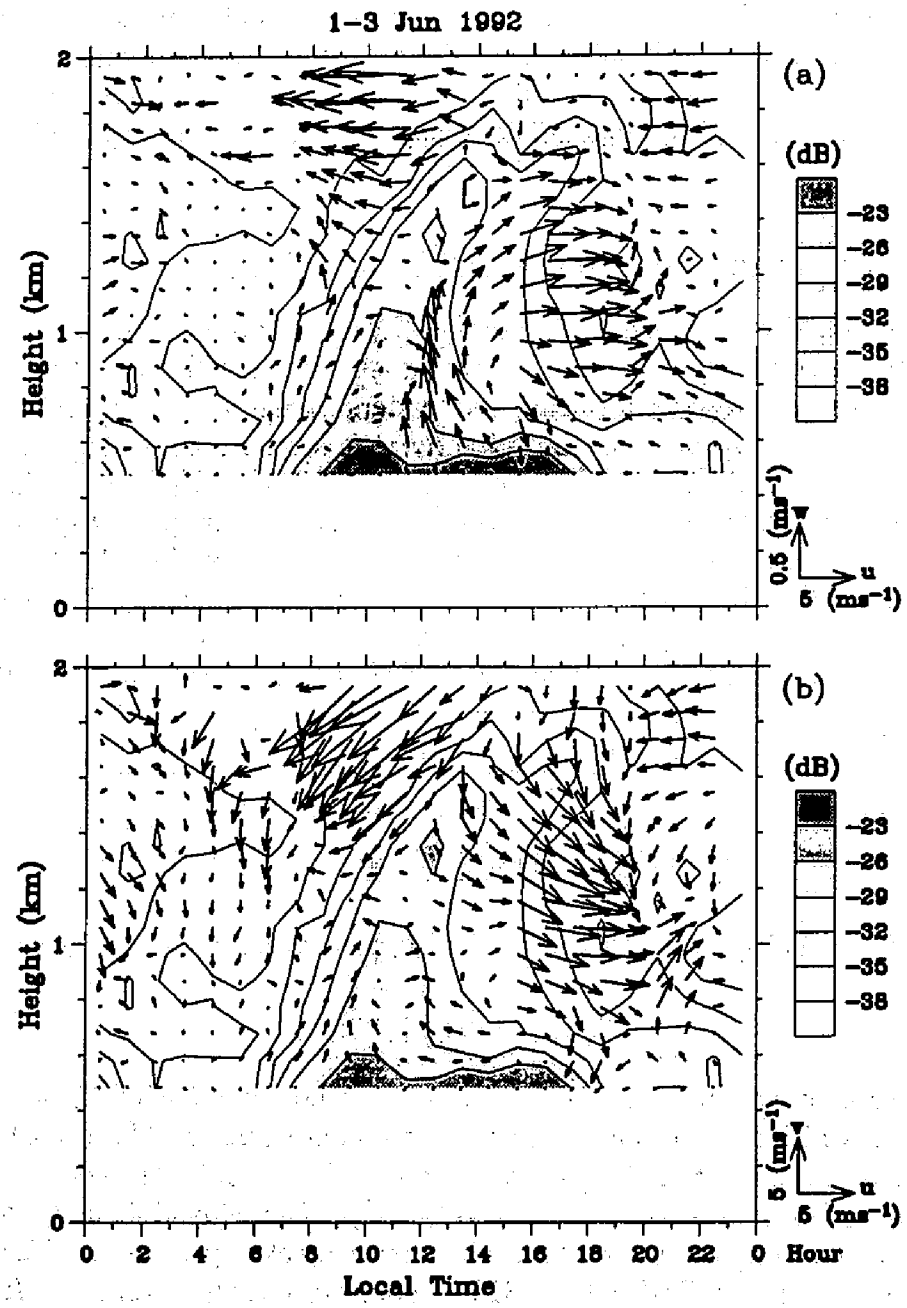

Figure 3.13: Daily variation of (a) zonal-vertical and (b) zonal-meridional winds (vector plot), and echo intensity (contour plot) averaged for three days during 1-3 June 1992. Vectors are directed upward for (a) an upward component and (b) a northward component, and towards the right for a eastward component.

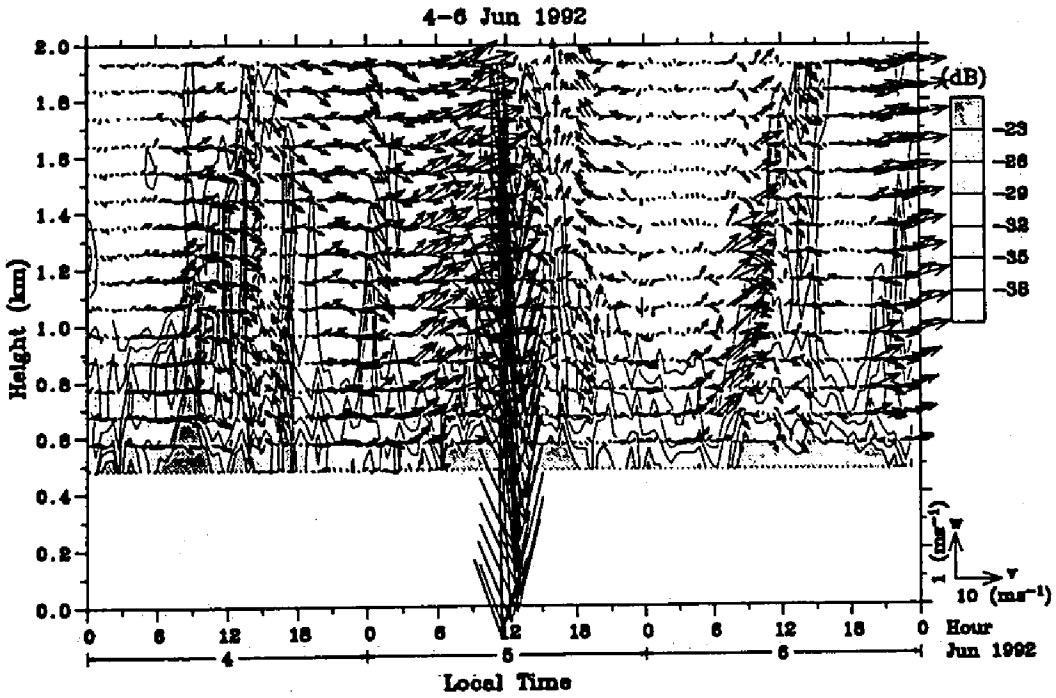

Figure 3.14: The same as Figure 3.11 except for the observation period during 4–6 June 1992.

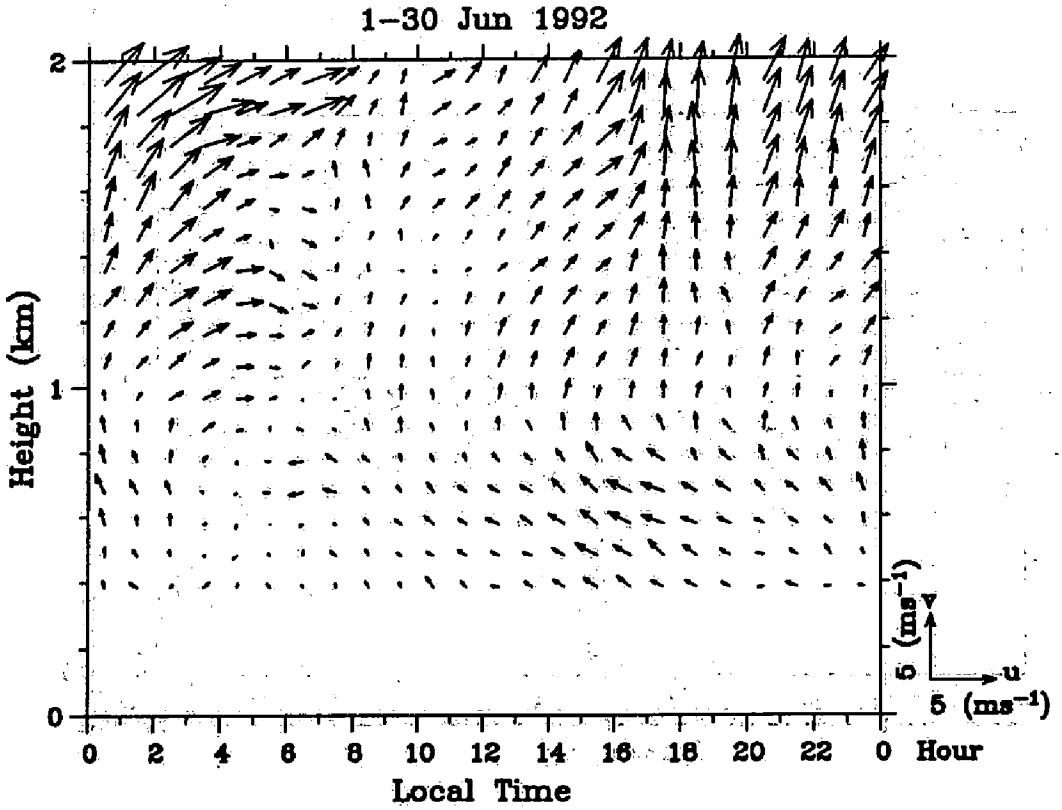

Figure 3.15: Monthly-mean daily variation of horizontal wind in June 1992. Vectors are directed upward for a northward component, and towards the right for a eastward component.

between the inside and outside of the PBL, rather than by the turbulence activities. Turbulence activity shows two maxima everyday; one appears just below the ascending top of the PBL in the morning, and the other appears inside the PBL in the afternoon. The latter is associated with the convective motions mentioned in Subsection 3.2.2.

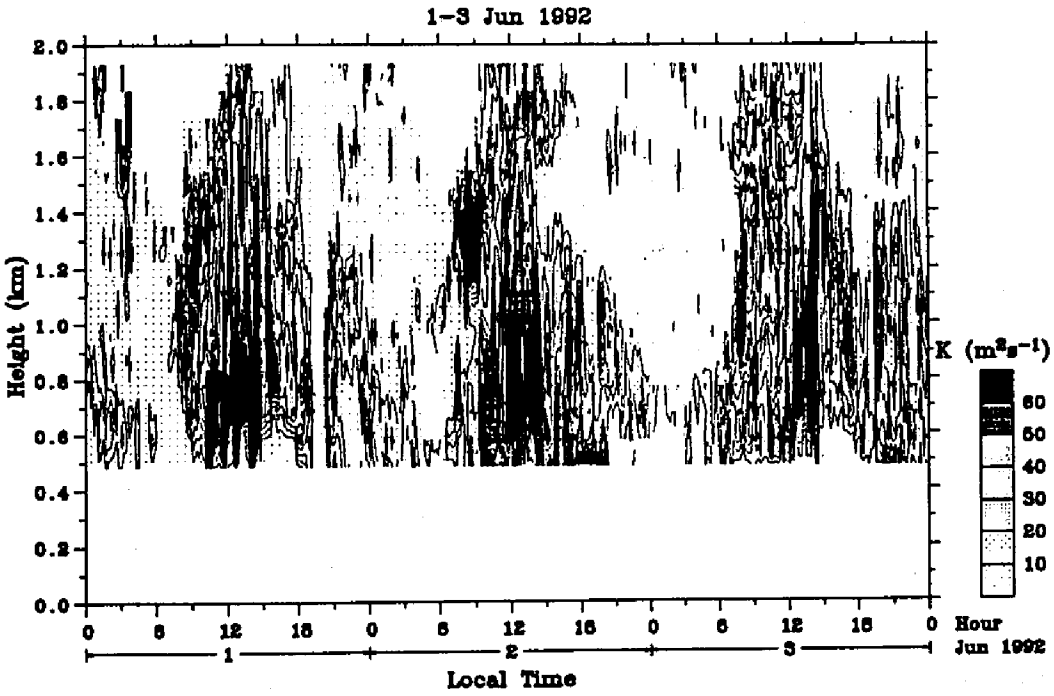

Figure 3.16: Time-height cross section of the vertical eddy diffusivity during 1–3 June 1992 calculated from spectral width averaged every 10 min.

3.2.4 Discussion and concluding remarks

We have found several features of diurnal variations of the PBL that developed on clear days. Here we present Figure 3.17 which shows that the observational evidence by the BLR are quite consistent with the evidence speculated or predicted numerically by *Yamada and Mellor* [1975]. Although their studies treated the PBL over a plain orography (the Wangara experiment in Australia), the present BLR observations were conducted among small mountains. A stable PBL top below which strong turbulence (mixing) is distributed can be detected with the BLR as the strong echo layer, which seems very similar to features at

the tropopause and at frontal surfaces [see, e.g., *Gage and Green*, 1978; *Röttger*, 1979; *Larsen and Röttger*, 1983; *Fukao et al.*, 1989; *Larsen et al.*, 1991]. Utilizing this feature, we may study detailed variations of the PBL (mixing layer) top level. For example, the PBL top becomes smeared in the afternoon, but it goes up and down together with convective motions inside the PBL.

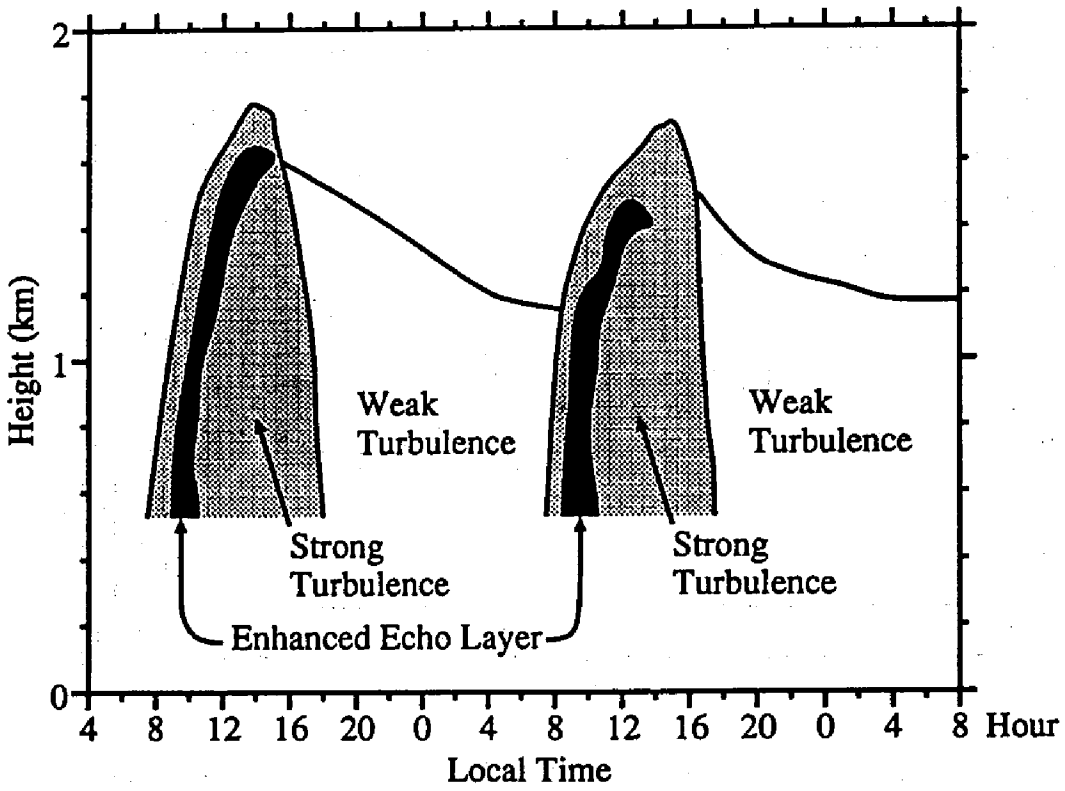

Figure 3.17: Schematic diagram of time evolution of the PBL observed with the BLR, adapted from *Yamada and Mellor* [1975].

Considering all the observational features described in this section, we conclude that a remarkable diurnal variation can appear in the PBL (or mixing layer) even over a hilly orographic situation, if the weather is fine and the larger-scale wind direction is suitable. The radar site of the present study is surrounded by small mountains, but is relatively opened to a lake (the Lake of Biwa, 671 km^2) located at a distance $\sim$ 30 km northward from the site. Thus, in the present case, the situation is suitable for generating a remarkable diurnal variation similar to that over a plain, if the dominant larger-scale wind blows southward. Such a

local situation is considered to produce the results somewhat different from those obtained over a plain in the U.S. by *May and Wilczak* [1993].

Chapter 4

Observation campaign in equatorial Indonesia

In this chapter, we describe the outline of the observation project in equatorial Indonesia in Section 4.1, and the performance of the BLR in Indonesia, mainly concerning the observation height range and the wind measurement reliability in Sections 4.2 and 4.3, respectively.

4.1 Outline of the observation project

It is recognized that large year-to-year variations in cloud convection over a maritime continent around Indonesia are closely related to the behavior of an anomalous weather condition, known as El Niño-Southern Oscillation (ENSO). Recent studies further revealed that active cloud convection generates various atmospheric waves, such as Kelvin waves, mixed Rossby-gravity waves, atmospheric tides, and gravity waves [e.g., *Andrews et al.*, 1987]. The wave energy thus deposited is transported both vertically and horizontally for a long distance.

While, tall cumulus clouds, exclusively generated near Indonesia, sometimes penetrate above the tropopause, which transport the tropospheric air into the stratosphere, resulting in upward flux of various minor constituents [*Holton*, 1984]. Thus, the equatorial atmosphere over Indonesia seems to play an important role upon global change of the earth's atmosphere. Yet, its detailed characteristics remain unresolved, because accurate observations have not been fully carried out so far.

We aimed to observe characteristics of cloud convections and atmospheric waves in the troposphere and middle atmosphere over Indonesia by means of ground-based observation techniques. Through collaboration between Japan (RASC

(Radio Atmospheric Science Center) of Kyoto University) and Indonesia (BPPT (Agency for the Assessment and Application of Technology) and LAPAN (National Institute of Aeronautics and Space)), we established a radar observatory at PUSPIPTEK (Indonesia National Center for Research, Science, and Technology) in Serpong (6.4°S, 106.7°E, 50 m above sea level), West Java, which is located in the south-west suburbs of Jakarta (see Figure 4.1) [*Tsuda, et al.*, 1995]. We installed in the radar observatory a meteor wind radar (MWR) [e.g., *Tsuda et al.*, 1988; *Nakamura et al.*, 1991; *Tsutsumi et al.*, 1994] in addition to the BLR as shown in Figure 4.2. In contrast with the BLR which measures wind velocity profiles in the lower troposphere, the MWR measures wind velocity and temperature profiles in the mesosphere by using the echo from a meteor trail.

Observations with the radars can be automatically continued under the supervision of a system computer without the full-time attendance of an operator, except for exchange of data tapes every 4–5 days. When electric power is somehow shut down, the computer, driven by a backup battery (UPS), automatically stops radar operation. In such an accident, an operator needs to reboot the operation system to restart the radar. Therefore, daily system-check has been regularly repeated by a technician of PUSPIPTEK to report the system condition.

In association with radar observations, we conducted rawinsonde measurements of horizontal wind velocity, temperature, and humidity, with a height resolution of 150 m, at LAPAN in Bandung (6.9°S, 107.6°E, 740 m above sea level), about 100 km east of the radar site. We employed a Väisälä DigiCORA (MW11) sounding system with meteorological balloons provided by TOTEX Co. Ltd. (TA-1000, TX-1000, and CR-600). Rawinsondes were launched four times a day at 05, 11, 16, and 23 LT during 16 November 1992–10 April 1993. Unfortunately, the sounding was stopped due to malfunction of a receiver on 20–30 November 1992, and from 17 December to 11 January 1993. In total, 411 balloons were launched, where 362 (88%) and 293 (71%) out of them reached 18 and 30 km, respectively. Although very low temperature near the tropopause sometimes caused a balloon burst at night, the TX-1000 balloon normally reached above the tropopause.

Besides international campaigns, we also conducted intensive observations in the dry and rainy seasons in order to study differences of the behavior between dry and wet atmosphere in tropics. The dry and rainy season campaigns were successfully conducted on 8–15 October 1993 and 15–22 February 1994, respectively. Over 50 rawinsondes were launched every 3 hours from the radar site. Fundamental meteorological parameters were also monitored in the ground, with an anemometer (surface winds; OGASAWARA, WS-A54), rain gauge (IKEDA, RT-5), pyranometer (solar radiation; EKO, MS-42), net pyrradiometer (net radiation; EKO, MF-11), and temperature and humidity sensors (VAISALA, HMP-133Y).

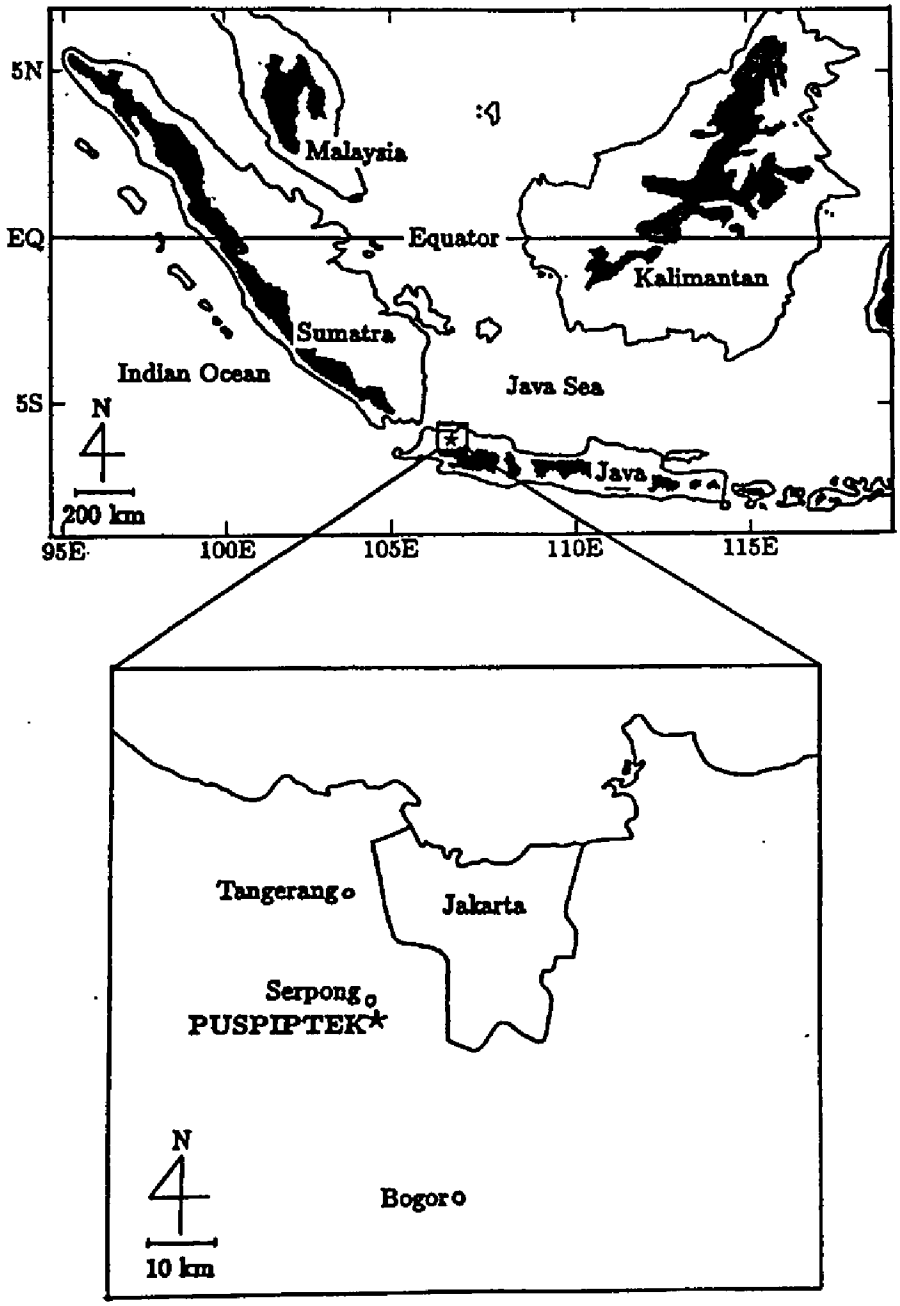

Figure 4.1: Map of the radar observation site at PUSPIPTEK in Serpong, Indonesia. Regions higher than approximately 450 m above the mean sea level are shaded.

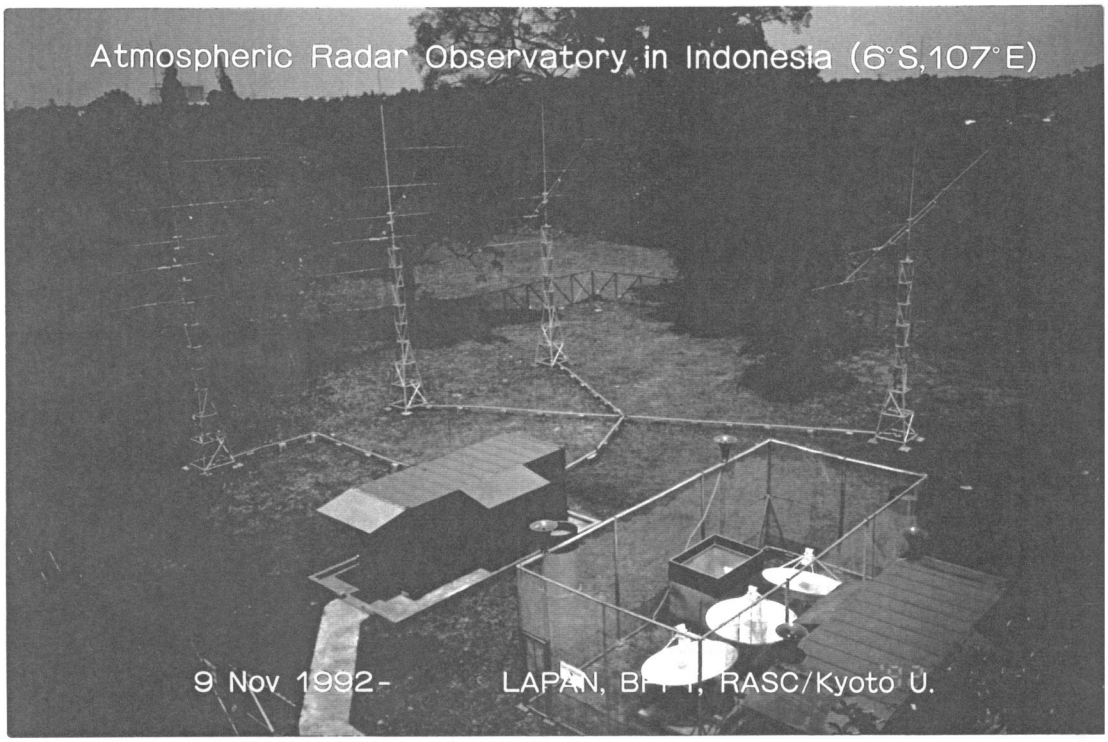

Figure 4.2: Radar observatory in Indonesia. Three parabolic antennas for BLR (right-bottom) and four five-element Yagi antennas for MWR were constructed. Loud speakers are used for RASS temperature measurements. All the radar equipment except for antennas is stored in two containers. Instruments for surface weather measurements, including anemometer, are also installed in the observatory.

Observations with the BLR and rawinsondes were carried out fairly continuously, as shown in Figure 4.3, except for several major gaps, such as in June–July 1993 for the BLR. Some of accidents were caused by a near-by lightening. Although Figure 4.3 shows the observation period as of the end of 1994, radar operation will be continued, at least, by the end of 1996, in order to cover one full cycle of ENSO. Daily sounding of rawinsondes was again commenced by LAPAN in Bandung, but once a day at 07 LT, from October 1993.

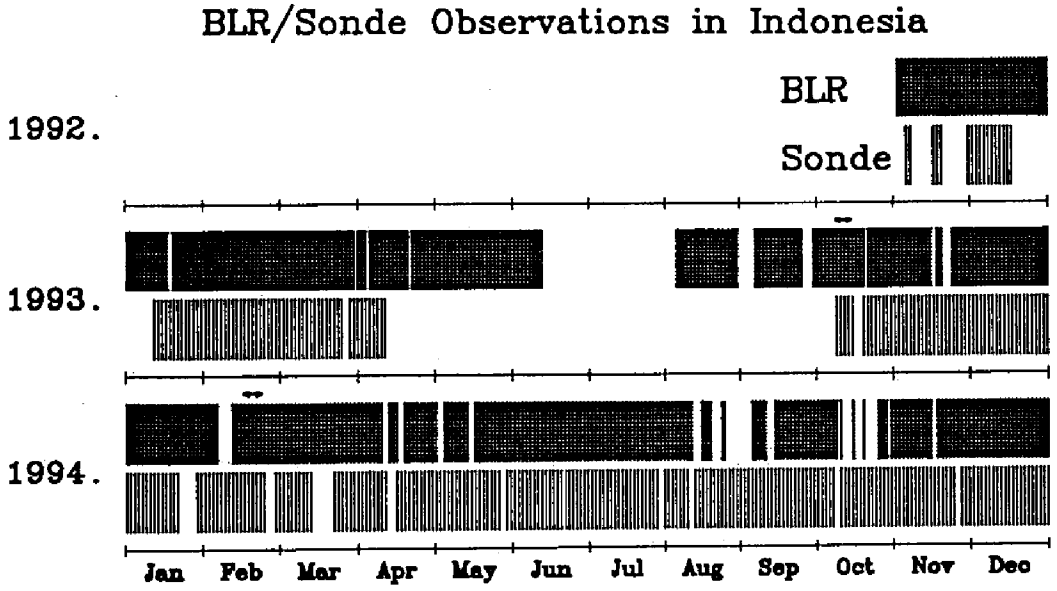

Figure 4.3: Observation periods of the BLR at PUSPIPTEK in Serpong, and rawinsonde soundings at LAPAN in Bandung, Indonesia (as of the end of 1994). Double-head arrows indicate campaign observations (see text for details).

Review of rawinsonde observation results in Bandung, Indonesia

Analyzing profiles of wind velocity and temperature fluctuations observed with rawinsondes during November 1992–April 1993, *Tsuda et al.* [1995] studied the propagation characteristics of atmospheric waves in the troposphere and stratosphere. Figure 4.4 shows a contour plot of low-pass filtered zonal winds, with a cut-off period at 4 days, together with relative humidity. Note that the tropopause was located at about 17 km.

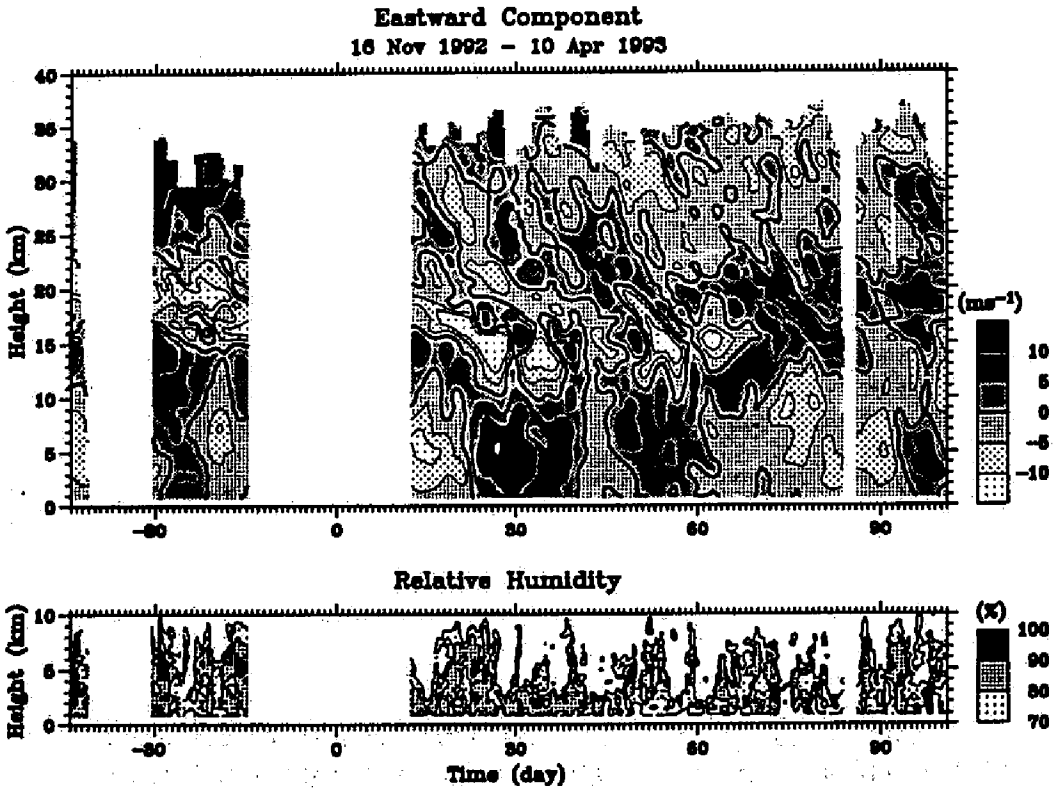

Figure 4.4: Fluctuating components of eastward winds (top panel), after processing a low-pass filter with a cutoff of 4 days at each height, and relative humidity (bottom panel). Horizontal axis indicates day number relative to 1 January 1993.

In Figure 4.4 we could detect a variety of wave activities in both troposphere and stratosphere. In particular, we detected an oscillation with a dominant period of about 27 days below about 10 km in January–February 1993, which seemed to be a manifestation of a 30–60 day oscillation in the tropical troposphere. The amplitudes of the oscillation decreased with time during days 20–60 in Figure 4.4, which correlated well with the time variation of relative humidity, which seems to represent the cloud activity.

Above about 15 km, phase progression along height became evident, with phase velocity being faster above about 20 km. We also analyzed wind fluctuations in the meridional winds and temperature, and found that the oscillation in the stratosphere could be interpreted by an equatorial Kelvin wave with periods of 10–20 days. The 20-day wave was greatly enhanced in a narrow height range at 15–20 km near the tropopause. However, the dominant wave period became shorter as about 10 days above 20 km. Note that the wind fluctuations in the stratosphere cloud naturally be connected to the perturbations in the troposphere, suggesting that the excitation mechanism of a Kelvin wave is closely related to cloud activity [e.g., *Salby and Garcia*, 1987].

We further found that the Kelvin waves also produced large temperature fluctuations near the tropopause, causing periodic variations in both the tropopause height and minimum temperature. Since exchange of air between troposphere and stratosphere is largely affected by the tropopause structure, it can be considered that the Kelvin wave activity could modulate upward flux of minor constituents in the equatorial region [*Tsuda et al.*, 1994a].

Short period fluctuations in the zonal winds were also extracted as in Figure 4.5, by applying a high-pass filter with a cut-off of 4 days on time series, considering that the Coriolis period at the site is 99.9 hours (4.16 days). Perturbations in the stratosphere were clearly characterized by downward phase progression with vertical scales of 2–5 km, being consistent with the behavior of upward energy propagating gravity waves. While in the troposphere both upward and downward propagation coexisted, showing complicated structures. These results imply that the gravity waves were generated in the troposphere, probably due to active convection [*Tsuda et al.*, 1994b].

4.2 Observational height range of the BLR

The lowest height of BLR observations is determined to be $\sim$ 300 m from the delay between signal transmission and reception. However it is significantly affected by both ground clutter and atmospheric echoing properties [*Fukao et al.*, 1995; *Hashiguchi et al.*, 1995b]. Figure 4.6 shows the ratio of effective samples

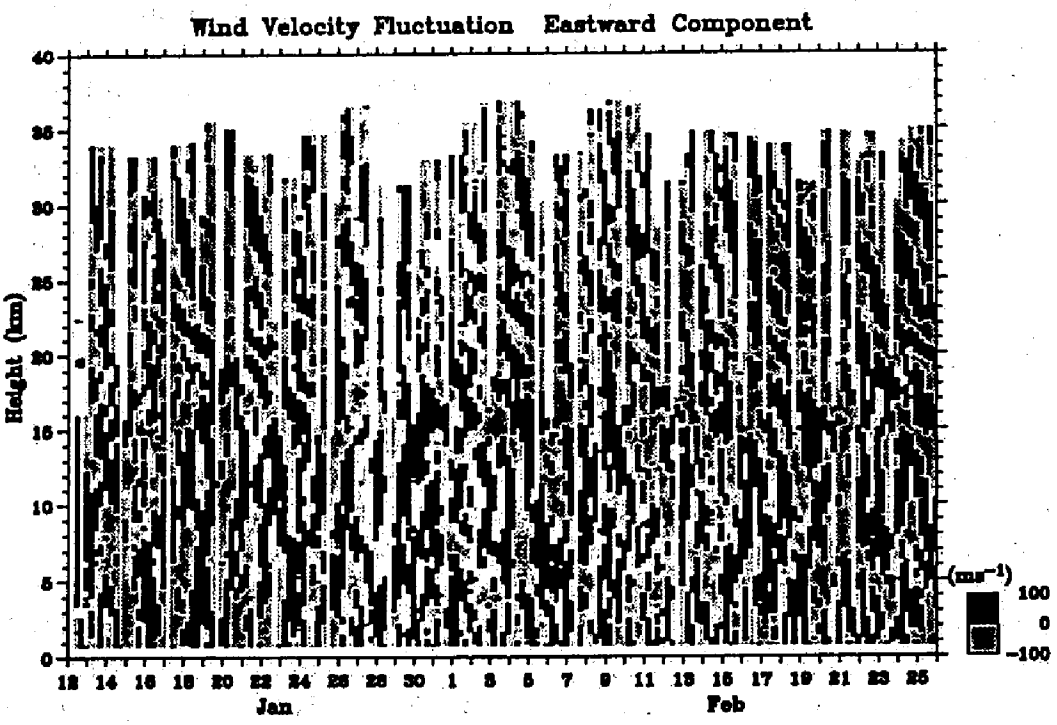

Figure 4.5: Fluctuating components of the eastward winds after processing a high-pass filter with a cutoff of 4 days, observed with rawinsondes during 12 January–25 February 1993. Note that darkly shaded area indicate positive deviations.

to all samples over one hour with a height resolution of 100 m. Wind velocities below 600 m were difficult to obtain (probability < 80 %) in Shigaraki whereas in Serpong wind velocities can be obtained from 300 m, which is the system limit of the BLR. This is because the ground clutter level is reduced in Serpong, since we selected the radar site without any surrounding mountains or tall buildings, lowered the antenna height, and constructed a clutter prevention fence around the antennas.

The maximum height of BLR observations depends on echo intensities from the atmosphere. In the clear atmosphere without precipitation, the echo intensity increases with humidity, temperature, and their vertical gradients. This is why the height coverage was normally limited to below 2.2 km (with probability $\geq$ 80 %) in Shigaraki, while it increases to 3.2 km in Serpong owing to higher humidity and temperature. It is noted that the highest height in Shigaraki was a little lower than 3 km even under conditions with the highest humidity and temperature in August. For the same reason, the height coverage shows large variations depending on local time. On clear days the height coverage is highest in mid-afternoon and lowest during the night-time. The *L*-band radar is very sensitive to precipitation particles (raindrops or drenched ice crystals), so that the height coverage is greatly increased. Precipitation echo is extended occasionally up to near the tropopause height under conditions of deep convection [*Williams et al.*, 1994], although the data are sampled up to only 6.4 km height in routine observations.

4.3 Comparison of wind and temperature fields with simultaneous rawinsonde observations

As described in Chapter 3, the BLR detects the mean radial Doppler velocity inside a sampling volume given by the beam width of 7.6° for one beam and the vertical resolution of 100 m. The vertical velocity determined by using one vertical beam corresponds to the mean value for a volume of roughly 130 m wide and 100 m thick at 1 km height. Since the zonal and meridional velocities are determined by using vertical and 15°-oblique beams, these velocity components are the mean values for a volume of about 400 m wide and 100 m thick at 1 km height under an assumption that the wind fields are homogeneous in this volume. The estimated velocities can be regarded as instantaneous values in time taken at the sampling interval ($\approx$ 1 min), although some averaging is required to obtain reliable values. We have compared wind velocities obtained simultaneously with the BLR and rawinsondes (VAISALA, RS80-15N; launched at the radar site every

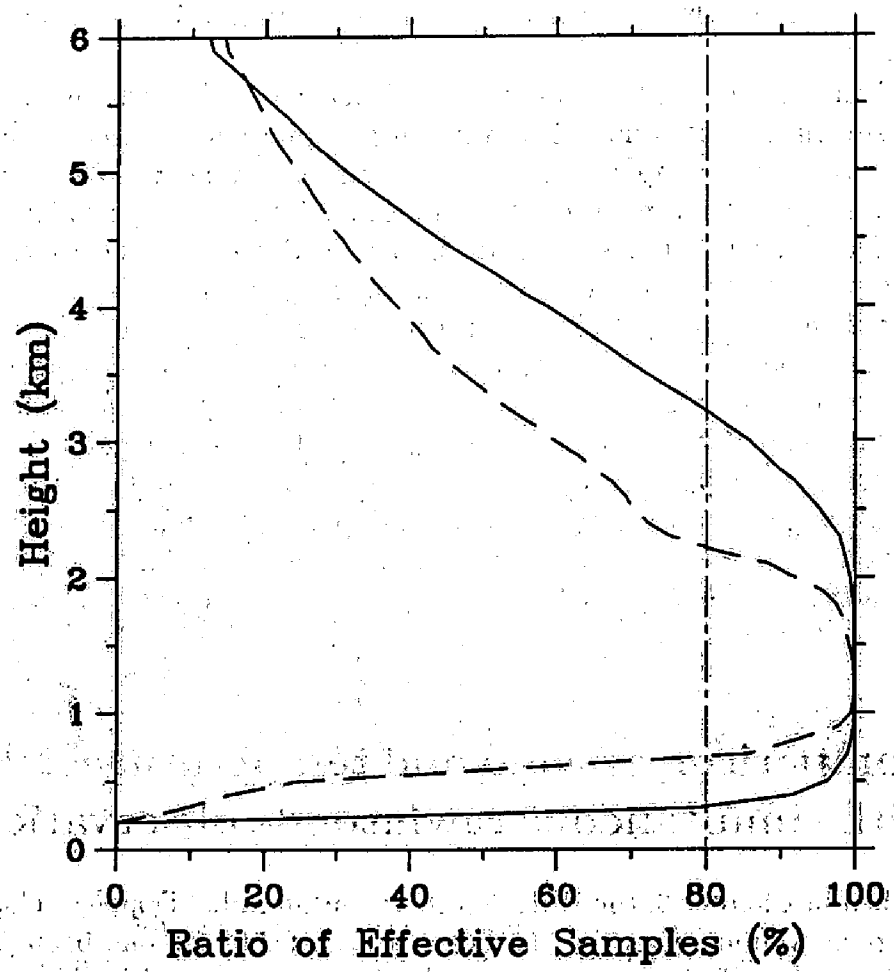

Figure 4.6: Height coverage of effective samples of BLR echoes obtained during one hour, calculated for November 1992–February 1994 in Serpong, Indonesia (solid curve) and April–August 1992 in Shigaraki, Japan (dashed curve).

three hours) during 8–15 October 1993. Considering that a rawinsonde took about 15 min to pass through the observation height range of the BLR, we have averaged the BLR data over 15 min after the launch time of the rawinsondes. As shown in Figure 4.7, both wind profiles coincided fairly well without any significant biases, and the BLR detected smaller-scale variations compared with those of the rawinsondes. The inherent accuracy for the BLR wind measurements is better than 1 m s^{-1} [*Fukao et al.*, 1995]. Figure 4.8 shows the diurnal variation of root-mean-square differences between the two techniques for (a) zonal and (b) meridional components. The RMS differences were better than 3 m s^{-1} almost all of the time, but at 03 LT large differences, which are possible contaminations due to birds and/or insects, discussed further below, were obtained. It is noted that the BLR can obtain three-dimensional wind profiles (including vertical velocity only when there is no precipitation) with higher vertical and temporal resolutions than rawinsondes.

In addition, we sometimes observed strong echoes below the Type 2 echo layer of Figure 5.1 in Chapter 5, in particular in the night-time. We examined every samples of these echoes, and found a discontinuity in height and time in the shape of the Doppler frequency spectrum. We consider that such echoes may be contaminations due to birds, bats, or insects [e.g., *Browning and Atlas*, 1966; *Lhermitte*, 1966; *Röttger and Larsen*, 1990; *Wilczak et al.*, 1994]. In order to remove this contamination, we fitted a Gaussian function to the data neglecting any peak that was not continuous in height and time. We will investigate in detail these echoes and appropriate reduction procedures in the future.

Figure 4.9 shows an example of temperature measurements with BLR/RASS on 10 October 1993, in comparison with a simultaneous rawinsonde measurement. Typical difference between RASS and rawinsonde measurements was about 0.5 K. The standard deviation in Figure 4.9 represents the range of temperature perturbations in 30 min. It is noteworthy that RASS determines virtual temperature, which was higher than atmospheric temperature by 2–4 K because of high humidity in the tropical PBL. Since the vertical gradient of virtual temperature is a direct measure of atmospheric stability, RASS measurement is useful in investigating the characteristics of convection.

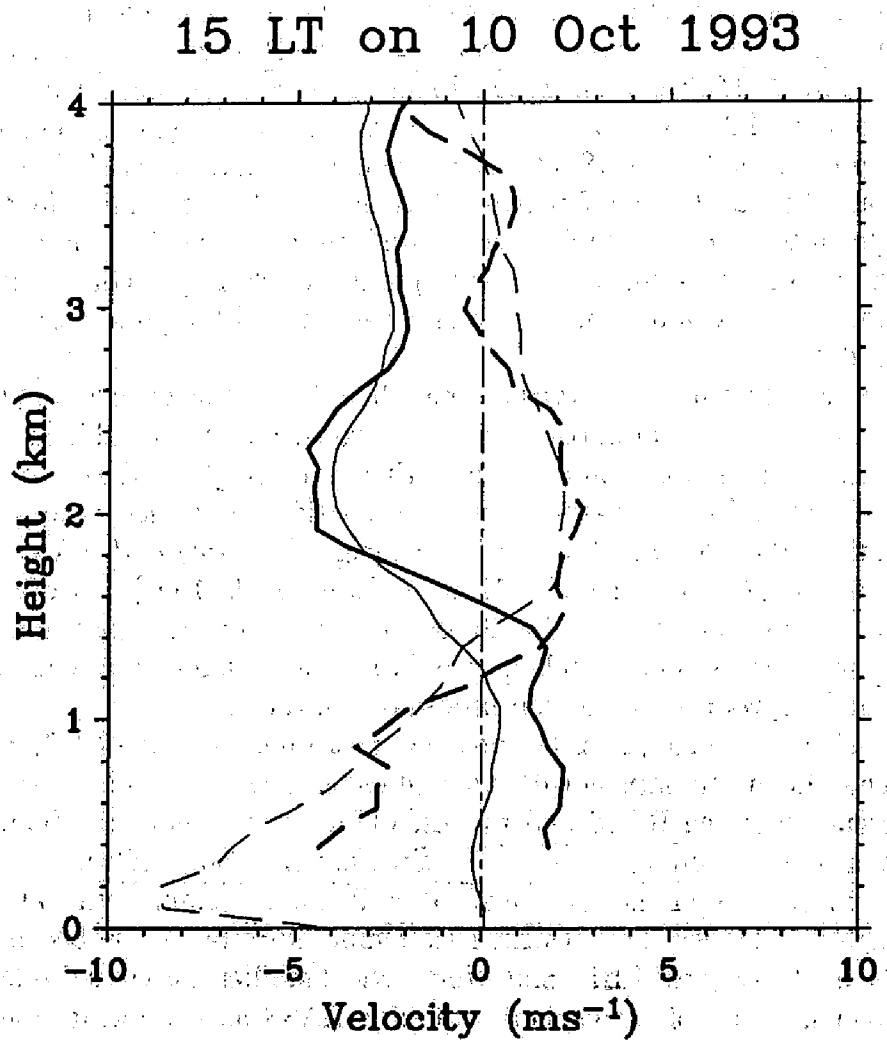

Figure 4.7: Profiles of zonal (solid curves) and meridional (dashed curves) wind velocities, which were obtained simultaneously with the BLR (thick curves; averaged over 15 min) and rawinsondes (thin curves; VAISALA, RS80-15N) at about 15 LT on 10 October 1993.

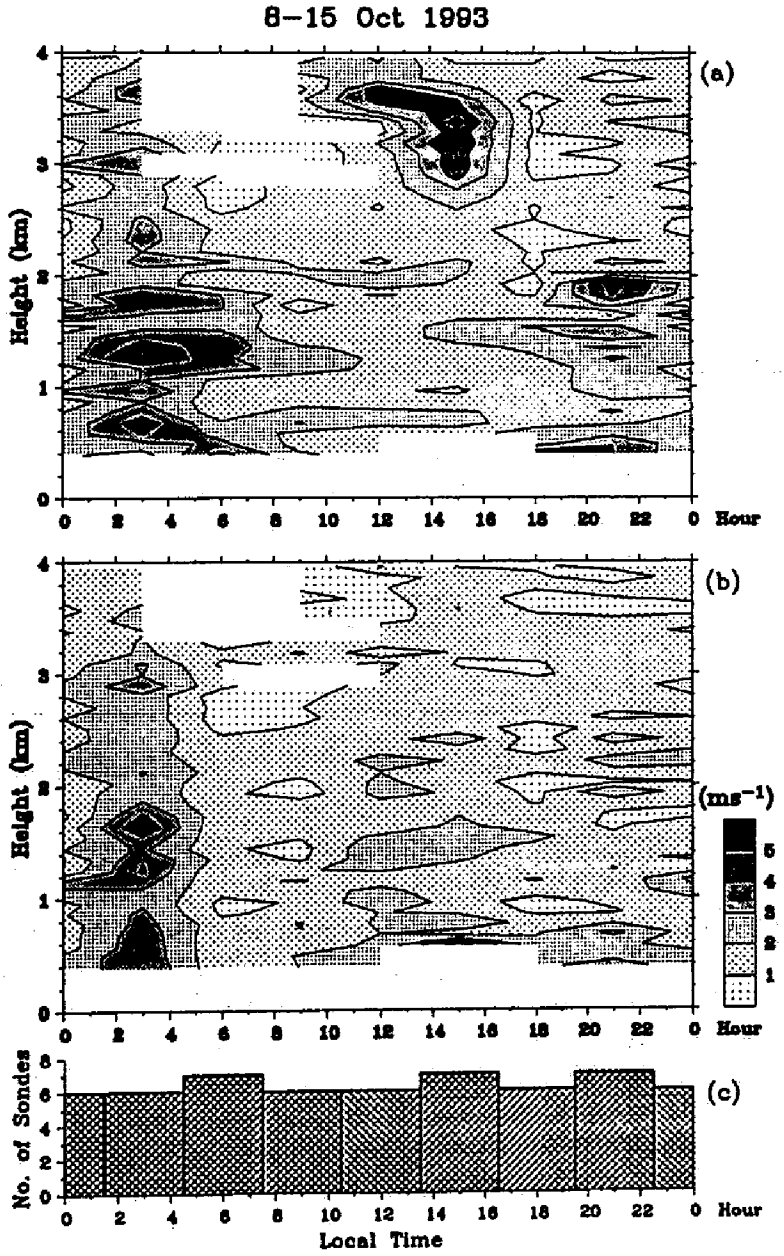

Figure 4.8: Diurnal variation of root-mean-square differences between the BLR and the rawinsondes for (a) zonal and (b) meridional winds obtained for 51 simultaneous observations during 8–15 October 1993. (c) indicates the number of rawinsondes launched in each local time.

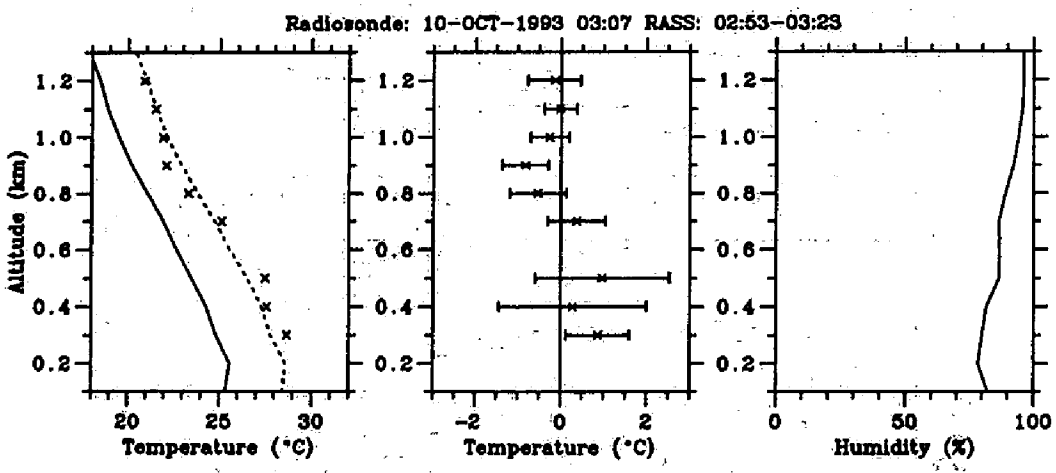

Figure 4.9: Measurements of temperature profile with BLR/RASS during 02:53–03:23 LT on 10 October 1993. Left: comparison of RASS temperature determinations (cross symbol) with atmospheric (solid curve) and virtual (dashed curve) temperature profiles obtained with a rawinsonde launched at 03:07 LT. Center: difference between RASS and rawinsonde measurements of virtual temperature, together with standard deviation for the RASS results within 30 min. Right: humidity profile obtained with a rawinsonde.

Chapter 5

Diurnal variation of the equatorial PBL

In this chapter, observational evidence concerning the vertical extent and diurnal variations of the equatorial PBL using the data observed with the BLR, rawinsondes, and standard ground-based instruments in the dry season campaign (8–15 October 1993) is described.

5.1 Radar observations of the PBL

Figure 5.1 shows the time-height cross section of echo intensity (equivalent radar reflectivity factor) observed with the BLR in Serpong during 10–12 October 1993. Although smaller scale variations were complicated, two types of strong echo regions were found. First, every morning at about 08 LT (Indonesian Western Standard Time = UT + 7 h), a significant echo layer (Type 1) appeared at the lowest observation height (300 m) and gradually ascended up to 3–5 km height until about 16 LT. Such a layer structure is smeared in the evening, and is identified with the top of the PBL (or the mixing layer) in the following section. Secondly, another type of thin layered echo (Type 2) was observed at 2–3 km heights during 20–12 LT, descending about 300 m at around 06 LT every morning. These three days were typical clear days (without any precipitation at the ground) in the dry season, and observations on other clear days showed similar diurnal variations of echo power intensity. Figure 5.2 shows the time-height cross section of echo intensity observed during 16–18 February 1994 in the rainy season campaign. In the rainy season the features of diurnal variations mentioned above were weak or disappeared. On rainy days strong echoes caused by rainfall appeared, but they are entirely different and distinguished from the typical behavior

of clear-air echoes mentioned above.

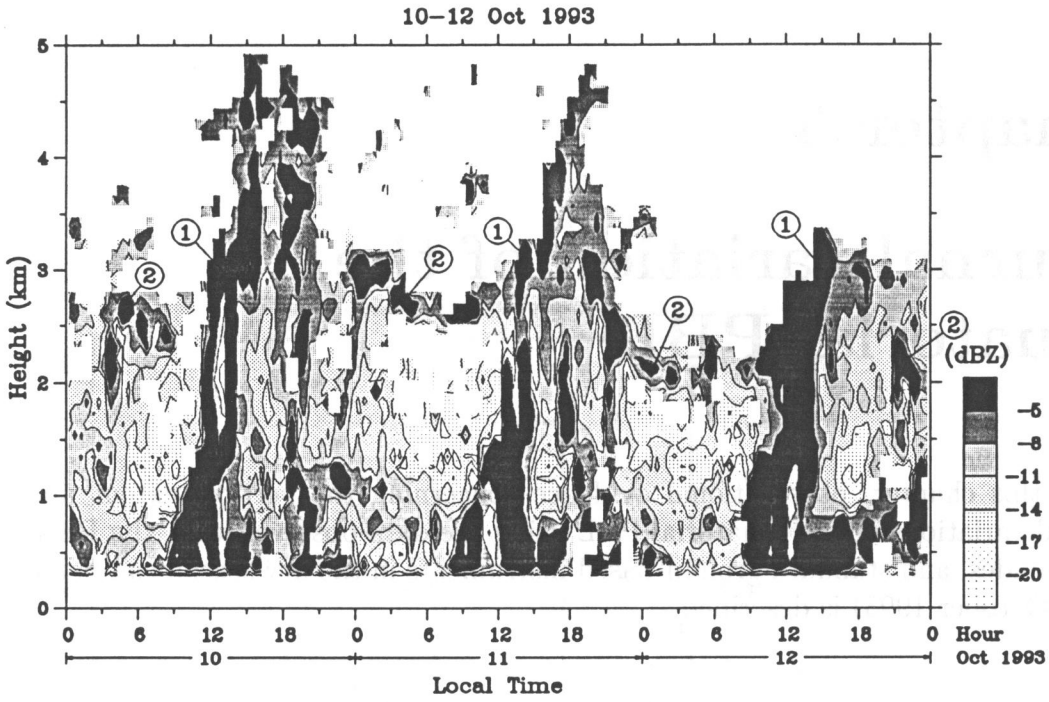

Figure 5.1: Time-height cross section of the equivalent radar reflectivity factor observed with the BLR averaged every 30 min for the eastward beam (azimuth=90°, zenith=15°) in Serpong during 10–12 October 1993. Circles with numbers indicate echo types (see text for details).

Figures 5.3 and 5.4 show variations of the three-components of wind velocity vector observed with the BLR. We found that the wind direction and speed changed drastically near the Type 1 (ascending) echo layer in the daytime and also near the Type 2 (2–3 km height) echo layer in the night-time. Below the Type 1 echo layer (or inside the mixing layer) the horizontal wind was generally weak and the vertical velocity was strong and highly variable. Below the Type 2 echo layer, both the horizontal and vertical velocities were variable, although the vertical velocity fluctuations were relatively weaker than those below the Type 1 echo layer. Above these two types of layers, an easterly wind was dominant throughout the observational period (at least in this season). The downward vertical velocities were observed below 1 km around 12 LT throughout the observational period. It is possible that this was very light precipitation which cannot be measured by the rain gauge on the ground.

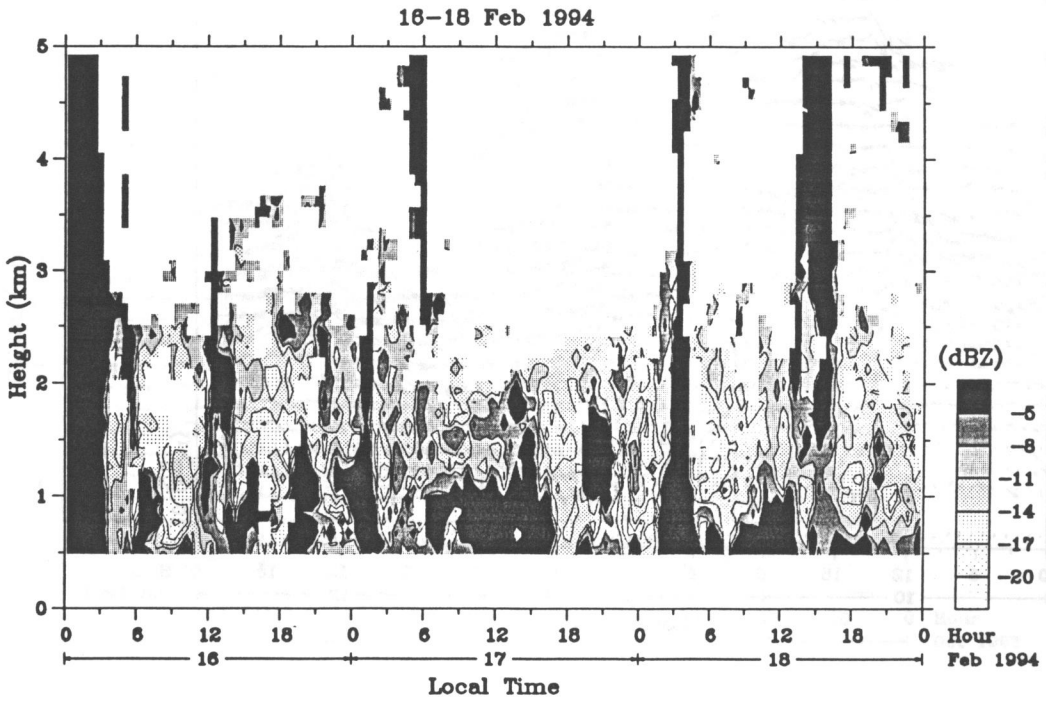

Figure 5.2: The same as Figure 5.1 except for the observation period during 16–18 February 1994.

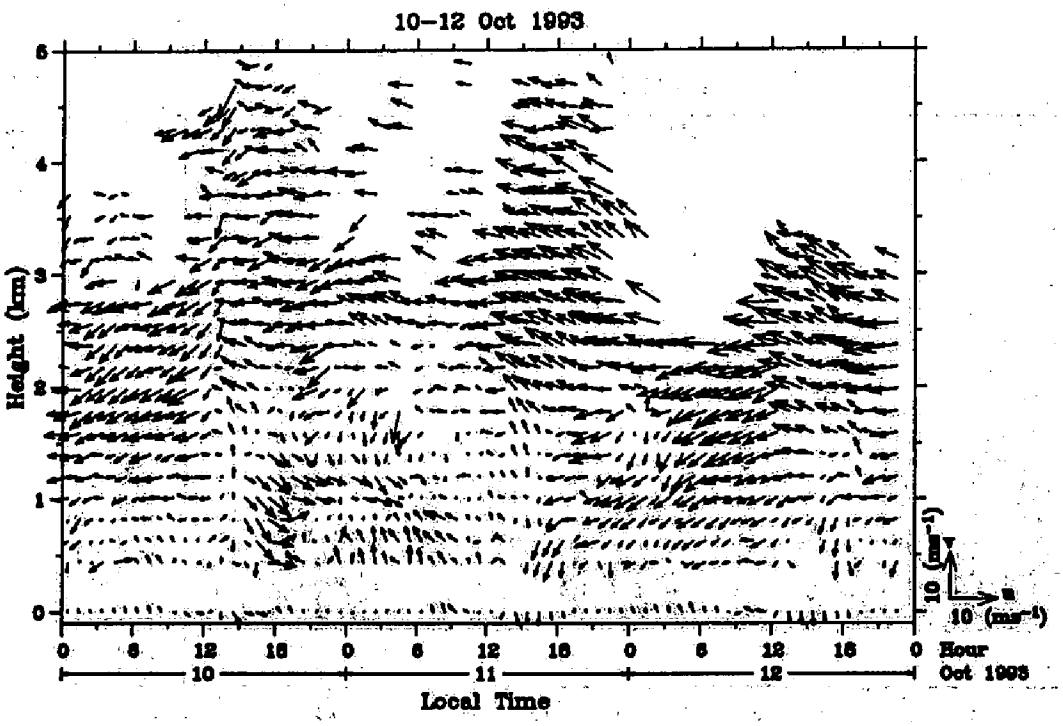

Figure 5.3: Time-height cross section of the zonal-meridional winds averaged every one hour observed with the BLR during 10–12 October 1993. The arrows plotted at the bottom are obtained with a standard anemometer (OGASAWARA, WS-A54) at about 10 m height above ground at the radar site. Vectors are directed upward for a northward component, and towards the right for a eastward component.

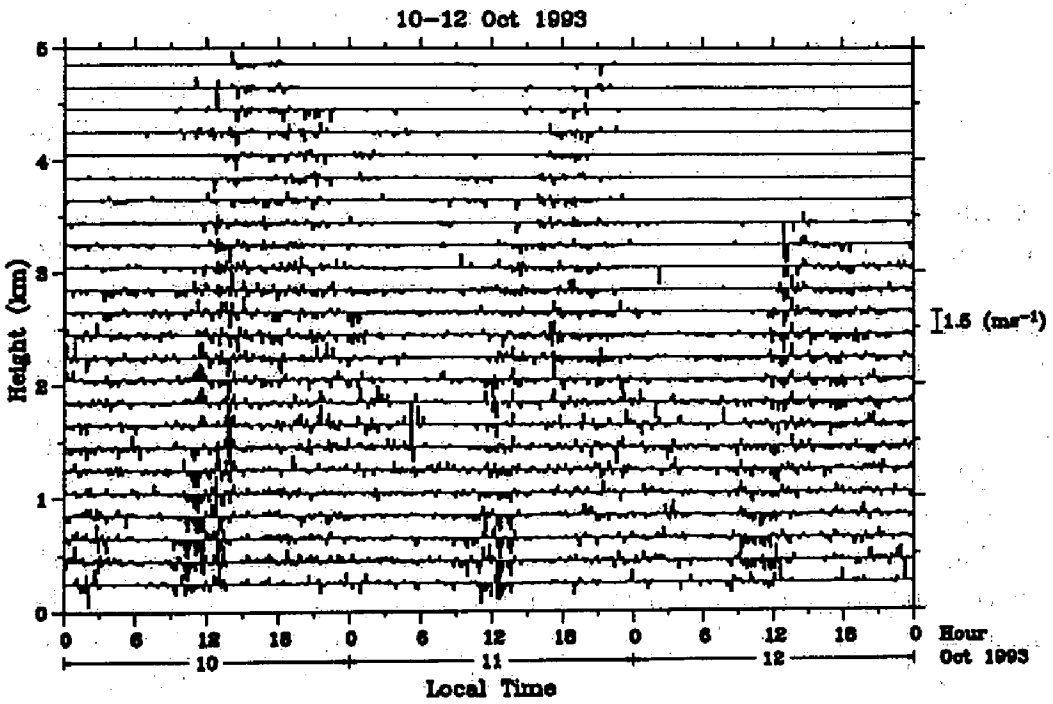

Figure 5.4: Time-height cross section of the vertical velocity averaged every 10 min observed with the BLR during 10–12 October 1993. The spacing of horizontal lines indicates a velocity of 1.5 m s^{-1}.

In Figure 5.3 surface winds (about 10 m height above the ground) monitored at the radar site with a standard anemometer (OGASAWARA, WS-A54) are also plotted. Although variations in the wind were less intense compared with those from the BLR, the wind direction tends to have northerly and southerly directions, in daytime and night-time, respectively, throughout the observational period. We consider that these diurnal variations of surface winds correspond to the sea-land breeze circulation, since the observatory is located about 40 km south of the Java coast line and there are no mountains between them. The sea breeze clearly extended to about 1 km height and there was the hint of a return flow aloft. However the land breeze was not clear in the BLR wind velocities and was, as expected, relatively shallow.

Time variations of temperature fluctuations were detected with BLR/RASS as shown in Figure 5.5, which were almost in-phase at 0.3–0.9 km heights. Temperature rapidly increased at 09–13 LT, reached the maximum at around 14 LT, sharply dropped by 18 LT, then gradually decreased at night. Maximum temperature difference in the diurnal variation was as large as 10 K at 0.3 km height, and decreased to 6 K at 0.8 km height. The Brunt-Väisälä frequency squared at about 0.5 km, derived from RASS profiles (not presented here), became persistently negative during daytime, indicating that the atmosphere was convectively unstable due to intense solar heat input.

Figure 5.6 shows the time-height cross section of the meridional wind velocity observed with the BLR during 8–15 October 1993 (dry season) and 15–22 February 1994 (rainy season). We confirm again that there exists diurnal variations corresponding to the sea-land breeze circulation in the dry season. However such diurnal variations are not observed in the rainy season. In the dry season the wind variations in the upper altitudes (higher than 2 km) occur later than in the lower altitudes although such features are not obvious in the rainy season. Figure 5.7 shows the time-height cross section of the zonal wind velocity. Easterly winds are observed in the dry season (particularly above 2 km height), while westerly winds are observed in the rainy season. This wind reversal between both seasons is discussed in detail in Chapter 6.

5.2 Meteorological features of the PBL

We found from pyranometer (EKO, MS-42) data (Figure 5.8) that after sunrise at around 06 LT, solar radiation started to increase rapidly on the ground from 07 LT until around 12 LT. Apparently there were not many clouds before noon. In the afternoon on 11 and 12 October, clouds appeared frequently during 12–14 LT, getting less frequent after that until sunset at 18 LT. On 10 October relatively

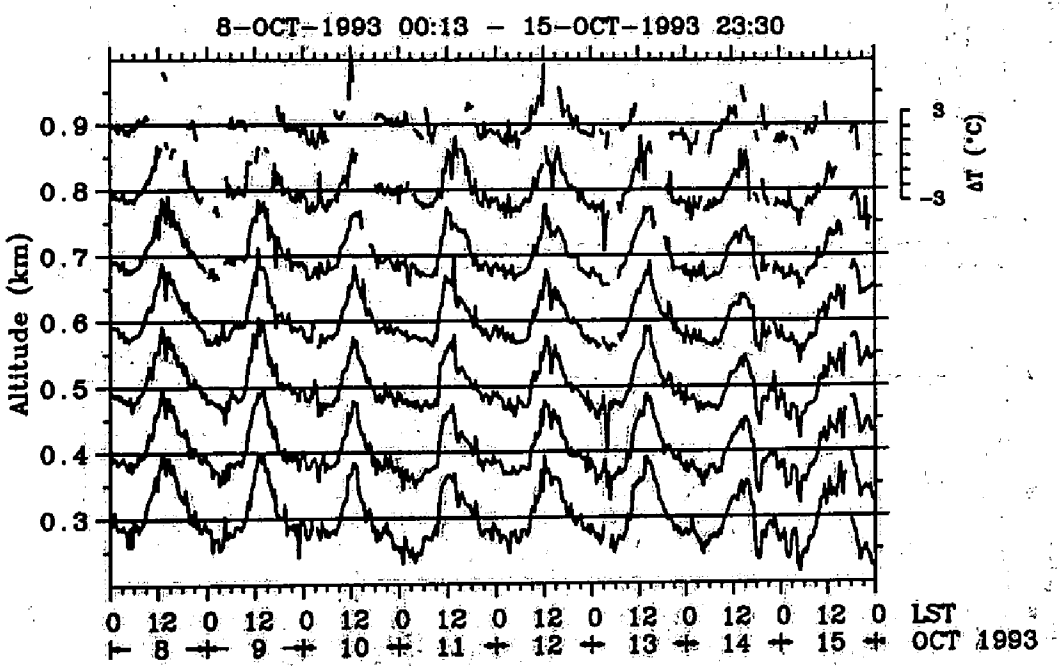

Figure 5.5: Diurnal variations of temperature fluctuations at 0.3–0.9 km heights, measured with BLR/RASS during 8–15 October 1993.

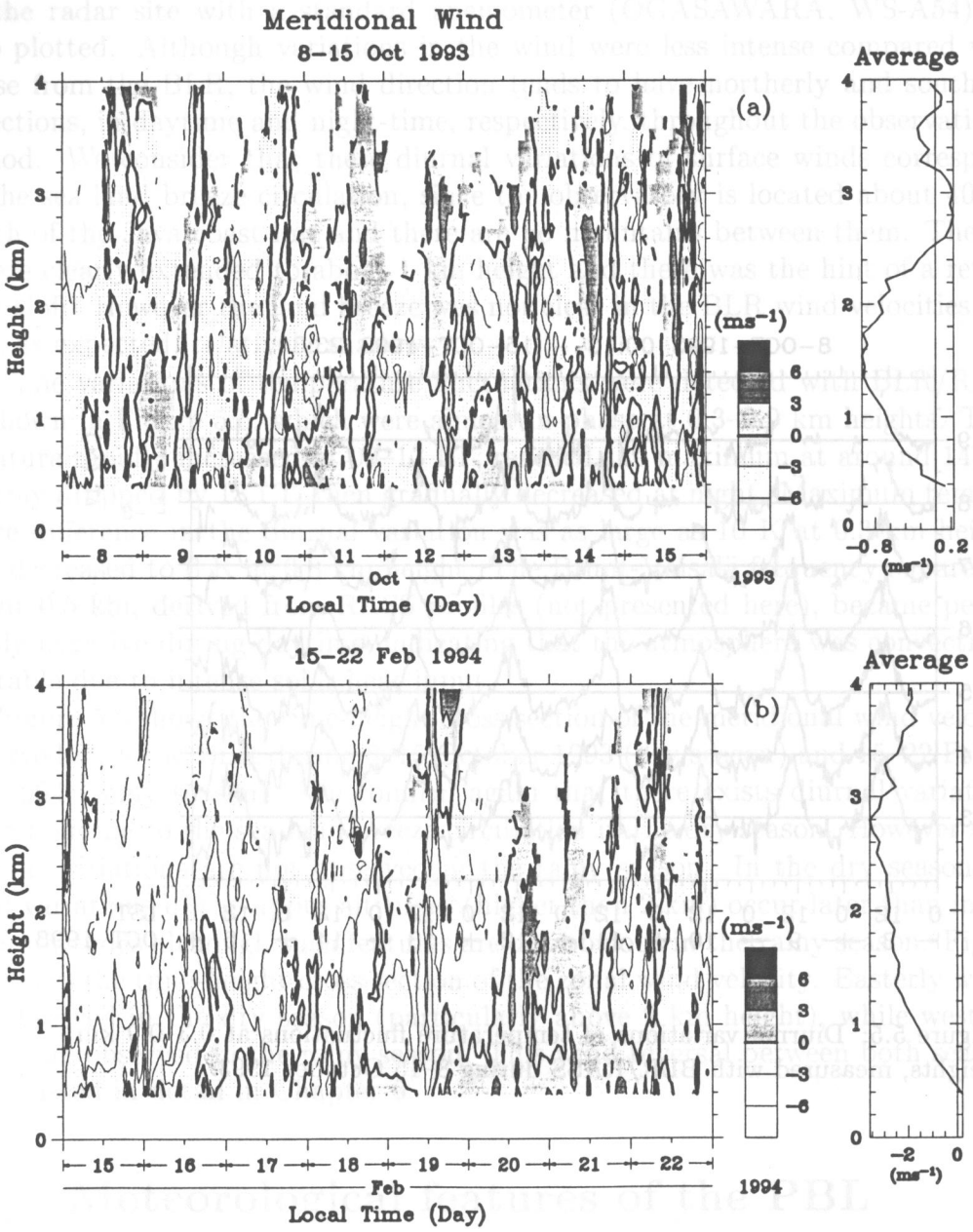

Figure 5.6: Time-height cross section of the meridional wind velocity averaged every 1 hour (left panels) and height profiles of averaged wind (right panels) observed with the BLR during (a) 8–15 October 1993 and (b) 15–22 February 1994.

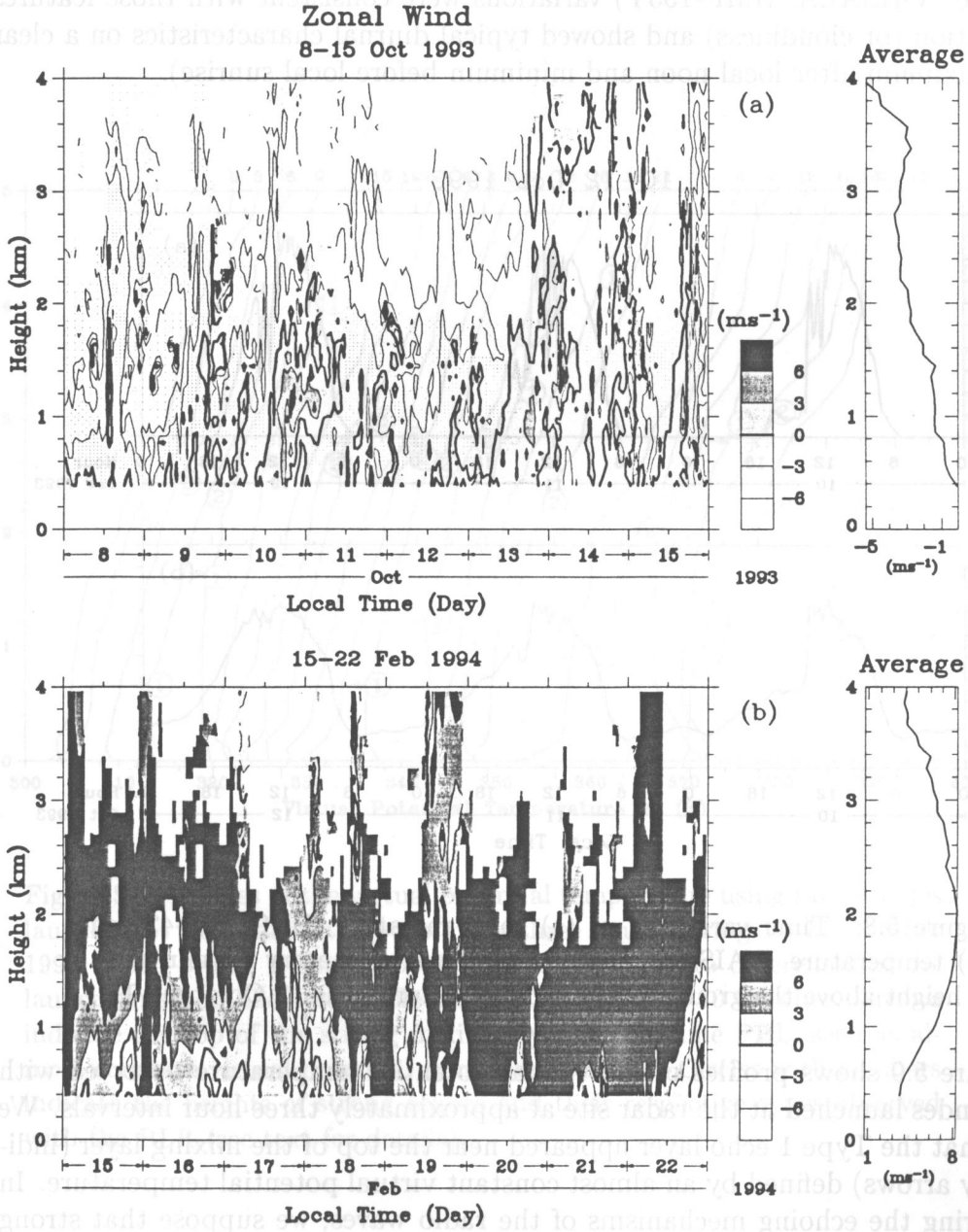

Figure 5.7: The same as Figure 5.6 except for the zonal wind velocity.

thick clouds covered the site almost continuously during 14–16 LT, although such a difference is not clear in the echo power and wind variations. The surface temperature (VAISALA, HMP-133Y) variations were consistent with those features of radiation (or cloudiness) and showed typical diurnal characteristics on a clear day (maximum after local noon and minimum before local sunrise).

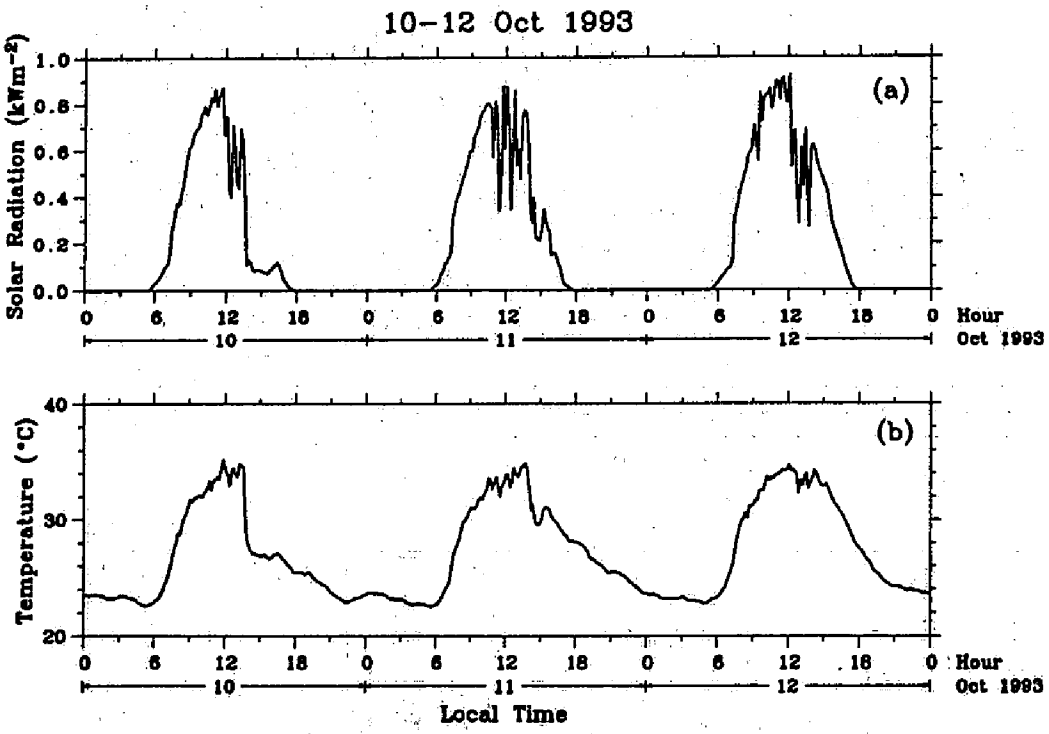

Figure 5.8: Time variations of (a) solar radiation (EKO, MS-42) and (b) temperature (VAISALA, HMP-133Y) averaged every 10 min at 1.5 m height above the ground of the radar site during 10–12 October 1993.

Figure 5.9 shows profiles of the virtual potential temperature observed with rawinsondes launched at the radar site at approximately three hour intervals. We found that the Type 1 echo layer appeared near the top of the mixing layer (indicated by arrows) defined by an almost constant virtual potential temperature. In considering the echoing mechanisms of the radio waves, we suppose that strong turbulence and vertical velocity fluctuations inside the mixing layer, and the striking gap in the vertical distributions of humidity and temperature contribute to the generation of the strong echo layer observed with the BLR [*Angevine et al.*, 1994; *Hashiguchi et al.*, 1995a].

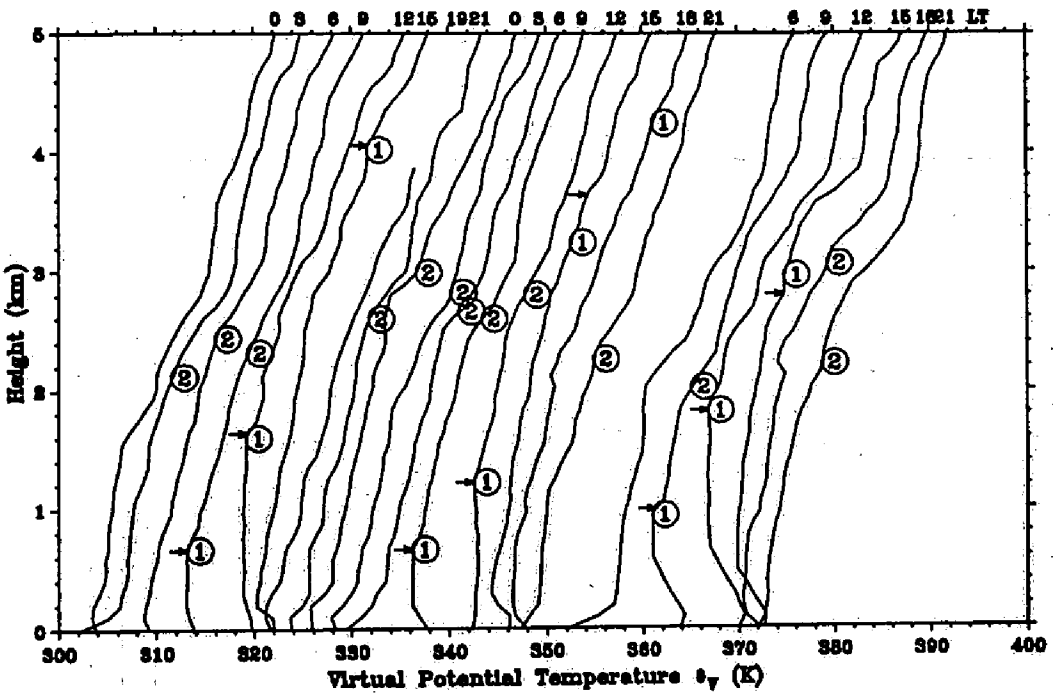

Figure 5.9: Profiles of the virtual potential temperature using rawinsondes launched at the radar site about every three hours during 10–12 October 1993. Each profile is shifted by 1 K/hour according to differences of the launch time from the first profile launched at 00 LT on 10 October. Arrows indicate the top of the strong mixing layer (or daytime PBL, seen as almost constant virtual potential temperature layer). Circles with numbers indicate the heights of strong echoes and their respective types observed with the BLR (see text for details).

Figure 5.10 shows the time-height cross section of relative humidity observed with rawinsondes. The Type 2 echo layer at 2–3 km heights corresponded to the sharp decrease of humidity with height in night-time. Such humidity gaps were also found as weak gaps of virtual potential temperature in Figure 5.9. This echo layer was similar to that observed with the 915 MHz BLR at the height of the trade-wind inversion in Hawaii, U.S. [*Rogers et al.*, 1993]. The Type 2 echo layer associated with the humidity gap was clear in Serpong in night-time, while the echo layer was observed in Hawaii in the whole day.

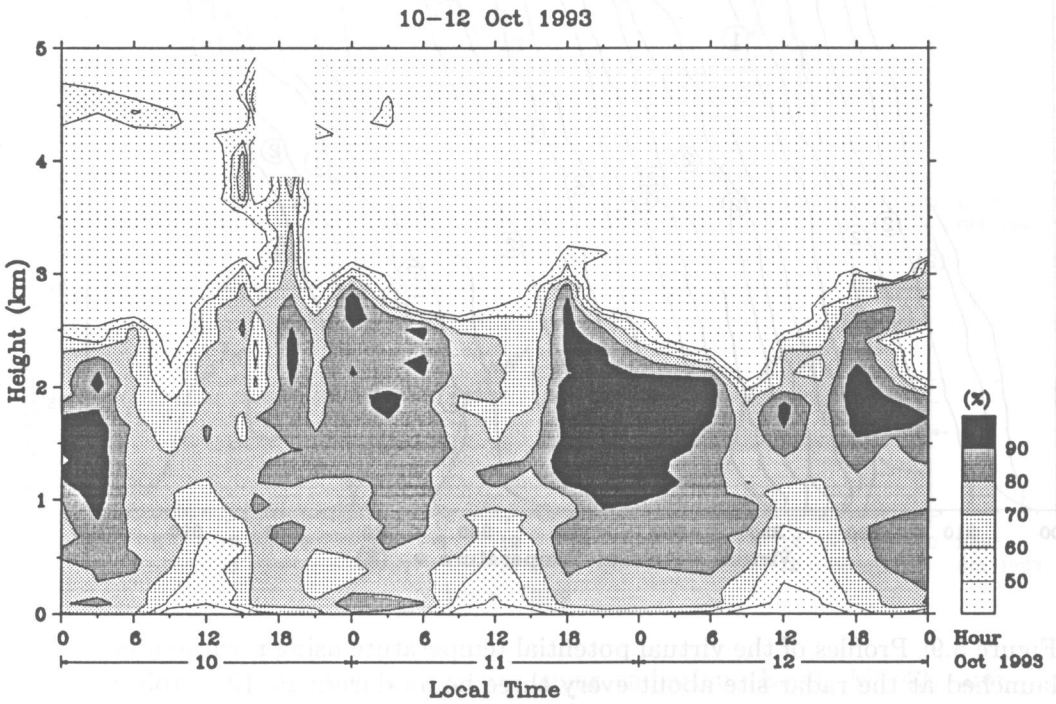

Figure 5.10: Time-height cross section of the relative humidity observed with rawinsondes during 10–12 October 1993.

5.3 Discussion and concluding remarks

The BLR has proved that there exist obvious diurnal variations of the strongly mixing PBL on clear days in the equatorial region. The observational features of the Type 1 echo layer in this study were quite similar to those observed with the BLR (see Section 3.2) and another 915 MHz radar in mid-latitudes on clear

days [*Ecklund et al.*, 1990; *Angevine et al.*, 1994; *Hashiguchi et al.*, 1995a]. The latter features were also consistent to the diurnal variations in a clear daytime PBL simulated by a numerical model [*Yamada and Mellor*, 1975]. However, the top height of such a layer in the mid-latitudes was limited up to 1–2 km, whereas that observed here in the equatorial region reached 3–5 km.

According to Ekman's classical theory described in Section 1.2, the thickness of the PBL is estimated by $\pi\sqrt{2K/f}$, where K is eddy diffusivity and f is the Coriolis' parameter. If K is constant, the ratio of the thickness in Serpong (6°S) to that in Shigaraki (35°N) becomes

$$\sqrt{\frac{\sin 35^\circ}{\sin 6^\circ}} \sim 2.3\,. \tag{5.1}$$

This prediction seems consistent with our observational results, although the interpretation of the PBL in the equatorial region is not so simple [*cf. Firestone and Albrecht*, 1986]. We should investigate in detail the differences of the thickness of the mid-latitude and equatorial PBLs in the future.

Chapter 6

Wind variation associated with cloud clusters

In this chapter, we first give a brief description of the data used in following sections. Overall features of winds, cloud activities, and rainfalls throughout the intensive observation period (IOP; November 1992–February 1993) of TOGA (Tropical Ocean-Global Atmosphere project) COARE (Coupled Ocean-Atmosphere Response Experiment) are described in Section 6.2. A striking reversal phenomenon from easterly (the Pacific Ocean trade wind) to westerly (the Indian Ocean monsoon) observed with the BLR is described in Section 6.3. This phenomenon is identified with a super cluster (the convection center) passage from west to east observed with the satellite imagery in Section 6.4. In Section 6.5 we summarize conclusions in this chapter.

6.1 Introduction

The Indonesian maritime continent is located in the center of the Pacific-Indian ocean "warm water pool" region. The world's most active atmospheric convection center exists in this region, which is believed to control the global climate including large intraseasonal and interannual variations. The approximately four-year scale El Niño-Southern Oscillation (ENSO) is considered to be triggered by the behavior and movement of such a convection center near the maritime continent [e.g., *Sumi*, 1986; *Trenberth*, 1991; *Allan*, 1991; *Lau*, 1992]. Also the 30–60 day intraseasonal oscillations are regarded as the movement of the super clusters situated there [*Nakazawa*, 1988]. Hierarchical structures of the super clusters and their relationships with the ENSO [*Lau et al.*, 1989; *Nitta et al.*, 1992] and with equatorial waves [*Takayabu and Nitta*, 1993] have also been

studied. However, because these studies were based on satellite cloud imageries and global objective analyses, detailed dynamical aspects smaller than cloud-cluster scale ($\sim 10^3$ km and ~ 1 day in horizontal and temporal scales) have not been discussed. In particular, studies of features over the Indonesian maritime continent have been quite rudimentary except for a few studies mainly based on surface observations or satellite imageries [e.g., *Estoque*, 1982; *Chang and Chen*, 1992].

During the TOGA COARE IOP, various observational techniques were integrated and concentrated into the eastern end of the maritime continent warm water pool region [*Webster and Lukas*, 1992]. Among them, wind profilers with RASS were constructed in several islands providing wind and temperature profiles with higher time and height resolutions and reliability than those previously obtained in this important region. Many of the profilers used in the TOGA COARE IOP were VHF band radars with a standard operational altitude range of 2–18 km [*Balsley et al.*, 1987, 1991; *Gage et al.*, 1988, 1991a, b, 1994; *Williams et al.*, 1992; *Sukmadradjat et al.*, 1993]. The other type of wind profilers were UHF band radars which were used for altitudes lower than 5 km [*Ecklund et al.*, 1988, 1990; *May and Wilczak*, 1993]. These VHF/UHF wind profilers were expected to improve drastically our knowledge and interpretation of the equatorial atmosphere dynamics, since classical techniques such as balloons, aircrafts, and satellites cannot observe the lower troposphere in as much detail as profilers [see, e.g., *Stull*, 1988; *Garratt*, 1992]. However, there were no wind profilers proposed in the original plan of this campaign in the center of the Indonesian maritime continent (on the western side of 140°E). The BLR has been operated in Indonesia also during the TOGA COARE IOP as described in Section 4.1.

Data used in this chapter

During the TOGA COARE IOP two surface meteorological parameters were observed with standard instruments at the radar site. These parameters were the surface winds, which are monitored with a standard anemometer (OGASAWARA, WS-A54) on a tower of about 10 m height above the ground, and precipitation (rainfall), which is automatically recorded with a rain gauge (IKEDA, RT-5).

Geostationary Meteorological Satellite (GMS) infrared (IR) data during the TOGA COARE IOP were edited by the Meteorological Research Institute (MRI). The specifications of the data used in this study are as follows:

Spatial resolution: 1° longitude × 1° latitude;
Spatial coverage: 60°N–60°S, 80°E–160°W;
Time resolution: 3 hours;
Temperature resolution: 1 K (256 levels).

We used the data to examine cloud distributions around the radar site. In order to select deep convective clouds and to exclude data from sea surface and lower clouds, we introduced an index (I_{TBB}) defined by

$$\begin{aligned} I_{TBB} &= 250 - T_{BB}, \quad \text{if } T_{BB} < 250 \text{ K}; \\ &= 0 \qquad\quad , \quad \text{if } T_{BB} \geq 250 \text{ K}, \end{aligned} \tag{6.1}$$

where T_{BB} is the area mean equivalent black body temperature in Kelvins.

Global objective analysis (GANAL) datasets prepared by the Japan Meteorological Agency (JMA) were also used in this study. The specifications of the data are as follows:

Spatial resolution: 1.875° longitude × 1.875° latitude;

Time resolution: 00Z, 12Z;

Vertical resolution: 15 levels from the surface to 10 hPa.

It should be noted that near the Indonesian maritime continent the GANAL data are mainly based on the cloud movement data by GMS [*cf. Nitta et al.*, 1986] because operational rawinsonde data are rarely obtained.

6.2 Overall features during the intensive observation period of TOGA COARE

The climatology of the Java Island is characterized by an annual cycle of the rainy (around January) and dry (around July) seasons, and is affected by both the Pacific Ocean trade wind (easterly) and Indian Ocean monsoon (westerly) circulations [see, e.g., *Allan*, 1991; *Johnson*, 1992]. The TOGA COARE IOP corresponded approximately to the rainy season at the BLR site.

Figures 6.1(b) and (c) show the time-height cross section of daily-mean westerly and southerly winds, respectively, observed with the BLR for 4 months during the TOGA COARE IOP. As described above, in November (which we considered to be around the end of the dry season) easterly winds (the Pacific Ocean trade wind) were observed above 2 km height. In and after December (rainy season) westerly winds (Indian Ocean monsoon) were observed although weak easterly winds were sometimes observed. *Sukmadradjat et al.* [1993] reported that sustained strong westerly winds were observed with a VHF wind profiler at Biak (2°S, 136°E) in the lower troposphere during the TOGA COARE IOP in the periods from late October to early November 1992, and from the end of December 1992 to early January 1993. In Serpong, sustained westerly winds were observed about one month later. That is, during early December 1992, and from late January to early February 1993. Westerly winds were at a maxima also

around the end of December and the end of February. These 30–60 day mode-like variations were clear only in the zonal wind variations, which seem to have Kelvin-wavelike structures. Although *Estoque* [1982] reported the existence of pressure disturbances with periods of approximately 20 days over the Indonesian maritime continent, such a periodicity was not so clear in the BLR winds at least during this observational period.

Figure 6.1(a) shows the time-latitude cross section of I_{TBB} along a longitude near the radar site (107°E). We found that cloud activity was very strong over the radar site throughout the TOGA COARE IOP. In particular, during January–February cloud activity over the radar site was stronger than that around the equator. Super cluster-like structures are found at 6°S latitude, corresponding to the 30–60 day-mode westerly maxima mentioned in the preceding paragraph. In late January when active clouds existed in the latitude range of 10°S–20°S on the southern side of the radar site, strong northerly winds were observed with the BLR.

Figure 6.1(d) shows the time variation of rainfall observed at the radar site. There were 3–5 day periods between the rainfall peaks particularly during January–February, which seems to be similar to the cloud cluster activity over the 6° latitude. However, the rainfall did not always correspond to the cloud activity observed with GMS over the radar site. We consider that smaller-scale convective clouds are directly related to the rainfall, and these are much smaller than the spatial resolution of the GMS data shown in Figure 6.1(a) which is 1° × 1° (~ 100 km × 100 km).

6.3 Wind reversal observed with the BLR

Figure 6.2 shows monthly averaged diurnal variations (left panels) and monthly averaged profiles (right panels) of the horizontal winds observed with the BLR (height $\geq$ 400 m) and the surface winds observed with the anemometer in November (upper panels) and December (lower panels). The diurnal variation indicates differences from the monthly averaged profile. In November, meridional components were stronger than zonal components below 1.6 km, while easterly winds were observed above 1.3 km. On the other hand, in December westerly winds were observed in the whole observational height range ($\leq$ 3 km). Northerly and southerly components were strong in daytime and night-time, respectively, in the height range lower than about 1 km throughout the two months. This feature was particularly clear near the ground. This wind variation corresponds to a sea-land breeze circulation as mentioned in Section 5.1 [*Hashiguchi et al.*, 1995b].

Figure 6.3 shows the time-height cross section of daily averaged horizontal

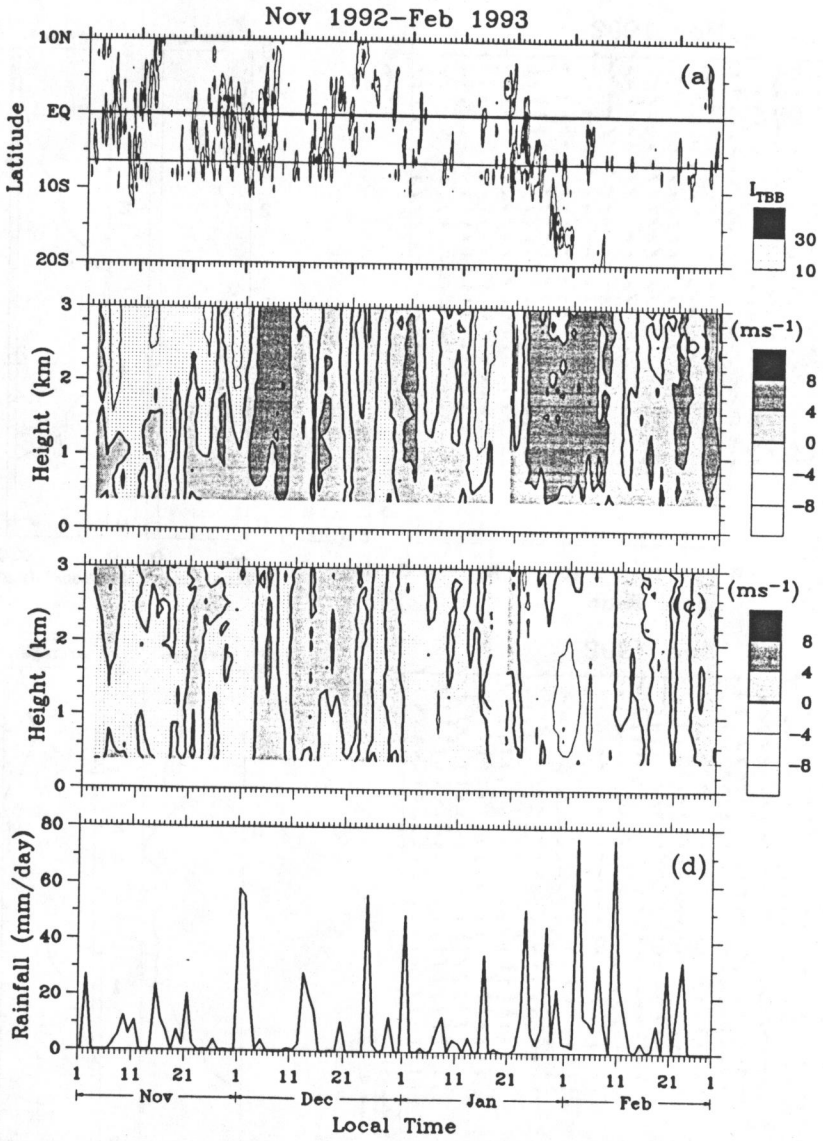

Figure 6.1: (a) Time-latitude cross section of the T_{BB} index (I_{TBB}) along a longitude of 107°E near the radar site obtained from 3-hourly infrared (IR) imageries of geostationary meteorological satellite (GMS) during TOGA COARE IOP (November 1992–February 1993). (b) and (c) show time-height cross sections of daily averaged westerly and southerly winds observed with the BLR, respectively. (d) shows time variation of rainfall observed with a rain gauge at the radar site. The thin horizontal line in (a) indicates the latitude of the radar site (6.4°S).

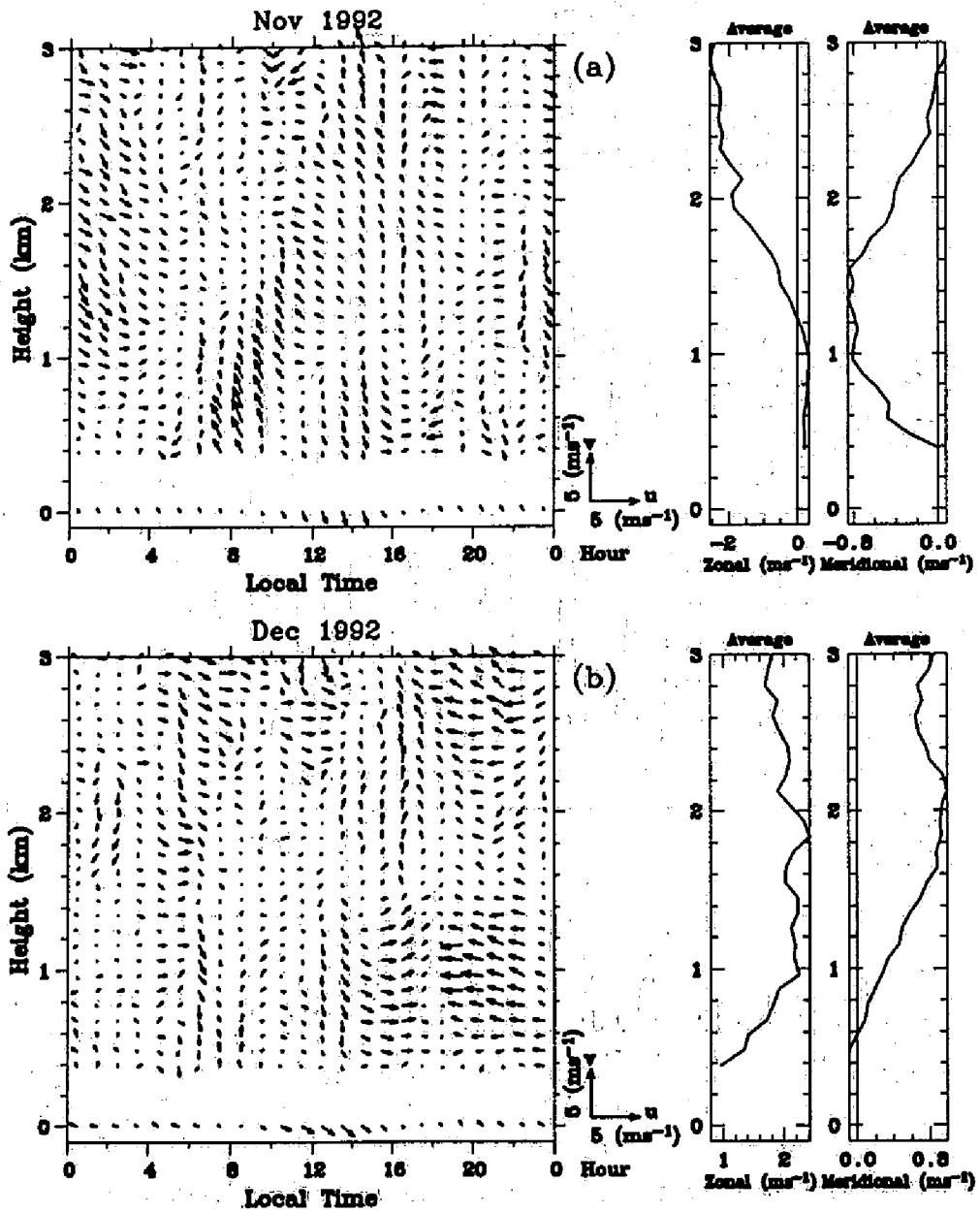

Figure 6.2: Height profiles of monthly averaged horizontal winds (four right panels) and variations of monthly averages of the diurnal wind fields (left panels) observed with the BLR in (a) November and (b) December 1992. Vectors are directed upward for a northward (southerly) component, and towards the right for a eastward (westerly) component. Surface winds observed with an anemometer are also indicated.

winds observed with the BLR and the anemometer during 2 November–31 December 1992. Small scale wind variations, such as the sea-land breeze circulation, are canceled in this figure. The wind direction was drastically reversed from easterly to westerly during these two months. In November (except on the dates 2 and 25) easterly winds were observed above 2 km, with strong easterly winds appearing at periods of 5–8 days. At the beginning of December the reversal of wind direction from easterly to westerly in the atmospheric boundary layer started earlier than in the free atmosphere. In December, strong westerly winds appeared periodically every 5–8 days. While easterly winds occasionally appeared in December, westerly winds were rarely seen above 2 km in November. Although winds at the ground were usually weak, relatively strong westerly winds were observed above the ground during 3–8 December.

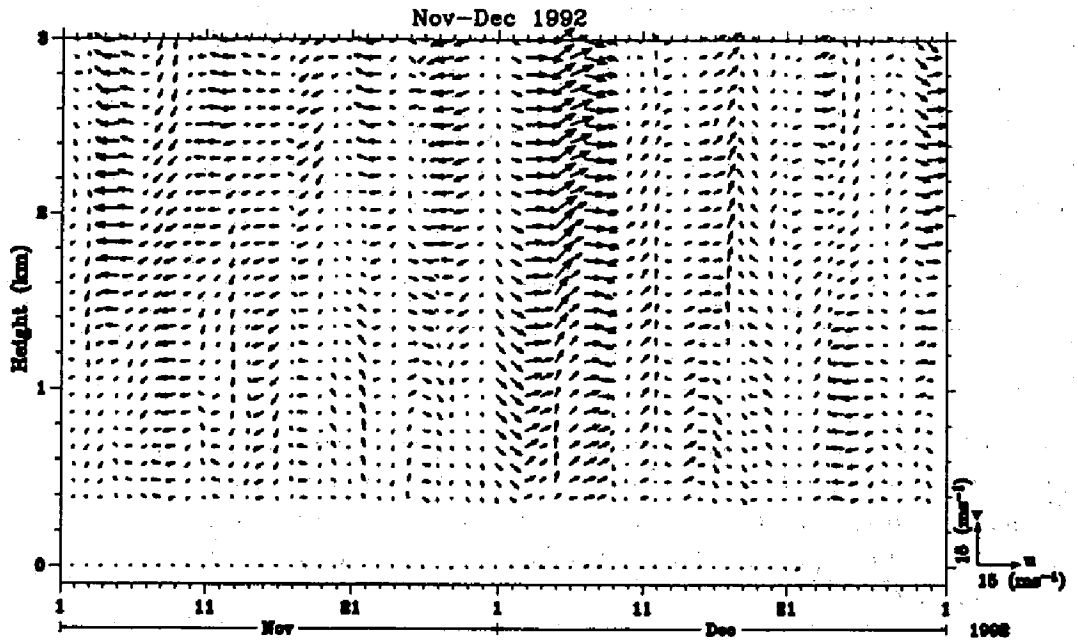

Figure 6.3: Time-height cross section of daily averaged horizontal winds observed with the BLR for two months from 2 November to 31 December 1992. Vectors are directed upward for a northward (southerly) component, and towards the right for a eastward (westerly) component. Surface winds observed with an anemometer are also indicated.

Figure 6.4 shows a time-height cross section of horizontal winds averaged every 2 hours during 28 November–3 December when the drastic change from easterly to westerly was observed. We confirm that the wind reversal occurred

during a rather short period. The dominant wind direction was easterly above 1.5 km altitude during 28–29 November, and was westerly throughout the 0.4–3 km height range during 2–3 December. However, the dominant wind direction was not so clear during 30 November–1 December.

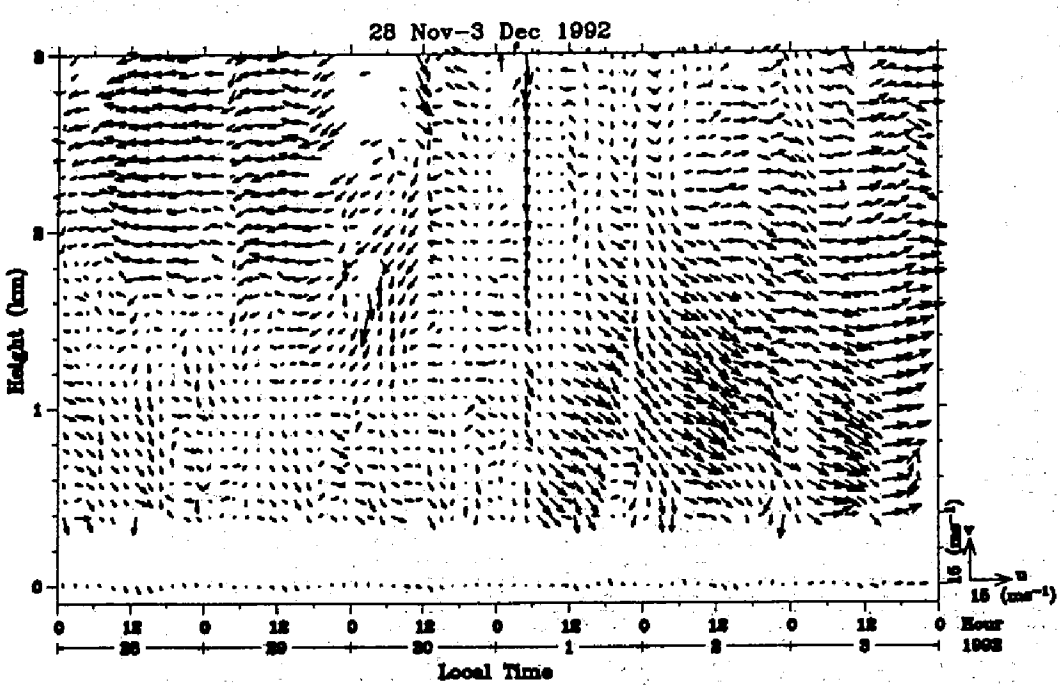

Figure 6.4: Time-height cross section of horizontal winds averaged every 2 hours during 28 November–3 December 1992. Vectors are directed upward for a northward (southerly) component, and towards the right for a eastward (westerly) component. Surface winds observed with an anemometer are also indicated.

Figure 6.5(a) shows a time-height cross section of the vertical Doppler velocity observed with the BLR in the same period as Figure 6.4. During precipitation the vertical velocity corresponds to the fall speed of precipitation particles. Rainfall observed on 28 November and 1–3 December is shown in Figure 6.5(b). In particular, strong rainfall exceeding 30 mm hour^{-1} was observed four times during the night of 1–2 December. It is noted, however, that even in such rainy weather the horizontal winds can be observed correctly with the BLR because the horizontal motion of precipitation particles follows the surrounding atmosphere almost perfectly. Westerly winds became strong below 1.5 km height during the rainfall as mentioned above, and winds were weak during the no rainfall period of

21–24 LT on 1 December (see Figure 6.4). Although no rainfall was observed on the ground on 29 and 30 November, large downward velocities observed with the BLR suggests precipitation above 0.4 km height. We consider that the BLR is more sensitive to the precipitation than the rain gauge because the BLR detects precipitation in a rather broad area (10^3–10^5 m^2) defined by the beam width ($\sim$ 7.6°) whereas the rain gauge detects precipitation in a much smaller area ($< 10^{-1}$ m^2). It is suggested that cloud activity was high in this period, and in particular it was very high in the beginning of December.

6.4 Satellite observations of cloud clusters

We used the 3-hourly GMS IR data to examine cloud distributions over Indonesia. Figure 6.6(b) shows the time-longitude cross section of I_{TBB} at 6°S latitude near the radar site during 1 November–31 December between 80°E and 160°W. Westward-moving cloud clusters were found with horizontal scales $\sim 10^2$ km and with time scales of 1–2 days. They were involved in an eastward-moving super cluster with a horizontal scale $\sim 10^3$ km as reported originally by *Nakazawa* [1988]. The phase speed of the super cluster in this case was about 4 m s^{-1}, while *Nakazawa* reported a speed of 10–15 m s^{-1}.

We found from Figure 6.6(b) that the convection center (the most active super cluster observed here) appeared on the western side of the radar site in November and passed by the radar site at the beginning of December. Such eastward movement of the convection center is a climatological feature of this season [*cf. Sumi*, 1986]. Another super cluster was generated on the western side of the radar site on or around 15 December. Figure 6.6(a) shows zonal winds averaged in the height range of 2–3 km every 12 hours observed with the BLR. When the center of the cloud clusters was located on the western or eastern sides of the radar site, the wind direction tended to become easterly or westerly, respectively. Furthermore when the cloud clusters were over the radar site, the BLR wind tended to become weak.

Figure 6.7 shows the 850 and 700 hPa (corresponding to approximately 1.5 and 3.2 km height, respectively) wind fields obtained from GANAL and the horizontal distribution of I_{TBB} near the radar site during 28 November–4 December 1992. GANAL winds near the radar site (cross symbol in Figure 6.7) are reasonably consistent with BLR daily mean winds shown in Figure 6.3; easterly winds changed to westerly winds in the beginning of December. However, the GANAL winds are somewhat stronger than the BLR winds. This may be due to the differences of temporal and spatial resolutions, and should be investigated in detail in the future.

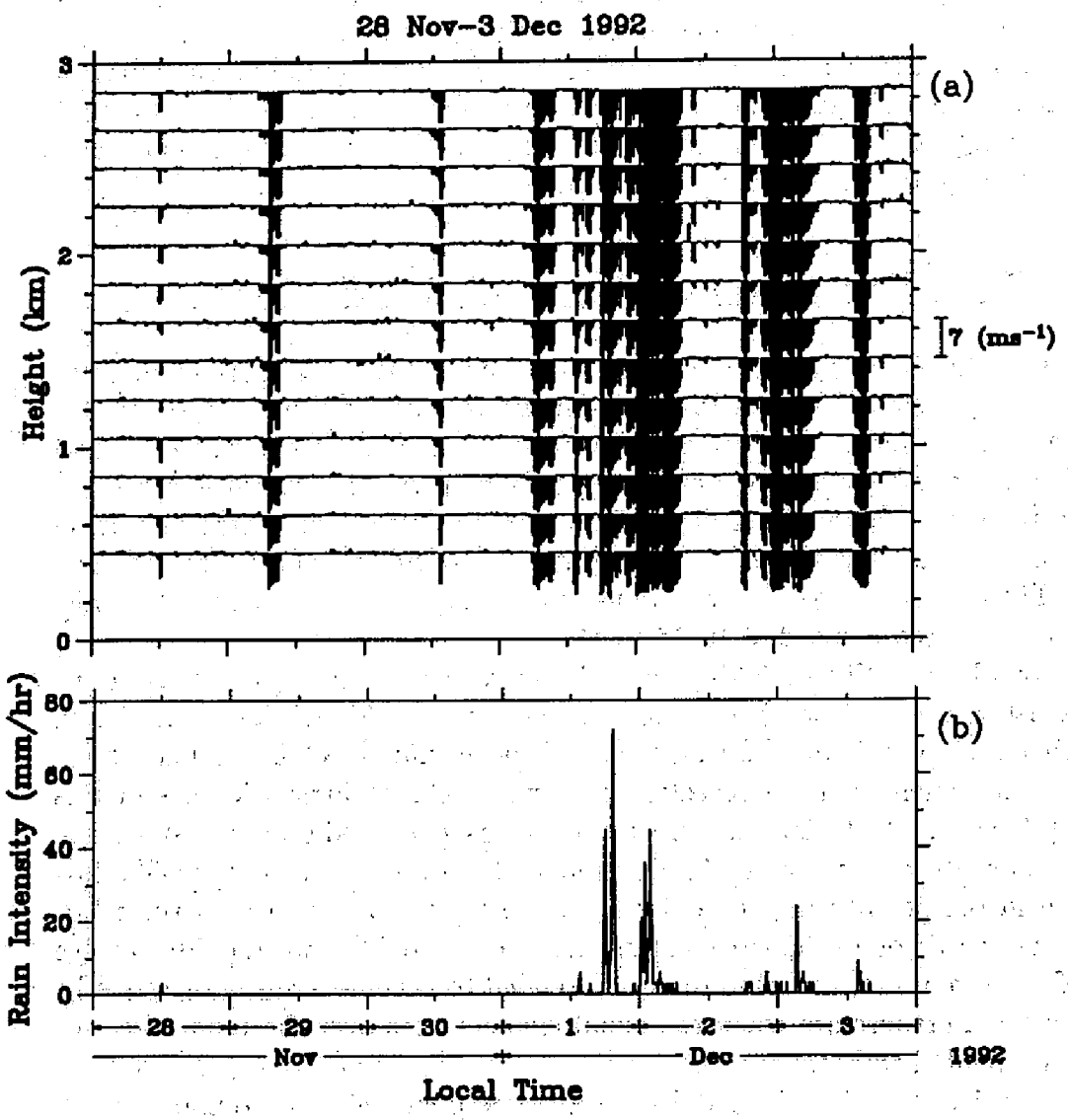

Figure 6.5: (a) Time-height cross section of the vertical atmospheric (or precipitation) motion (every 20 min) observed with the BLR and (b) time variation of the rainfall (every 10 min) obtained with a rain gauge at the radar site during 28 November–3 December 1992. The spacing of horizontal lines in (a) indicates a velocity of 7 m s^{-1}.

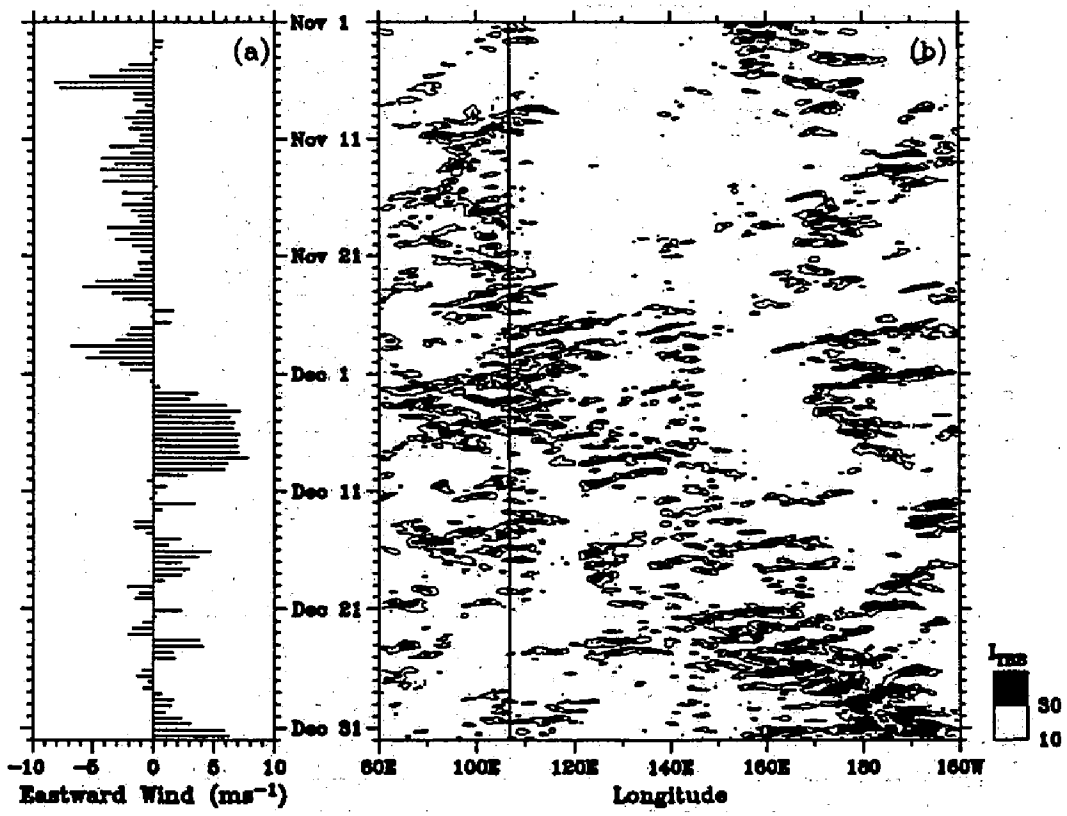

Figure 6.6: (a) Zonal winds averaged over the height range of 2–3 km every 12 hours observed with the BLR and (b) time-longitude cross section of the T_{BB} index (I_{TBB}) along the 6°S latitude near the radar site obtained from the 3-hourly GMS IR data during 1 November–31 December 1992. The vertical line in (b) indicates the longitude of the radar site (106.7°E).

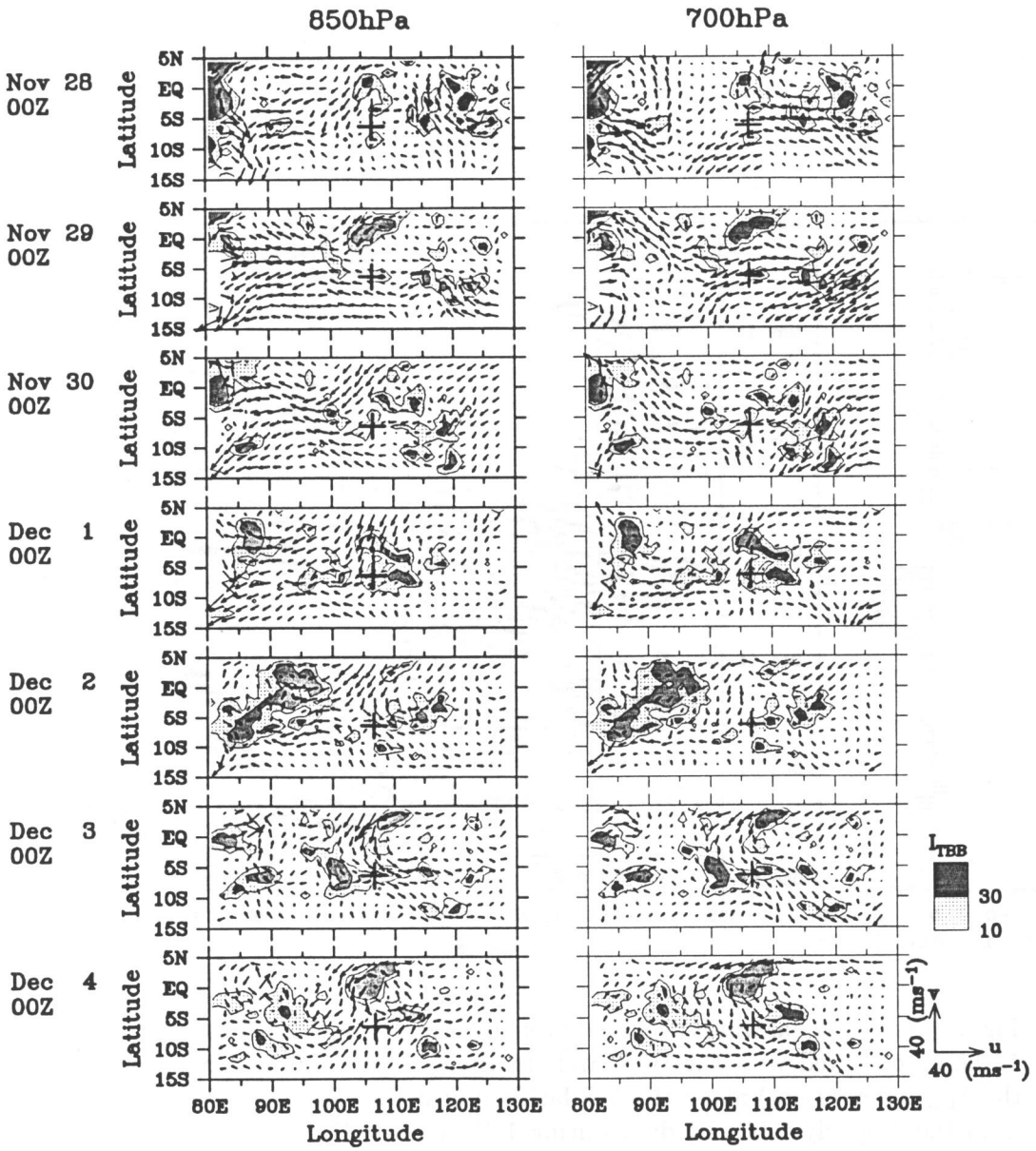

Figure 6.7: 850 (left panels) and 700 (right panels) hPa wind fields obtained from the global objective analysis (vector plot) and horizontal distribution of the T_{BB} index (I_{TBB}) (contour plot) during 28 November–4 December 1992. Vectors are directed upward for a northward (southerly) component, and towards the right for a eastward (westerly) component. The cross symbol (+) in each panel indicates the radar site (6.4°S, 106.7°E).

GMS observed the cloud top levels, which were in the upper troposphere ($I_{TBB} > 30$ or $T_{BB} < 220$ K). Therefore, middle-tropospheric observations are needed to relate the GMS cloud activity data with the BLR wind variation data which were observed only in the lower troposphere. Since we have also obtained rawinsonde data at the radar site in other periods (October 1993 for the dry season and February 1994 for the rainy season; see *Tsuda et al.*, 1995), we plan to examine the relationship between the GMS and BLR data in detail using the rawinsonde data in these periods.

6.5 Discussion and concluding remarks

On the basis of the horizontal winds observed with the BLR (Section 6.3), the cloud distributions observed with GMS, and the wind fields obtained with GANAL (Section 6.4), we conclude that the convection center (a super cluster) moved eastward over Indonesia (see Figure 6.8), bringing the rainy season to this region. The Pacific Ocean trade wind (easterly) dominated only on the eastern (or dry season) side of the convection center. The Indian Ocean monsoon wind (westerly) blew toward the convection center from the western side. The strong convergence of both winds maintained the convection center. The reversal of the wind direction from easterly (in November) to westerly (in December) observed with the BLR was associated with the eastward movement of the convection center.

It must be noted that there were several super clusters generated on the western (rainy season) side of the convection center, and that the westerly wind became weak (sometimes weak easterly) just before the passage of a super cluster (see Figure 6.6). Although the interactions among monsoon variations, super cluster generation, and rainfall activity may be quite interesting, they are beyond the scope of this study as it uses data mainly from a single station. After the TOGA COARE IOP, the mean wind direction reversed from westerly to easterly in the middle of March 1993 (the end of the 1992–1993 rainy season), and then reversed again from easterly to westerly in the middle of December 1993 as shown in Figures 6.9 and 6.10.

The temporal scales of the convection center and other super clusters (all moving eastward) were about 10 days, and the interval (clear period) between two super clusters was also about 10 days. These scales are similar to those from other observational studies [*Nakazawa*, 1988; *Lau et al.*, 1989; *Nitta et al.*, 1992]. Thus, if the super clusters are organized in a wave structure, the wave period is ≤ 20 days. This period is similar to those of surface pressure disturbances found over Indonesia in December 1978–March 1979 reported by *Estoque* [1982], tropopausal

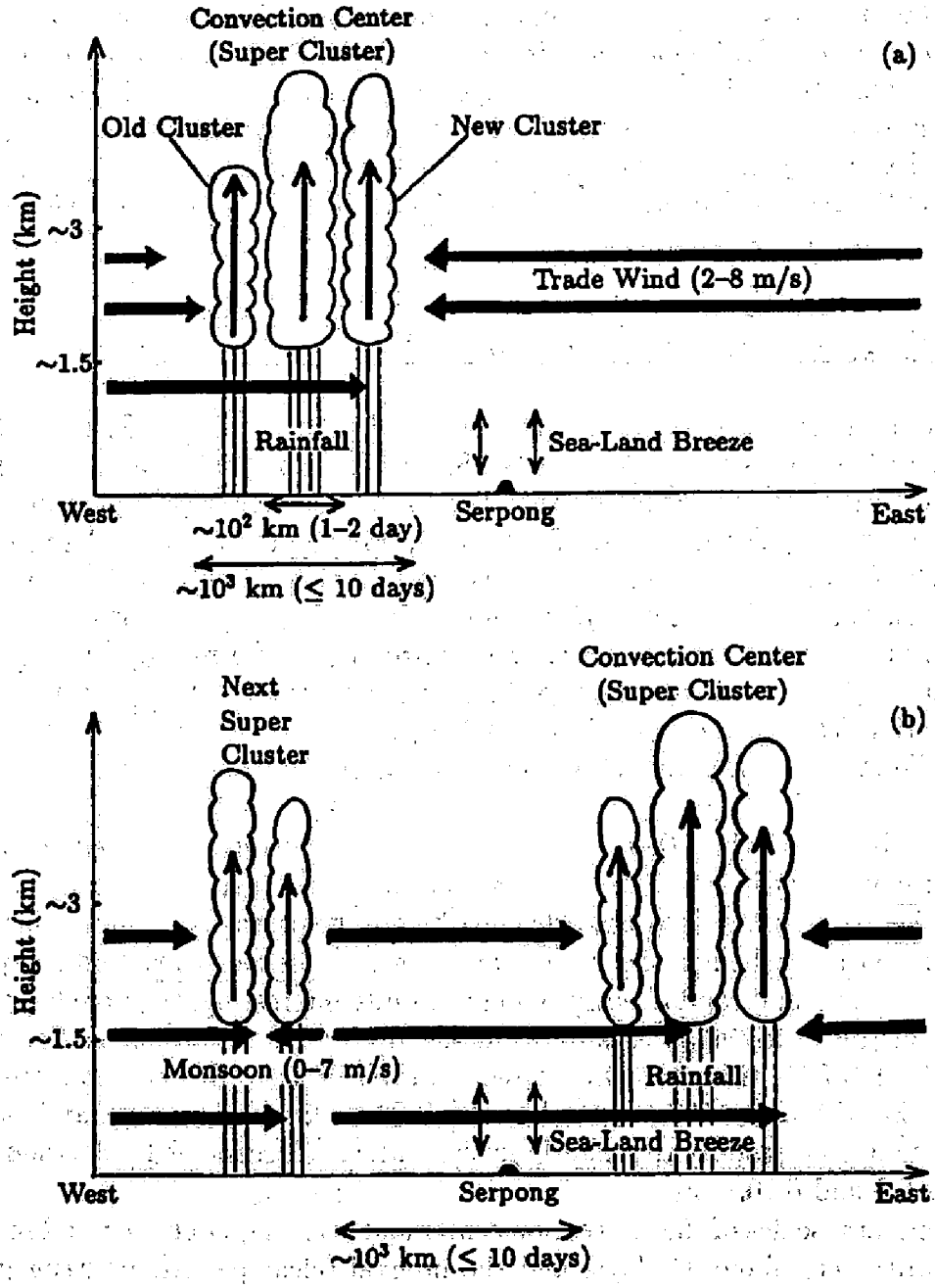

Figure 6.8: Schematic figure of the reversal of wind direction between (a) November and (b) December 1992, associated with an eastward movement of the convection center (a super cluster).

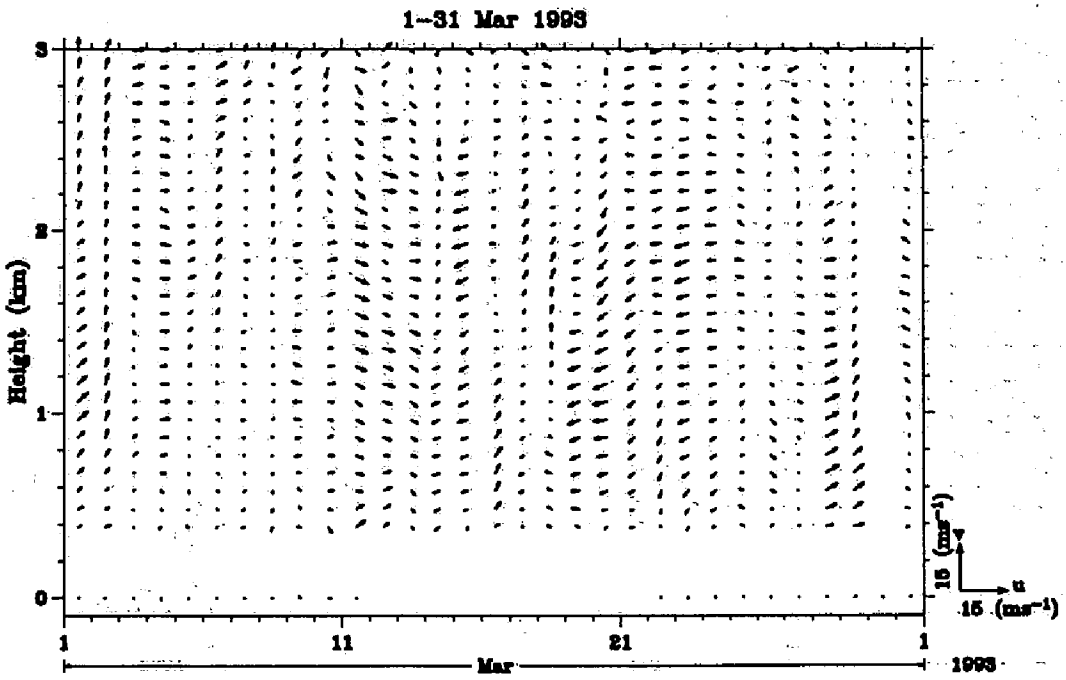

Figure 6.9: The same as Figure 6.3 except for the observation period during 1–31 March 1993.

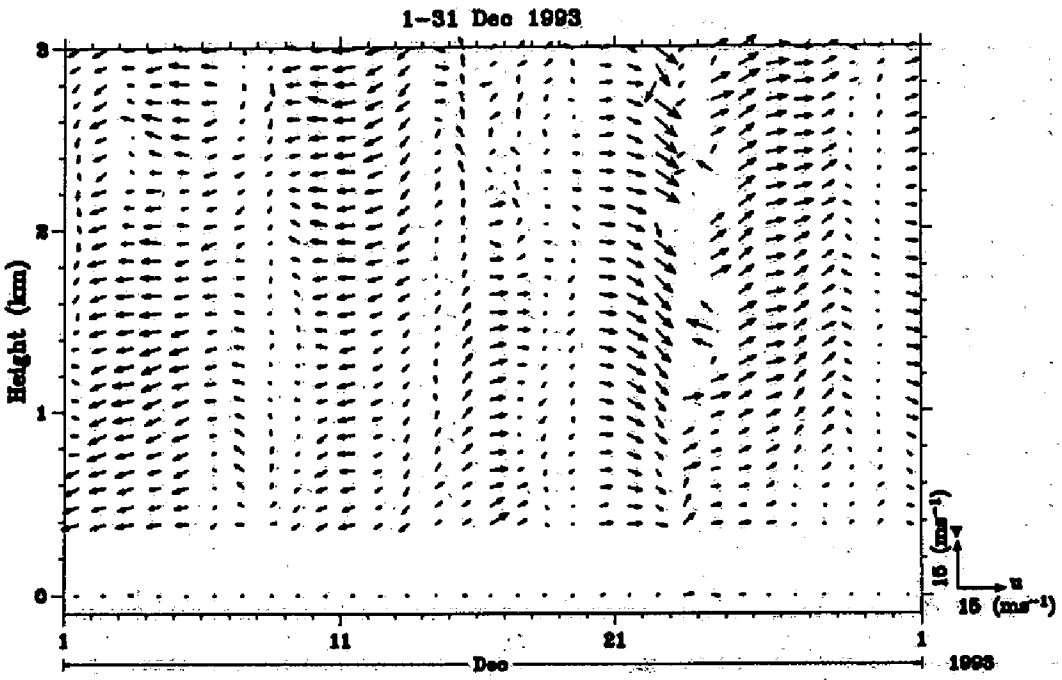

Figure 6.10: The same as Figure 6.3 except for the observation period during 1–31 December 1993.

Kelvin-wavelike disturbances found over Indonesia in February–March 1990 reported by *Tsuda et al.* [1994a], and also to lower-stratospheric Kelvin waves discovered by *Wallace and Kousky* [1968]. Using a phase speed of 4 m s^{-1} (Section 6.4) the zonal wavelength is estimated to be $\leq$ 7,000 km. In this study, we found that westerly enhancement of the wind in the western side of each super clusters appeared later in the higher altitudes (Section 6.3 and Figure 6.3), which implies a westward phase inclination.

Westward-moving cloud clusters with temporal scales of 1–2 days were found with each super cluster both in (and after) December (the westerly monsoon regime) and in November (the easterly trade wind regime) before the passage of the convection center. These temporal scales were somewhat smaller than those of the mixed Rossby-gravity wavelike disturbances (3–5 days) that were mainly over the equatorial Pacific Ocean during June–August [see, e.g., *Takayabu and Nitta*, 1993]. In this study, we found that wind variations associated with the cloud clusters in the easterly regime (or in dry season) were relatively weak in the PBL (see Section 6.3 and Figure 6.3).

In summary, the BLR observed not only wind variations correlated with the cloud cluster and super clusters, but also several differences in the characteristics of the easterly and westerly regimes (or the dry and rainy seasons). We intend to study these differences in detail based on much more intensive observations which were conducted in October 1993 (dry season) and in February 1994 (rainy season) with rawinsondes and radiation sensors as well as the BLR [*cf. Tsuda et al.*, 1995] as mentioned a part of their investigations in Chapter 5.

Chapter 7

Frequency spectra of wind velocity fluctuations

Quantitative information on the energy transport and conversion processes in the atmosphere is given by the power spectra of wind velocity fluctuations, which have become available with the development of radar profiling techniques from the troposphere to the lower thermosphere [see, e.g., *Balsley and Carter*, 1982; *Larsen et al.*, 1982; *Nakamura et al.*, 1993a]. These spectra have suggested that kinetic energy is generated in the troposphere and is transported upward mainly by various types of propagating waves. A major source of these waves is anticipated to be in tropical active convections [*Tsuda et al.*, 1994a, b, c]. Nevertheless, the bottom of the atmosphere called the PBL, in which tropospheric convections are generated, has not yet been examined closely, for quantitative information on the kinetic energy generation.

In this chapter, we present a preliminary but quantitative result concerning the horizontal wind velocity spectra for a rather broad frequency band, based on our PBL observations with the BLR. In the following sections, the spectral analysis procedure for the BLR data is first described. Frequency power spectra of wind velocity fluctuations observed with the BLR are presented in Section 7.2. In Section 7.3 we discuss kinetic energy generation based on the observational results and summarize the conclusions.

7.1 Spectral analysis techniques for the BLR data

Since the BLR can provide temporally and vertically continuous wind velocity data, spectral analysis can be applied with respect to frequency or vertical

wavenumber. In the present work, we have calculated one-dimensional frequency spectra of zonal and meridional wind fluctuations observed with the BLR. Power spectral densities are often calculated from the squared values of Fourier coefficients obtained through the fast Fourier transformation (FFT) of time series. However, if the observed data series has missing samples, FFT cannot be directly applied to the data. Avoiding this difficulty, we applied the method reported by *Blackman and Tukey* [1959] to the observed data series with some missing data points in order to calculate the power spectral density. We briefly describe the spectrum calculation procedure employed in this work, following the principle of *Blackman and Tukey*.

From a time series of a certain physical quantity, an auto-correlation function (ACF) is calculated with a maximum lag that must be smaller than the number of the total samples of the series. The chosen maximum lag must be small enough for there to be no missing ACF values. After multiplying the ACF with a lag window (Hanning window), the power spectral density is calculated using a FFT. For computing the frequency spectrum, the data are prewhitened before calculating ACF to make reliable estimates. The original data series $\{x_i\}$ becomes a prewhitened data series $\{\tilde{x}_i\}$ with the use of the formula

$$\tilde{x}_i = x_i - \beta x_{i-1} \tag{7.1}$$

where β is the degree of prewhitening, which was taken as 0.95. After the Fourier transformation the spectrum is compensated for prewhitening by recoloring. Finally the spectrum $\{P_i\}$ is smoothed by the formula

$$\tilde{P}_i = \frac{P_{i-3} + 6P_{i-2} + 15P_{i-1} + 20P_i + 15P_{i+1} + 6P_{i+2} + P_{i+3}}{64} \tag{7.2}$$

as suggested by *Endlich et al.* [1969].

As described in Chapter 3, the BLR detects the mean radial Doppler velocity inside a sampling volume given by the beam width of 7.6° for one beam at a range resolution of 100 m. The vertical velocity determined by using one vertical beam corresponds to the mean value over a volume of roughly 130 m wide and 100 m thick at 1 km height. Since the zonal and meridional velocities are determined by using vertical and 15°-oblique beams, these velocity components are the mean values over a volume of about 400 m wide and 100 m thick at 1 km height under an assumption that the wind fields are homogeneous in this volume. The BLR can provide time series of wind velocities with a high time resolution of about 1 min. However, since the noise floor of a frequency spectrum calculated from this time series is raised, probably due to inhomogeneity of the wind fields (particularly in vertical velocities) between vertical and oblique beams, a reliable power spectral

density can barely be obtained at frequencies higher than 1 hour^{-1}. Therefore we have calculated frequency spectra from time series of wind velocities averaged every one hour for each range gate (height resolution of 100 m) with a maximum lag of 256 data points (corresponding to a period of $\sim$ 11 days), except for cases when more than 50% of the data were missing in each time series obtained for three months.

7.2 Observational results

Since the climatology of the Java Island is characterized by an annual cycle of rainy and dry seasons as mentioned in Chapter 6, we compared frequency power spectra between the dry and rainy seasons. Figure 7.1 shows frequency power spectral densities calculated for zonal and meridional wind velocities observed with the BLR at the height range of 0.4–2.4 km and with a standard anemometer at 10 m height above the ground during August–October 1993 (dry season) and December 1993–February 1994 (rainy season). The spectra were averaged over height regions of 0.6 km thick.

The spectral slope obtained from the BLR data is fairly similar between the zonal and meridional components, and the dry and rainy seasons, showing a logarithmic slope of -1 at frequencies at least higher than 1 day^{-1}. A slope of $-5/3$ has been reported in observations in the extra-tropical lower and middle atmosphere in earlier studies however [e.g., *Balsley and Carter*, 1982; *Larsen et al.*, 1982; *Gage et al.*, 1986; *Tsuda et al.*, 1994b]. The slope for the meridional component in the dry season is gentler than -1 at frequencies less than 1 day^{-1}. On the other hand, the slopes obtained from the anemometer data for all the cases are close to $-5/3$ at the higher frequency range (approximately higher than the semidiurnal component). As shown in Figure 7.2, the spectral slope obtained by the BLR observations in Shigaraki, Japan was closer to $-5/3$ rather than -1, which is consistent with results obtained from the MU radar data for a 2.5–3.4 km height range at the same place for about 100 hours during 15–19 June 1992. Therefore, we do not consider that those differences of slope values are due to any technical problems in the BLR wind measurements.

A common feature in all cases in Figure 7.1 is that the spectral amplitudes above 0.4 km are about 10 times as large as those at the ground and increase slightly with height (note that the values at 1.1–1.7 km and 1.8–2.4 km heights are multiplied by a factor of 10 and 10^2, respectively). In order to examine the relative dominance of various components, we present energy-content contour plots of the spectral amplitudes obtained for each sampled height (see Figure 7.3). We found the following features concerning vertical and seasonal variabilities of

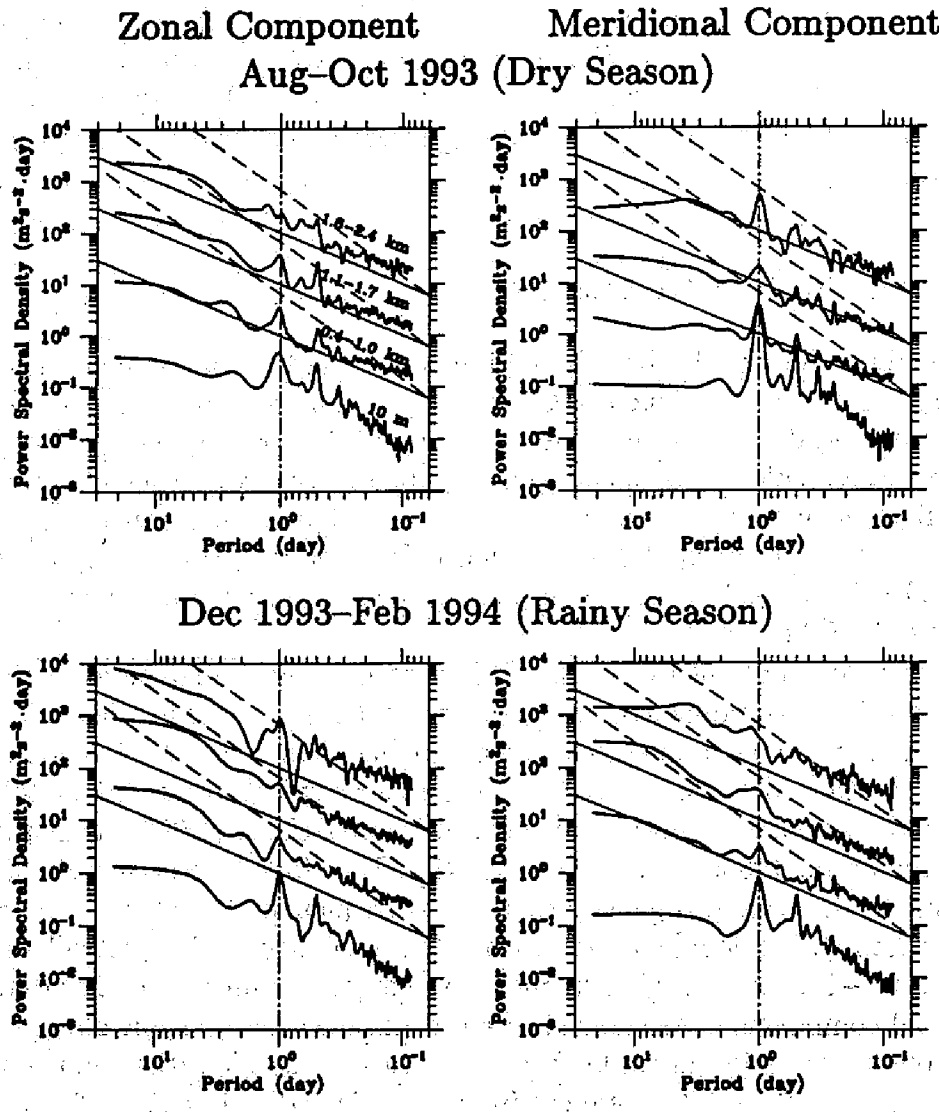

Figure 7.1: Frequency power spectral densities for (left panels) zonal and (right panels) meridional wind velocities observed with the BLR (0.4–2.4 km) and a standard anemometer (10 m) in Serpong, Indonesia during (upper panels) August–October 1993 and (lower panels) December 1993–February 1994. Spectra at 1.1–1.7 km and 1.8–2.4 km heights are multiplied by a factor of 10 and 10^2, respectively, to separate them on the graph. The axes are correct for the spectra at 10 m and 0.4–1.0 km heights. Slant solid and dashed lines indicate the logarithmic spectral slopes of -1 and $-5/3$, respectively. Vertical dotted-dashed lines indicate the period of one day.

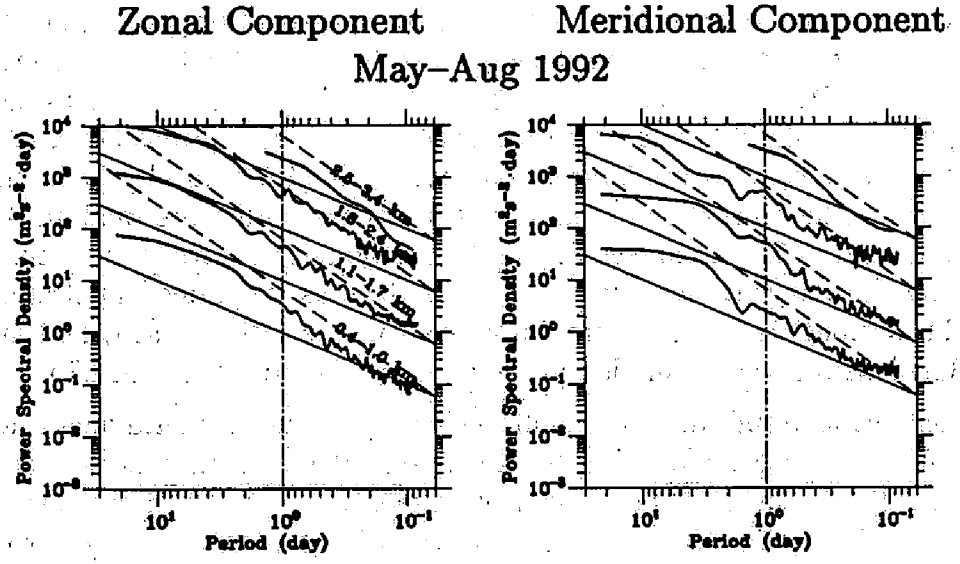

Figure 7.2: The same as Figure 7.1 except for the location in Shigaraki, Japan and observation period during May–August 1992. Frequency power spectral densities, multiplied by a factor of 10^3, for wind velocities observed with the MU radar (2.5–3.4 km) during 15–19 June 1992 are also indicated. Surface wind data were not obtained in Shigaraki in this period.

these spectral amplitudes:

i) The spectral amplitudes in the rainy season are about two times or more larger than those in the dry season in the almost entire observed height and frequency ranges.

ii) In the all height ranges, the diurnal component is dominant. This component is strongest for the meridional component in the dry season, both near the ground and at heights above about 2 km. This result is consistent with features noted in Chapter 5: striking diurnal variations of the top of the PBL which extends up to 3 km or higher on clear days. The predominance for the meridional wind may be explained by a sea-land breeze circulation near the coastline which runs in the west-east direction. We have confirmed that the meridional winds have a reversal at an altitude of around 1.5 km between the sea-land breeze near the surface and its counterbalancing flow in the upper levels. A semidiurnal component is also seen clearly in the dry season. The diurnal and semidiurnal peaks are both quite weak in the data obtained in Shigaraki (see Figure 7.2), although we have found similar PBL-top diurnal variations on a few clear days as mentioned in Section 3.2. In Serpong these peaks are found even in the rainy season, and are correlated with severe rainfalls concentrated in afternoons (12–24 LT).

iii) The zonal wind amplitudes are significantly larger than the meridional wind amplitudes at periods of around 10 days (particularly in the rainy season). They are consistent with the activity of eastward moving super cloud clusters (see Chapter 6) which have Kelvin-wavelike structures and behavior (particularly near the tropopause; *cf. Tsuda et al.*, 1994b, 1995).

iv) Above 2 km height the meridional wind amplitudes are larger than the zonal wind amplitudes at periods of around 4 days in the rainy season. We have noted in Chapter 6 that rainy season cloud activity and rainfall have a periodicity of 3–5 days. It seems that the 4 day component is associated with such active convective clouds which several studies have reported as possibly having mixed Rossby-gravity wavelike structures and westward moving behavior [e.g., *Takayabu and Nitta*, 1993].

7.3 Discussion and concluding remarks

Frequency power spectra of horizontal wind velocities in a broad frequency band of approximately 1 hour–1 month have been presented in this chapter. We have found that the spectral slope is approximately -1 in a period band from

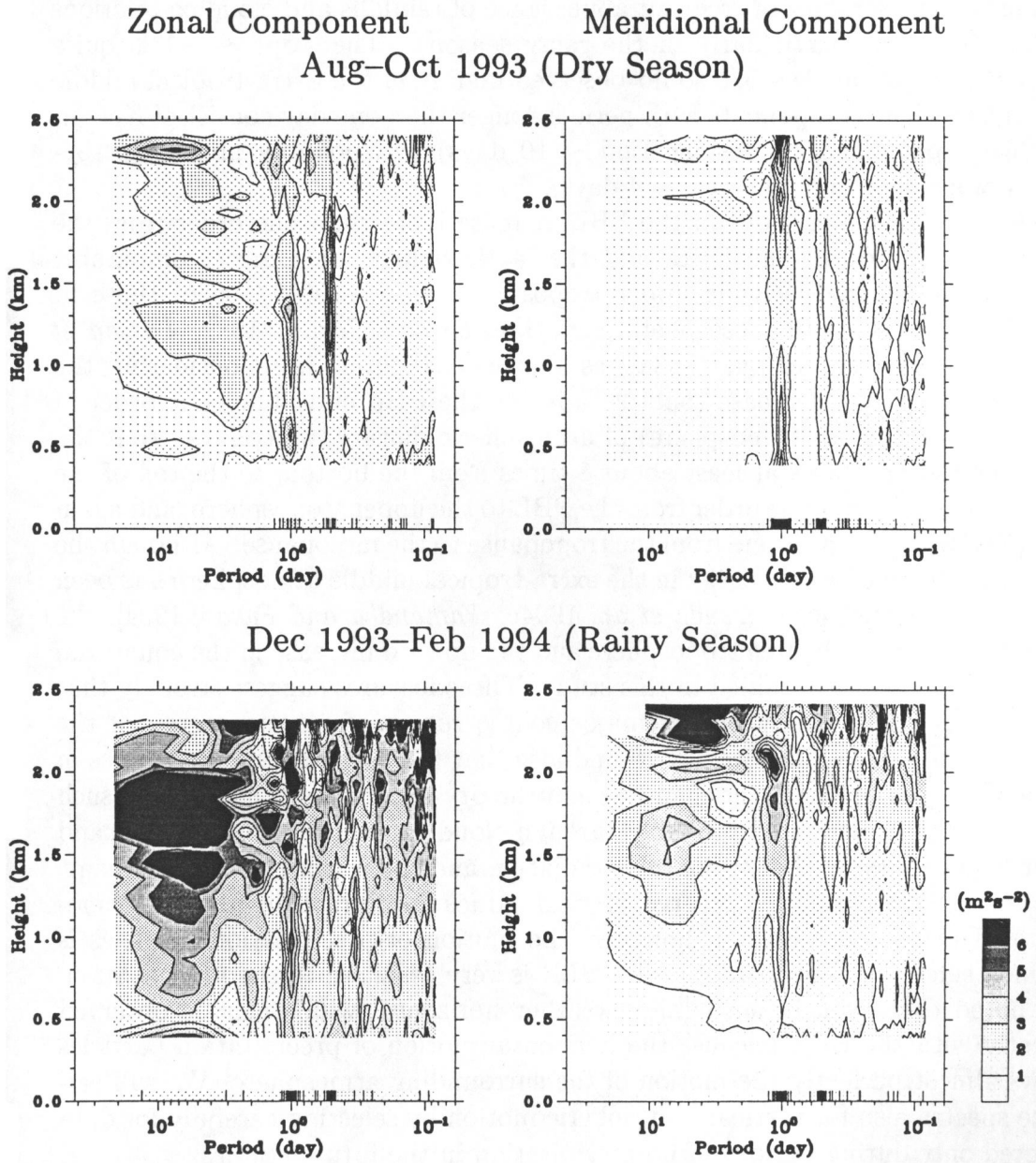

Figure 7.3: The same as Figure 7.1 except for an energy-content form. The values at 10 m height are multiplied by a factor of 10.

a few hours to a few days, and that there exists striking diurnal oscillations corresponding to PBL-top variations, sea-land breeze circulations (both on clear days in the dry season), or frequent appearance of rainfalls and cloud convections in the afternoon (particularly in the rainy season). The slope ~ -1 is quite different from values $\sim -5/3$ so far observed mainly in the extra-tropical middle atmosphere. The components with periods longer than one day consist of Kelvin-wavelike super cloud clusters (period $\sim$ 10 days) and possibly mixed Rossby-gravity wavelike cloud clusters ($\sim$ 4 days).

The spectral amplitudes in the PBL increase more than one order from the bottom to the top of the PBL, and the latter values are almost comparable to values in the mid-latitude upper troposphere and 1/300–1/100 of those in the mid-latitude upper mesosphere [e.g., *Balsley and Carter*, 1982; *Larsen et al.*, 1982; *Nakamura et al.*, 1993a], as shown in Figure 7.4. Considering the upward exponential decrease (only 20% inside the PBL and about one order of magnitude in the free troposphere) of atmospheric density, we consider that the kinetic energy increases at least about 8 times from the bottom to the top of the PBL, decreases about one order from the PBL to the upper troposphere, and again decreases two or three orders from the tropopause to the mesopause. Although the upward decrease of wave energy in the extra-tropical middle atmosphere has been previously reported [e.g., *Tsuda et al.*, 1994c; *Yamanaka and Fukao*, 1994], the upward decrease in the free troposphere and the upward increase in the equatorial PBL are new results obtained in this study. These features suggest strongly that the equatorial PBL must be the major source region of kinetic energy of the earth's atmosphere. Since we have found also that the power spectral densities in the rainy season are stronger than those in the dry season, we consider that such kinetic energy is generated probably through cloud convection from sensible and latent heat inputs by the strong solar radiation and the warm equatorial ocean.

The BLR can directly observe vertical atmospheric motion in clear atmosphere. During precipitation, however, the motion of precipitation particles is obtained since the *L*-band radio wave BLR is very sensitive to the precipitation. It is noted that even in such rainy weather horizontal winds can be observed correctly with the BLR because the horizontal motion of precipitation particles follows almost perfectly the motion of the surrounding atmosphere. We will calculate spectra also for vertical atmospheric motion by selecting carefully for data collected only during periods of no precipitation in the future studies.

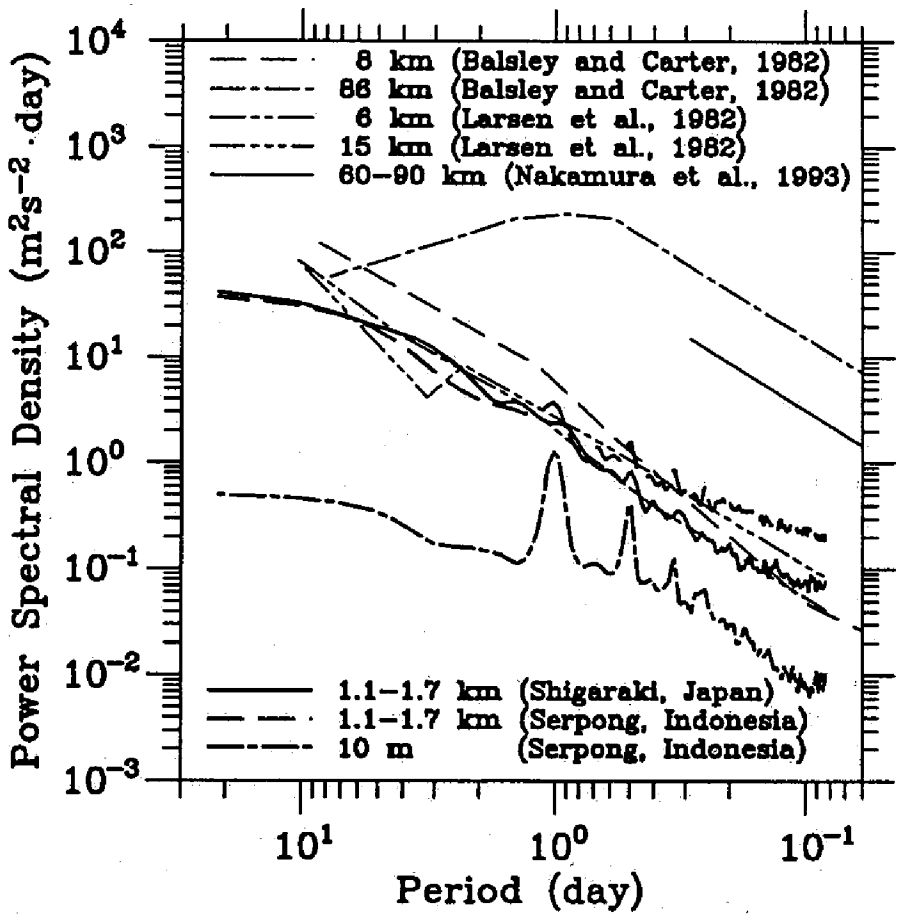

Figure 7.4: Comparison between the horizontal wind frequency spectra obtained in this study (thick curves) and earlier (extra-tropical lower- and middle-atmospheric) studies (thin curves) [*Balsley and Carter*, 1982; *Larsen et al.*, 1982; *Nakamura et al.*, 1993a].

Chapter 8

Summary and conclusions

This thesis was concerned with the development of the *L*-band boundary layer radar (BLR) and the continuous observations with using the BLR in the planetary boundary layer (PBL) in Shigaraki, Japan and in Serpong in the Indonesian maritime continent. The BLR has been successfully operated in Shigaraki throughout four months during May–August 1992 and in Serpong since November 1992.

In Chapter 1, general introduction was presented to show the characteristics of the PBL and the observation techniques in the PBL. Radar techniques to observe wind velocities were also shown in this chapter.

In Chapter 2, system requirements of the BLR were first discussed. RASS (Radio Acoustic Sounding System) techniques using the BLR were also described. We showed in detail the hardware and software systems of the BLR designed based on the above discussions. The method to estimate the spectral parameters (the echo power, the mean Doppler shift, and the spectral width) from the Doppler power spectrum observed with the BLR was also described.

In Chapter 3, we presented the simultaneous observational results of the BLR and the MU (Middle and Upper atmosphere) radar conducted on 6 January 1992. We discussed the performance of the BLR in comparison with the results observed with the MU radar. From the continuous four-month observations with the BLR in Shigaraki, remarkable diurnal variations of the echo intensity were observed, and an enhanced echo layer was identified with the top of the PBL by simultaneous radiosonde observations. Observed features of the diurnal variation of the PBL were in general quite consistent to those speculated or predicted numerically in earlier studies. The BLR clearly revealed the large vertical velocity variations and intense turbulence in the PBL. We found that the remarkable diurnal variations of the PBL appeared only for a few days each month. In almost all the remarkable cases we found that the dominant larger-scale wind in the free atmosphere was southward.

In Chapter 4, we first described the outline of the observation project in equatorial Indonesia, and reviewed rawinsonde observation results in Bandung, Indonesia during November 1992–April 1993. The performance of the BLR with respect to the observation height range and the wind measurement reliability was also examined on the basis of simultaneous meteorological observations.

In Chapter 5, we found that there were two types of strong echo structures appearing systematically in the equatorial PBL with diurnal variations on clear days. The first type was the striking appearance of a strong echo layer ascending from below 300 m (in the morning) to above 3–5 km (in the afternoon), which was identified with a diurnal variation of the top of the mixing PBL, and was similar to observational results, described in Chapter 3, in Shigaraki. The thickness of the PBL was however higher in the Indonesian equatorial region than in mid-latitudes. Another type was layered echoes appearing at 2–3 km heights from night-time to morning, which seem to be coincident with humidity gaps.

In Chapter 6, we found by using the data from BLR and GMS (Geostationary Meteorological Satellite) observations, and GANAL (Global objective analysis) that there existed a reversal of the dominant wind direction from easterly Pacific Ocean trade wind to westerly Indian Ocean monsoon wind between the western and eastern sides of the eastward moving convection center (a super cluster). The BLR provided detailed measurements of wind variations in time and height, and revealed the fact that the wind reversal occurred during a rather short period and the lower-tropospheric wind disturbances associated with cloud clusters in the easterly trade-wind regime (or in the dry season) were relatively weaker than those in the westerly monsoon regime (or in the rainy season).

In Chapter 7, frequency power spectra were analyzed from zonal and meridional wind velocities observed continuously in a height range below 2.5 km with the BLR. We found that (i) the spectral slope in a period range from a few hours to a few days is approximately -1 in Serpong in contrast with approximately $-5/3$ in Shigaraki; (ii) the power spectral densities in the rainy season are at least about two times larger than those in the dry season; (iii) the diurnal component is dominant both in dry and rainy seasons; (iv) components with periods of about 4 and 10 days are probably associated with mixed Rossby-gravity wavelike cloud clusters and Kelvin wavelike super cloud clusters, respectively, and (v) the power spectral amplitudes increase at least one order of magnitude from the bottom to the top of equatorial PBL, and the values at the top of the PBL are almost comparable to those in the upper troposphere over mid-latitudes. The last feature suggests strongly that the equatorial PBL is a major source of kinetic energy of the earth's atmosphere.

We have not yet utilized the full capabilities of the BLR in this thesis. For

example, variations of vertical atmospheric wind and turbulence intensity in the lower troposphere including the PBL, and the top of the PBL can be observed with using the BLR every minute, which are all impossible by classical observation techniques. We are going to analyze these high-resolution data in detail in the future studies. Furthermore, we should develop more inexpensive and more transportable (compact and light weight) radar system to make BLR systems popular as wind measurement system in the lower troposphere. We believe that these advanced studies must contribute to elucidation of many unknown important roles of the PBL (particularly in equatorial region) in the earth's environmental problems.

References

Allan, R. J., Australasia, in *Teleconnections Linking Worldwide Climate Anomalies: Scientific Basis and Societal Impact*, Cambridge University Press, 73–120, 1991.

Andrews, D. G., J. R. Holton, and C. B. Leovy, *Middle Atmosphere Dynamics*, Academic Press, Inc., 1987.

Angevine, W. M., A. B. White, and S. K. Avery, Boundary-layer depth and entrainment zone characterization with a boundary-layer profiler, *Bound.-Layer Meteor.*, **68**, 375–385, 1994.

Arimura, Y., Development of a transportable boundary layer radar, *Bachelor thesis, Department of electronic engineering, Kyoto University*, 23pp., 1990 (in Japanese).

Balsley, B. B. and K. S. Gage, The MST radar technique: Potential for middle atmospheric studies, *Pure Appl. Geophys.*, **118**, 452–493, 1980.

Balsley, B. B. and D. A. Carter, The spectrum of atmospheric velocity fluctuations at 8 and 86 km, *Geophys. Res. Lett.*, **9**, 465–468, 1982.

Balsley, B. B., A. C. Riddle, W. L. Ecklund, and D. A. Carter, Sea surface currents in the equatorial Pacific from VHF radar backscatter observations, *J. Atmos. Ocean. Tech.*, **14**, 530–535, 1987.

Balsley, B. B., D. A. Carter, A. C. Riddle, W. L. Ecklund, and K. S. Gage, On the potential of VHF wind profilers for studying convective processes in the tropics, *Bull. Amer. Meteor. Soc.*, **72**, 1355–1360, 1991.

Battan, L. J., *Radar Observation of the Atmosphere*, The University of Chicago Press, 88–97, 1973.

Blackman, R. B. and J. W. Tukey, *The Measurement of Power Spectra from the Point of View of Communications Engineering*, Dover, New York, 1959.

Browning, K. A. and D. Atlas, Velocity characteristics of some clear-air dot angels, *J. Atmos. Sci.*, **23**, 592–604, 1966.

Chang, C.-P. and J.-M. Chen, A statistical study of winter monsoon cold surges over the South China Sea and the large-scale equatorial divergence, *J. Meteor. Soc. Japan*, **70**, 287–302, 1992.

Ecklund, W. L., D. A. Carter, and B. B. Balsley, A UHF wind profiler for the boundary layer: Brief description and initial results, *J. Atmos. Ocean. Tech.*, **5**, 432–441, 1988.

Ecklund, W. L., D. A. Carter, B. B. Balsley, P. E. Currier, J. L. Green, B. L. Weber, and K. S. Gage, Field tests of a lower tropospheric wind profiler, *Radio Sci.*, **25**, 899–906, 1990.

Endlich, R. M., R. C. Singleton, and J. W. Kaufman, Spectral analysis of detailed vertical wind speed profiles, *J. Atmos. Sci.*, **26**, 1030–1041, 1969.

Estoque, M. A., Large scale pressure disturbances over the Indonesian maritime continent, *J. Meteor. Soc. Japan*, **60**, 1143–1152, 1982.

Firestone, J. K. and B. A. Albrecht, The structure of the atmospheric boundary layer in the central equatorial Pacific during January and February of FGGE, *Mon. Wea. Rev.*, **114**, 2219–2231, 1986.

Friend, A. W., Theory and practice of tropospheric sounding by radar, *Proc. IEEE*, **37**, 116–138, 1949.

Fukao, S., T. Sato, T. Tsuda, S. Kato, K. Wakasugi, and T. Makihira, The MU radar with an active phased array system, 1. Antenna and power amplifiers, *Radio Sci.*, **20**, 1155–1168, 1985a.

Fukao, S., T. Tsuda, T. Sato, S. Kato, K. Wakasugi, and T. Makihira, The MU radar with an active phased array system, 2. In-house equipment, *Radio Sci.*, **20**, 1169–1176, 1985b.

Fukao, S., K. Wakasugi, T. Sato, S. Morimoto, T. Tsuda, I. Hirota, I. Kimura, and S. Kato, Direct measurement of air and precipitation particle motion by very high frequency Doppler radar, *Nature*, **316**, 712–714, 1985c.

Fukao, S., M. D. Yamanaka, T. Sato, T. Tsuda, and S. Kato, Three-dimensional air motions over the baiu front observed by a VHF-band Doppler radar: A case study, *Mon. Wea. Rev.*, **116**, 281–292, 1988.

Fukao, S., M. D. Yamanaka, H. Matsumoto, T. Sato, T. Tsuda, and S. Kato, Wind fluctuations near a cold vortex-tropopause funnel-system observed by the MU radar, *Pure Appl. Geophys.*, **130**, 463–479, 1989.

Fukao, S., M. D. Yamanaka, N. Ao, W. K. Hocking, T. Sato, M. Yamamoto, T. Nakamura, T. Tsuda, and S. Kato, Seasonal variability of vertical eddy diffusivity in the middle atmosphere, Part I: Three-year observations by the MU radar, *J. Geophys. Res.*, **99**, 18973–18987, 1994.

Fukao, S., H. Hashiguchi, M. Yamamoto, T. Tsuda, T. Sato, M. D. Yamanaka, T. Nakamura, S. Kato, T. Makihira, and K. Hamatsu, An *L*-band clear-air Doppler radar for the atmospheric boundary layer, *J. Meteor. Soc. Japan*, to be submitted, 1995.

Gage, K. S. and J. L. Green, Evidence for specular reflection from monostatic VHF radar observations of the stratosphere, *Radio Sci.*, **13**, 991–1001, 1978.

Gage, K. S., W. L. Ecklund, and B. B. Balsley, A modified Fresnel scattering model for parameterization of Fresnel returns, *Radio Sci.*, **20**, 1493–1501, 1985.

Gage, K. S., B. B. Balsley, and R. Garello, Comparisons of horizontal and vertical velocity spectra in the mesosphere, stratosphere and troposphere: observations and theory, *Geophys. Res. Lett.*, **13**, 1125–1128, 1986.

Gage, K. S., J. R. McAfee, W. G. Collins, D. Söderman, H. Böttger, A. Radford, and B. B. Balsley, A comparison of winds observed at Christmas Island using a wind-profiling Doppler radar with NMC and ECMWF analyses, *Bull. Amer. Meteor. Soc.*, **69**, 1041–1046, 1988.

Gage, K. S., Radar observations of the free atmosphere: Structure and dynamics, in *Radar in Meteorology: Battan Memorial and 40th Anniversary Radar Meteorology Conference*, edited by D. Atlas, American Meteorological Society, 534–565, 1990.

Gage, K. S., B. B. Balsley, W. L. Ecklund, D. A. Carter, and J. R. McAfee, Wind profiler-related research in the tropical Pacific, *J. Geophys. Res.*, **96**, 3209–3220, 1991a.

Gage, K. S., J. R. McAfee, D. A. Carter, W. L. Ecklund, A. C. Riddle, G. C. Reid, and B. B. Balsley, Long-term mean vertical motion over the tropical Pacific: Wind-profiling Doppler radar measurements, *Science*, **254**, 1771–1773, 1991b.

Gage, K. S., J. R. McAfee, W. L. Ecklund, D. A. Carter, C. R. Williams, P. E. Johnston, and A. C. Riddle, The Christmas Island wind profiler: A prototype VHF wind-profiling radar for the tropics, *J. Atmos. Ocean. Tech.*, **11**, 22–31, 1994.

Garratt, J. R., *The Atmospheric Boundary Layer*, 316pp., Cambridge University Press, 1992.

Gossard, E. E., Radar research on the atmospheric boundary layer, in *Radar in Meteorology: Battan Memorial and 40th Anniversary Radar Meteorology Conference*, edited by D. Atlas, American Meteorological Society, 477–527, 1990.

Hashiguchi, H., M. Yamamoto, S. Fukao, T. Tsuda, M. D. Yamanaka, T. Nakamura, T. Sato, S. Kato, T. Makihira, and K. Hamatsu, Development of a boundary layer radar, *Preprints of the International Symposium on Middle Atmosphere Science, Kyoto, 23–27 March*, 46–47, 1992.

Hashiguchi, H., M. D. Yamanaka, T. Tsuda, M. Yamamoto, T. Nakamura, T. Adachi, S. Fukao, T. Sato, and D. L. Tobing, Diurnal variations of the planetary boundary layer observed with an *L*-band clear-air Doppler radar, *Bound.-Layer Meteor.*, in press, 1995a.

Hashiguchi, H., S. Fukao, T. Tsuda, M. D. Yamanaka, D. L. Tobing, T. Sribimawati, S. W. B. Harijono, and H. Wiryosumarto, Observations of the planetary boundary layer over equatorial Indonesia with an *L*-band clear-air Doppler radar: Initial results, *Radio Sci.*, in press, 1995b.

Hashiguchi, H., S. Fukao, M. D. Yamanaka, T. Tsuda, S. W. B. Harijono, and H. Wiryosumarto, Boundary layer radar observations of the passage of the convection center over Serpong, Indonesia (6°S, 107°E) during the TOGA COARE intensive observation period, *J. Meteor. Soc. Japan*, in press, 1995c.

Hashiguchi, H., S. Fukao, M. D. Yamanaka, and T. Tsuda, Frequency spectra of wind velocity fluctuations between 1 hour and 1 month in the atmospheric boundary layer over equatorial Indonesia, *J. Geomag. Geoelectr.*, submitted, 1995d.

Hocking, W. K., Measurements of turbulent energy dissipation rate in the middle atmosphere by radar techniques: A review, *Radio Sci.*, **20**, 1403–1422, 1985.

Holton, J. R., Troposphere-stratosphere exchange of trace constituents: The water vapor puzzle, in *Dynamics of the Middle Atmosphere*, edited by J. R. Holton and T. Matsuno, 369–385, D. Reidel, 1984.

Johnson, R. H., Heat and moisture sources and sinks of Asian monsoon precipitating systems, *J. Meteor. Soc. Japan*, **70**, 353–372, 1992.

Kodaira, N., R. Tachihira, D. Shizaki, A. Takeda, Y. Iwasaka, and K. Naito, Special edition for meteorological radars, *Study note of the meteorological society of Japan*, **139**, 9–10, 1980 (in Japanese).

Kurosaki, S., M. D. Yamanaka, H. Hashiguchi, T. Sato, and S. Fukao, Vertical eddy diffusivity in the lower and middle atmosphere: A climatology based on

the MU radar observations during 1986–1992, *J. Atmos. Terr. Phys.*, in press, 1995.

Larsen, M. F., M. C. Kelley, and K. S. Gage, Turbulence spectra in the upper troposphere and lower stratosphere at periods between 2 hours and 40 days, *J. Atmos. Sci.*, **39**, 1035–1041, 1982.

Larsen, M. F. and J. Röttger, Comparison of tropopause height and frontal boundary locations based on radar and radiosonde data, *Geophys. Res. Lett.*, **10**, 325–328, 1983.

Larsen, M. F., S. Fukao, O. Aruga, M. D. Yamanaka, T. Tsuda, and S. Kato, A comparison of VHF radar vertical velocity measurements by a direct vertical beam method and by a VHF technique, *J. Atmos. Ocean. Tech.*, **8**, 766–776, 1991.

Lau, K.-M., L. Peng, C. H. Sui, and T. Nakazawa, Dynamics of super cloud clusters, westerly bursts, 30–60 day oscillations and ENSO: An unified view, *J. Meteor. Soc. Japan*, **67**, 205–219, 1989.

Lau, K.-M., East Asian summer monsoon rainfall variability and climate teleconnection, *J. Meteor. Soc. Japan*, **70**, 211-242, 1992.

Lhermitte, R. M., Probing air motion by Doppler analysis of radar clear air returns, *J. Atmos. Sci.*, **23**, 575–591, 1966.

May, P. T., R. G. Strauch, K. P. Moran, and W. L. Ecklund, Temperature sounding by RASS with wind profiler radars: A preliminary study, *IEEE Transact. Geosci. Remote Sens.*, **28**, 19–28, 1990.

May, P. T. and J. M. Wilczak, Diurnal and seasonal variations of boundary layer structure observed with a radar wind profiler and RASS, *Mon. Wea. Rev.*, **121**, 673–682, 1993.

Mechtly, E. A., S. A. Bowhill, K. P. Gibbs, and L. G. Smith, Changes of lower ionosphere electron concentrations with solar activity, *J. Atmos. Terr. Phys.*, **34**, 1899–1907, 1972.

Morimoto, S., Study of observation techniques of middle and upper atmosphere by using the MU radar, *Master thesis, Department of electric engineering II, Kyoto University*, 43pp., 1985 (in Japanese).

Murayama, Y., T. Tsuda, M. Yamamoto, T. Nakamura, T. Sato, S. Kato, and S. Fukao, Dominant vertical scales of gravity waves in the middle atmosphere observed with the MU radar and rocketsondes, *J. Atmos. Terr. Phys.*, **54**, 339–346, 1992.

Nakamura, K. and Y. Masuda, Development of a lower troposphere wind profiler at communications research laboratory, *Preprints of the International Symposium on Middle Atmosphere Science, Kyoto, 23–27 March*, 48–49, 1992.

Nakamura, T., T. Tsuda, M. Tsutsumi, K. Kita, T. Uehara, and S. Fukao, Meteor wind observations with the MU radar, *Radio Sci.*, **26**, 857–869, 1991.

Nakamura, T., T. Tsuda, S. Fukao, S. Kato, and R. A. Vincent, Comparison of the mesospheric gravity waves observed with the MU radar (35°N) and the Adelaide MF radar (35°S), *Geophys. Res. Lett.*, **20**, 803–806, 1993a.

Nakamura, T., T. Tsuda, M. Yamamoto, S. Fukao, and S. Kato, Characteristics of gravity waves in the mesosphere observed with the middle and upper atmosphere radar, 1. Momentum flux, *J. Geophys. Res.*, **98**, 8899-8910, 1993b.

Nakazawa, T., Tropical super clusters within intraseasonal variations over the western Pacific, *J. Meteor. Soc. Japan*, **66**, 823–839, 1988.

Nitta, Ts., T. Maruyama, and T. Motoki, Long-term variation of tropospheric circulations in the western Pacific region as derived from GMS cloud winds, *J. Meteor. Soc. Japan*, **64**, 895–911, 1986.

Nitta, Ts., T. Mizuno, and K. Takahashi, Multi-scale convective systems during the initial phase of the 1986/87 El Niño, *J. Meteor. Soc. Japan*, **70**, 447–466, 1992.

Ottersten, H., Atmospheric structure and radar backscattering in clear air, *Radio Sci.*, **4**, 1179–1193, 1969a.

Ottersten, H., Mean vertical gradient of potential refractive index in turbulent mixing and radar detection of CAT, *Radio Sci.*, **4**, 1247–1249, 1969b.

Rogers, R. R., W. L. Ecklund, D. A. Carter, K. S. Gage, and S. A. Ethier, Research applications of a boundary-layer wind profiler, *Bull. Amer. Meteor. Soc.*, **74**, 567–580, 1993.

Röttger, J., VHF radar observations of a frontal passage, *J. Appl. Meteor.*, **18**, 85–91, 1979.

Röttger, J. and M. F. Larsen, UHF/VHF radar techniques for atmospheric research and wind profiler applications, in *Radar in Meteorology: Battan Memorial and 40th Anniversary Radar Meteorology Conference*, edited by D. Atlas, American Meteorological Society, 235–281, 1990.

Salby, M. L. and R. R. Garcia, Transient response to localized episodic heating in the tropics. Part I: Excitation and short-time near-field behavior, *J. Atmos. Sci.*, **44**, 458–498, 1987.

Sato, K., Small-scale wind disturbances observed by the MU radar during the passage of typhoon Kelly, *J. Atmos. Sci.*, **50**, 518–537, 1993.

Sato, T., Radar principles, in *Lecture Notes of International School on Atmospheric Radar (ISAR), Kyoto, 24–28 November*, Chapter 2, 1988.

Sato, T., N. Ao, M. Yamamoto, S. Fukao, T. Tsuda, and S. Kato, A typhoon observed with the MU radar, *Mon. Wea. Rev.*, **119**, 755–768, 1990.

Silver, S., *Microwave Antenna Theory and Design*, McGraw-Hill, New York, 1951.

Skolnik, M. L., *Introduction to Radar Systems*, McGraw-Hill, New York, 1980.

Stull, R. B., *An Introduction to Boundary Layer Meteorology*, 666pp., Kluwer Academic Publishers, 1988.

Sukmadradjat, P. Mardio, C. R. Williams, P. E. Johnston, A. C. Riddle, and K. S. Gage, Wind observations over Biak during TOGA COARE, *Preprints of the Fifth International Symposium on Equatorial Atmosphere Observations over Indonesia, Jakarta, 8–9 December*, II-5, 9pp., 1993.

Sumi, A., On the movement of the "convection center" from summer to winter season in the northern hemisphere, *J. Meteor. Soc. Japan*, **64**, 605–611, 1986.

Takayabu, Y. N. and Ts. Nitta, 3–5 day-period disturbances coupled with convection over the tropical Pacific ocean, *J. Meteor. Soc. Japan*, **71**, 221–246, 1993.

Takeuchi, K. and J. Kondo, *Atmosphere Near the Ground*, Lectures in Atmospheric Science: Part 1, 226pp., University of Tokyo Press, 1990 (in Japanese).

Trenberth, K. E., General characteristics of El Niño-Southern Oscillation, in *Teleconnections Linking Worldwide Climate Anomalies: Scientific Basis and Societal Impact*, Cambridge University Press, 13–42, 1991.

Tsuda, T., S. Kato, H. Manson, and C. E. Meek, Characteristics of semidiurnal tides observed by the Kyoto meteor radar and Saskatoon medium-frequency radar, *J. Geophys. Res.*, **93**, 7027–7036, 1988.

Tsuda, T., Y. Murayama, H. Wiryosumarto, S. Kato, S. W. B. Harijono, S. Fukao, M. Karmini, C. M. Mangan, S. Saraspriya, and A. Suripto, A preliminary report of radiosonde observations of the equatorial atmosphere dynamics over Indonesia, *J. Geomag. Geoelectr.*, **44**, 1041–1055, 1992.

Tsuda, T., Y. Murayama, H. Wiryosumarto, S. W. B. Harijono, and S. Kato, Radiosonde observations of equatorial atmosphere dynamics over Indonesia, Part I: Equatorial waves and diurnal tides, *J. Geophys. Res.*, **99**, 10491–10505, 1994a.

Tsuda, T., Y. Murayama, H. Wiryosumarto, S. W. B. Harijono, and S. Kato, Radiosonde observations of equatorial atmosphere dynamics over Indonesia, Part II: Characteristics of gravity waves, *J. Geophys. Res.*, **99**, 10507–10516, 1994b.

Tsuda, T., Y. Murayama, T. Nakamura, R. A. Vincent, A. H. Manson, C. E. Meek, and R. L. Wilson, Variations of the gravity wave characteristics with height, season and latitude revealed by comparative observations, *J. Atmos. Terr. Phys.*, **56**, 555–568, 1994c.

Tsuda, T., T. Adachi, H. Hashiguchi, H. Wiryosumarto, S. W. B. Harijono, T. Sribimawati, N. Yoshino, and S. Fukao, Temperature and wind velocity fluctuations in the tropical boundary layer observed with a RASS, *Preprints of the Third International Symposium on Tropospheric Profiling: Needs and Technologies, Hamburg, 30 August–2 September*, 186–188, 1994d.

Tsuda, T., S. Fukao, M. Yamamoto, T. Nakamura, M. D. Yamanaka, T. Adachi, H. Hashiguchi, N. Fujioka, M. Tsutsumi, S. Kato, S. W. B. Harijono, T. Sribimawati, B. P. Sitorus, R. B. Yahya, M. Karmini, F. Renggono, B. L. Parapat, W. Djojonegoro, P. Mardio, N. Adikusumah, H. T. Endi, and H. Wiryosumarto, A preliminary report on observations of equatorial atmosphere dynamics in Indonesia with radars and radiosondes, *J. Meteor. Soc. Japan*, in press, 1995.

Tsutsumi, M., T. Tsuda, T. Nakamura, and S. Fukao, Temperature fluctuations near the mesopause inferred from meteor observations with the MU radar, *Radio Sci.*, **29**, 599–610, 1994.

Wakasugi, K., A. Mizutani, M. Matsuo, S. Fukao, and S. Kato, A direct method for deriving drop-size distribution and vertical air velocities from VHF Doppler radar spectra, *J. Atmos. Ocean. Tech.*, **3**, 623–629, 1986.

Wakasugi, K., A. Mizutani, M. Matsuo, S. Fukao, and S. Kato, Further discussion on deriving drop-size distribution and vertical air velocities directly from VHF Doppler radar spectra, *J. Atmos. Ocean. Tech.*, **4**, 170–179, 1987.

Wallace, J. M. and V. E. Kousky, Observational evidence of Kelvin waves in the tropical stratosphere, *J. Atmos. Sci.*, **25**, 900–907, 1968.

Webster, P. J. and R. Lukas, TOGA COARE: The Coupled Ocean-Atmosphere Response Experiment, *Bull. Amer. Meteor. Soc.*, **73**, 1377–1416, 1992.

Wilczak, J. M., R. G. Strauch, F. M. Ralph, and D. A. Merritt, Contamination of wind profiler data by migrating birds, *Preprints of the Third International Symposium on Tropospheric Profiling: Needs and Technologies, Hamburg, 30 August–2 September*, 212–214, 1994.

Williams, C. R., S. K. Avery, J. R. McAfee, and K. S. Gage, Comparison of observed diurnal and semidiurnal tropospheric winds at Christmas Island with tidal theory, *Geophys. Res. Lett.*, **19**, 1471–1474, 1992.

Williams, C. R., W. L. Ecklund, and K. S. Gage, Classification of precipitating cloud systems in the tropics using UHF wind profilers, *Preprints of the Third International Symposium on Tropospheric Profiling: Needs and Technologies, Hamburg, 30 August–2 September*, 198–200, 1994.

Woodman, R. F. and A. Guillén, Radar observations of winds and turbulence in the stratosphere and mesosphere, *J. Atmos. Sci.*, **31**, 493–505, 1974.

Woodman, R. F, Spectral moment estimation in MST radars, *Radio Sci.*, **20**, 1185–1195, 1985.

Yamada, T. and G. Mellor, A simulation of the Wangara atmospheric boundary layer data, *J. Atmos. Sci.*, **32**, 2309–2329, 1975.

Yamamoto, M., T. Sato, P. T. May, T. Tsuda, S. Fukao, and S. Kato, Estimation error of spectral parameters of mesosphere-stratosphere-troposphere radar obtained by least squares fitting method and its lower bound, *Radio Sci.*, **23**, 1013–1021, 1988.

Yamanaka, M. D. and S. Fukao, A simple model of gravity-wave momentum and energy fluxes transferred through the middle atmosphere to the upper atmosphere, *J. Atmos. Terr. Phys.*, **56**, 1375–1385, 1994.

Yamanaka, M. D., S. Kurosaki, S. Fukao, H. Hashiguchi, T. Tsuda, and S. Kato, Seasonal and interannual variabilities of vertical eddy diffusivity observed by the MU radar, *Adv. Space Res.*, **14**, 277–280, 1994.

Publication list

Refereed journals

i) Yamanaka, M. D., S. Kurosaki, S. Fukao, H. Hashiguchi, T. Tsuda, and S. Kato, Seasonal and interannual variabilities of vertical eddy diffusivity observed by the MU radar, *Adv. Space Res.*, **14**, 277–280, 1994.

ii) Hashiguchi, H., M. D. Yamanaka, T. Tsuda, M. Yamamoto, T. Nakamura, T. Adachi, S. Fukao, T. Sato, and D. L. Tobing, Diurnal variations of the planetary boundary layer observed with an *L*-band clear-air Doppler radar, *Bound.-Layer Meteor.*, in press, 1995.

iii) Hashiguchi, H., S. Fukao, T. Tsuda, M. D. Yamanaka, D. L. Tobing, T. Sribimawati, S. W. B. Harijono, and H. Wiryosumarto, Observations of the planetary boundary layer over equatorial Indonesia with an *L*-band clear-air Doppler radar: Initial results, *Radio Sci.*, in press, 1995.

iv) Hashiguchi, H., S. Fukao, M. D. Yamanaka, T. Tsuda, S. W. B. Harijono, and H. Wiryosumarto, Boundary layer radar observations of the passage of the convection center over Serpong, Indonesia (6°S, 107°E) during the TOGA COARE intensive observation period, *J. Meteor. Soc. Japan*, in press, 1995.

v) Hashiguchi, H., S. Fukao, M. D. Yamanaka, and T. Tsuda, Frequency spectra of wind velocity fluctuations between 1 hour and 1 month in the atmospheric boundary layer over equatorial Indonesia, *J. Geomag. Geoelectr.*, submitted, 1995.

vi) Kurosaki, S., M. D. Yamanaka, H. Hashiguchi, T. Sato, and S. Fukao, Vertical eddy diffusivity in the lower and middle atmosphere: A climatology based on the MU radar observations during 1986–1992, *J. Atmos. Terr. Phys.*, in press, 1995.

vii) Sato, K., H. Hashiguchi, and S. Fukao, Gravity waves and turbulence associated with cumulus convection observed with the UHF/VHF clear-air

Doppler radars, *J. Geophys. Res.*, in press, 1995.

viii) Tsuda, T., S. Fukao, M. Yamamoto, T. Nakamura, M. D. Yamanaka, T. Adachi, H. Hashiguchi, N. Fujioka, M. Tsutsumi, S. Kato, S. W. B. Harijono, T. Sribimawati, B. P. Sitorus, R. B. Yahya, M. Karmini, F. Renggono, B. L. Parapat, W. Djojonegoro, P. Mardio, N. Adikusumah, H. T. Endi, and H. Wiryosumarto, A preliminary report on observations of equatorial atmosphere dynamics in Indonesia with radars and radiosondes, *J. Meteor. Soc. Japan*, in press, 1995.

ix) Fukao, S., H. Hashiguchi, M. Yamamoto, T. Tsuda, T. Sato, M. D. Yamanaka, T. Nakamura, S. Kato, T. Makihira, and K. Hamatsu, An *L*-band clear-air Doppler radar for the atmospheric boundary layer, *J. Meteor. Soc. Japan*, to be submitted, 1995.

Unrefereed articles

i) Hashiguchi, H., M. Yamamoto, S. Fukao, T. Tsuda, T. Sato, T. Nakamura, M. D. Yamanaka, S. Kato, T. Makihira, and K. Hamatsu, Development of a boundary layer radar, *Proceedings of the Second Symposium of the MU Radar, Kyoto, 12–13 March*, 40–44, 1991 (in Japanese).

ii) Yamamoto, M., H. Hashiguchi, S. Fukao, T. Tsuda, T. Sato, M. D. Yamanaka, T. Nakamura, and S. Kato, Development of a transportable boundary layer radar, *Proceedings of the Second STEP Symposium, Tokyo, March*, 1991 (in Japanese).

iii) Fukao, S., M. Yamamoto, H. Hashiguchi, T. Tsuda, T. Sato, M. D. Yamanaka, T. Nakamura, and S. Kato, Development of a boundary layer radar, *Proceedings of the Sixth Atmospheric Symposium, Tokyo, 21–22 January*, 30–36, 1992 (in Japanese).

iv) Hashiguchi, H., M. Yamamoto, S. Fukao, T. Tsuda, M. D. Yamanaka, T. Nakamura, T. Sato, S. Kato, T. Makihira, and K. Hamatsu, Development of a boundary layer radar, *Preprints of the International Symposium on Middle Atmosphere Science, Kyoto, 23–27 March*, 46–47, 1992.

v) Hashiguchi, H., M. Yamamoto, T. Tsuda, T. Sato, M. D. Yamanaka, T. Nakamura, and S. Fukao, Observations of the planetary boundary layer with a boundary layer radar, *Proceedings of the Third STEP Symposium, Tokyo, May*, 1992 (in Japanese).

vi) Hashiguchi, H., S. Fukao, D. L. Tobing, M. D. Yamanaka, M. Yamamoto, T. Nakamura, T. Adachi, T. Sato, and T. Tsuda, Diurnal variation of the

atmospheric boundary layer observed with a boundary layer radar, *Proceedings of the Seventh Atmospheric Symposium, Tokyo, 26–27 January*, 175–180, 1993 (in Japanese).

vii) Tsuda, T., M. Yamamoto, T. Nakamura, T. Adachi, H. Hashiguchi, N. Fujioka, M. D. Yamanaka, M. Tsutsumi, and S. Fukao, Overview of atmospheric observations in equatorial Indonesia, *Proceedings of the Seventh Atmospheric Symposium, Tokyo, 26–27 January*, 181–184, 1993 (in Japanese).

viii) Fukao, S., T. Tsuda, M. D. Yamanaka, M. Yamamoto, T. Nakamura, H. Hashiguchi, T. Adachi, D. L. Tobing, T. Sato, S. Kato, S. W. B. Harijono, and H. Wiryosumarto, Observations with a boundary layer radar in Indonesia, *Proceedings of the Seventh Atmospheric Symposium, Tokyo, 26–27 January*, 185–190, 1993 (in Japanese).

ix) Tobing, D. L., S. Fukao, T. Tsuda, M. D. Yamanaka, M. Yamamoto, T. Nakamura, H. Hashiguchi, T. Adachi, T. Sato, S. Kato, S. W. B. Harijono, and H. Wiryosumarto, Planetary boundary layer observations in Japan and Indonesia with boundary layer radar, *Preprints of Bandung Symposium, Bandung, May*, 1993.

x) Hashiguchi, H., S. Fukao, M. D. Yamanaka, M. Yamamoto, T. Tsuda, and T. Sato, Diurnal variation of the atmospheric boundary layer observed with a boundary layer radar in Shigaraki, *Proceedings of the Fourth STEP Symposium, Tokyo, June*, 1993 (in Japanese).

xi) Fukao, S., T. Tsuda, H. Hashiguchi, M. D. Yamanaka, M. Yamamoto, T. Nakamura, S. W. B. Harijono, D. L. Tobing, H. Wiryosumarto, and S. Kato, Observations of the equatorial planetary boundary layer with a boundary layer radar in Indonesia, *Proceedings of the Fourth STEP Symposium, Tokyo, June*, 1993 (in Japanese).

xii) Hashiguchi, H., S. Fukao, T. Tsuda, M. D. Yamanaka, M. Yamamoto, T. Nakamura, T. Adachi, T. Sato, S. Kato, S. W. B. Harijono, D. L. Tobing, and H. Wiryosumarto, Observations of the planetary boundary layer in Japan and Indonesia with the Kyoto boundary layer radar, *Proceedings of the Sixth Workshop on Technical and Scientific Aspects of MST/ST Radar, Taipei, 17–20 August*, 58–61, 1993.

xiii) Karmini, M., B. A. Wahyudi, F. Renggono, S. W. B. Harijono, H. Wiryosumarto, H. Hashiguchi, T. Adachi, T. Tsuda, and S. Fukao, A sample of temperature profiles observed by RASS/BLR during atmospheric dynamic observation campaign in Serpong, Indonesia 9 October, 1993, *Preprints of the Fifth International Symposium on Equatorial Atmosphere Observation*

over Indonesia, Jakarta, December, 1993.

xiv) Sribimawati, T., D. W. Soehoed, F. Renggono, B. A. Wahyudi, S. W. B. Harijono, H. Wiryosumarto, H. Hashiguchi, T. Tsuda, and S. Fukao, Observation of diurnal variation of radiation budget, temperature, relative humidity, and wind during dry season campaign over Indonesia, *Preprints of the Fifth International Symposium on Equatorial Atmosphere Observation over Indonesia, Jakarta, December*, 1993.

xv) Tobing, D. L., B. L. Parapat, S. W. B. Harijono, H. Wiryosumarto, H. Hashiguchi, T. Tsuda, and S. Fukao, Observation of planetary boundary layer over Indonesia equatorial atmosphere, *Preprints of the Fifth International Symposium on Equatorial Atmosphere Observation over Indonesia, Jakarta, December*, 1993.

xvi) Hashiguchi, H., M. D. Yamanaka, T. Tsuda, T. Adachi, S. Fukao, S. W. B. Harijono, and H. Wiryosumarto, Observations of the planetary boundary layer with a boundary layer radar in Indonesia, *Proceedings of the Eighth Atmospheric Symposium, Tokyo, January*, 1994 (in Japanese).

xvii) Hashiguchi, H., T. Tsuda, S. Fukao, S. W. B. Harijono, and H. Wiryosumarto, Frequency spectra of wind velocity fluctuations between 1 hour and 1 month in the atmospheric boundary layer over equatorial Indonesia, *Preprints of Eighth International Symposium on Solar Terrestrial Physics, Sendai, 5–10 June*, 246, 1994.

xviii) Fukao, S., H. Hashiguchi, T. Tsuda, M. Yamamoto, T. Adachi, M. D. Yamanaka, T. Nakamura, and T. Sato, Planetary boundary layer observations with an *L*-band clear-air Doppler radar, *Preprints of the Third International Symposium on Tropospheric Profiling: Needs and Technologies, Hamburg, 30 August–2 September*, 117–119, 1994.

xix) Tsuda, T., T. Adachi, H. Hashiguchi, H. Wiryosumarto, S. W. B. Harijono, T. Sribimawati, N. Yoshino, and S. Fukao, Temperature and wind velocity fluctuations in the tropical boundary layer observed with a RASS, *Preprints of the Third International Symposium on Tropospheric Profiling: Needs and Technologies, Hamburg, 30 August–2 September*, 186–188, 1994.